Mikoviny Sámuel

Földtudományi Doktori Iskola

a doktori iskola vezetoje:

Dr. h. c. mult. Dr. Kovács Ferenc

egyetemi tanár

a MTA rendes tagja

APPLICATION OF GEOPHYSICS, PHOTOGRAMMETRY AND REMOTE SENSING FOR POLAR RESEARCH: AN INTERDISCIPLINARY STUDY

Doktori értekezés

Dr. univ. Csathó Beáta

okl. geofizikus mérnök

okl. alkalmazott matematikus

Kutatóhely: Miskolci Egyetem
Muszaki Földtudományi Kar
Geofizikai Tanszék

Tudományos vezeto: Dr. habil. Dobróka Mihály
A muszaki tudományok doktora
Tanszékvezeto egyetemi tanár

Miskolc, 2003.

TABLE OF CONTENTS

TABLE OF FIGURES

TARTALMI KIVONAT

Mint ismeretes, a Föld felszínének homérséklete 0.5 Celsius fokot emelkedett az elmúlt évszázadban, és utolsó két évtizedre egyre fokozódó felmelegedés volt jellemzo. Egyre több jel mutat arra, hogy ez az általános felmelegedés jelentos részben civilizációs eredetu. Az emberi tevékenység megnövelte az üvegházhatást okozó gázok (elsosorban széndioxid, metán és nitrogén dioxidjai) mennyiségét és ezzel megváltoztatta az atmoszféra összetételét. Az Antarktisz és Grönland jégtömege együttesen több mint 33 millió köbkilométer jeget tárol. Ha ez a jégtömeg elolvadna, a világtengerek szintje közel 70 métert emelkedne. Az éves átlagos csapadékmennyiség Grönland és Antarktisz jégtakarója felett együttesen mintegy 6.5 mm tengerszintváltozásnak felel meg. Nyilvánvaló tehát, hogy a csapadékmennyiség és a jégtakaróból a tengerbe visszatéro vízmennyiség egyensúlyának akár kismértéku megbomlása is jelentos szerepet játszhat a világtengerek szintjének jelenleg megfigyelt 1.8 mm/év változásában. Valóban, a tengerek szintváltozását az elmúlt néhány millió évben az eljegesedés mértéke határozta meg, és az eljegesedett területek gyors csökkenése változás a jelenleginél egy nagyságrenddel nagyobb volt. Ezért a sarkvidéki területek jégtakarójának változásának ismerete alapveto fontosságú az emberiség számára.

Az eddigi kutatás elsosorban a jég-atmoszféra-oceán-aljzat rendszer egyes elemeinek pontosabb megismerésére irányult. A gleccserek jövobeli viselkedését megjósoló modellek egyszeru paraméterezéseket és éghajlati feltételeket használtak. Például, van der Veen kijelenti, hogy „a felszíni hófelhalmozódás és csökkenés mértékét becsülo gleccserkutatási modellekben használt paraméterezés jósága, különösen változó éghajlati viszonyok esetén nem bizonyított”. A sarkvidéki területek jelenlegi állapotának megértéséhez és a jövobeli hatásokat pontosabb elorejelzéséhez pontos és nagyfelbontású mérésekre, valamint összetett, a jégtakaró dinamikus változását, a földkéreg összetételét és a meteorológiai hatásokat ötvözo modellekre van szükség.

Ez a dolgozat interdiszciplináris megközelítést javasol geofizikai, távérzékelési, fotogrammetriai és gleccserkutatási eredmények együttes kezelésére. Az állandóan növekvo adatmennyiség új részleteket szolgáltat a különbözo folyamatok térbeli és idobeli eloszlásáról. Kutatásom a jéggel fedett területek folyamatainak minél teljesebb megismerésére irányult, új feldolgozó és értelmezo eljárások kifejlesztésével és az adatok együttes értelmezésével. A grönlandi jégtakaró tömegmérlegét kutató csoport tagjaként elkészítettem Grönland csapadéktérképét és egy, geofizikai, gleccserkutatási, távérzékelési és fotogrammetria adatokat tartalmazó térinfomatikai rendszert hoztam létre. Új feldolgozó eljárásokat fejlesztettem ki a jégtakaró jelenlegi és múltbeli elterjedésének és vastagságának meghatározására muholdfelvételekbol, repülogépes és muholdas lézer térképezésbol. Geofizikai és gleccserkutatási adatok együttes értelmezésével kimutattam, hogy Grönland Ény-i részén a jégtömeg dinamikája és az aljzat geológiája szoros kapcsolatban áll. Elsoként alkalmaztam légi lézeres felmérést a sarkvidéki gleccserkörnyéki és vulkanikus területek geomorfológiai térképezésére, új, izgalmas területet nyitva meg ezzel a további kutatás számára.

ABSTRACT

The Earth's surface temperature has risen by about 0.5 degree celsius in the past century, with accelerated warming during the past two decades. There is new and stronger evidence that most of the warming over the last 50 years is attributable to human activities. Human activities have altered the chemical composition of the atmosphere through the buildup of greenhouse gases – primarily carbon dioxide, methane, and nitrous oxide.

The Antarctic and Greenland ice sheets together hold 33 million cubic km of ice, representing enough water to raise global sea level by 70 m. Annual snowfall on the ice sheets is equivalent to 6.5 mm of sea level, so that only a small imbalance between snowfall and discharge of ice and meltwater into the ocean could be a major contributor to present-day sea-level rise (~1.8 mm/year). Large variations in sea level over the past million years have in fact been controlled by ice, with rates of sea-level rise at least one order of magnitude larger than at present during times of rapid deglaciation. Consequently, a detailed knowledge and understanding of the evolution of polar ice sheets is of considerable societal importance. Most of the research so far focused on the individual components of the ice-atmosphere-ocean-solid Earth system. Glaciological models, predicting the future contributions of the polar ice sheets, used simple parameterizations and climate forcing. For example, van der Veen, C.J. concludes that "the validity of the parameterizations used by glaciological modeling studies to estimate changes in surface accumulation and ablation under changing climate conditions has not been convincingly demonstrated."

To understand the current conditions and predict future changes we need more accurate measurements covering large areas of the polar regions, and the development of complex models combining ice dynamics, post-glacial rebound, solid Earth geophysics and climate.

This dissertation promotes a interdisciplinary approach, using results from geophysics, remote sensing, photogrammetry and glaciology for the investigation of the polar regions. The ever increasing amount of data provides new details of the spatial and temporal behavior of the different processes. My goal is to develop new tools to extract the relevant information and to combine data for more accurate modeling and results of this research are summarized in this dissertation. I contributed to the first estimation of mass balance of the Greenland ice sheets. I developed new tools for fast and accurate mapping of current and past conditions of the ice sheets and glaciers from satellite imagery and satellite and laser altimetry. My integrated interpretation of the geophysical and glaciological data revealed a strong relationship between subice geology and ice dynamics in Greenland. By a novel processing of airborne laser scanning data a new insight was gained into the geomorphology of glaciated and volcanic areas in Antarctica.

INTRODUCTION

A large part of our planet is permanently or periodically covered by snow and ice. About 10% of the land surface is covered with glaciers and with the ice sheets of Greenland and Antarctica. The total volume of the polar ice sheets is approximately 33 million cubic km. This volume would raise the global sea level by almost 70 m, if fully melted. The average annual precipitation of Greenland and Antarctica together corresponds to 6.5 mm/year global sea level change and the current estimate of the global sea level rise is 1.8 mm/year (Rignot and Thomas, 2002). It is therefore obvious that even a slight change in the balance between the precipitation and the discharge from the ice sheets into the ocean, could have a strong influence on the sea level change.

Based on the intensive research of the last decades, there is a growing consensus in the research community, that the warming trend of the last 50 years can mostly be attributed to the effects of human activity. The increase of the greenhouse gases in the atmosphere has changed the balance of the Earth-atmosphere system. According to the Report of the Intergovernmental Panel on Climate Change (Houghton and others, 2001) 1.4-5.8 ^{o}C temperature increase and 0.09-0.48 m sea level change are expected in the next century. The most likely value of the latter (the average of the model runs) is 0.48 m, which is about 2-4-times larger than the sea level change observed in the 20th century. This sea level rise wouldn't threaten the majority of the coastal cities, but it could harm the coastal flora and fauna as well as the fresh water reserves. Moreover, it might increase the devastating effect of the hurricanes and major storms.

Unlike Antarctica, Greenland is not centered on the pole, but it is located at lower latitudes. Therefore the Greenland ice sheet may serve as a sensitive indicator of climate changes. If the current warming trend continues, the partial melting of the Greenland ice sheet will result a 0.09 m/year sea level rise during the 21st century. Model calculations suggest that a long-term 3 ^{o}C/century or larger increase in the global temperature could result the complete melt of the Greenland ice sheet within a thousand year.

The error and the sensitivity of the model calculations are rather large, and one of the major goals of the polar research is to provide more accurate predictions. The IPCC report also emphasizes how important it is to improve the accuracy of the mass balance estimates and to increase the complexity of the models depicting dynamic behavior of the cryosphere. It is mandatory to combine the results from several disciplines, such as geophysics, geodesy, atmospheric sciences to answer these questions. This dissertation summarizes the results obtained by using such an interdisciplinary approach for investigating the mass balance and dynamics of the Greenland and Antarctic ice sheets.

1.0 DETERMINATION OF MASS BALANCE OF GREENLAND ICE SHEET BY A TRADITIONAL APPROACH

1.1. Introduction

Comparison of ice discharge from higher elevation areas of the entire Greenland Ice Sheet with total snow accumulation gives estimates of ice thickening rates over the past few decades. On average, the region has been in balance, but with thickening of 21 centimeters per year in the southwest and thinning of 30 centimeters per year in the southeast. The north of the ice sheet shows less variability, with average thickening of 2 centimeters per year in the northeast and thinning of about 5 centimeters per year in the northwest. These results agree well with those from repeated altimeter surveys, except in the extreme south, where we find substantially higher rates of both thickening and thinning.

1.2. Measurements and mass balance computation

During 1993 through 1997, ice motion was inferred from repeat GPS (Global Positioning System) measurements at stations (Fig. 1) completely circumnavigating the Greenland Ice Sheet (Thomas and others, 2000a), with a 1- or 2-year interval between repeat surveys. Stations were about 30 km apart, close to the 2000-m contour, apart from several in the southeast, which were substantially higher because of high mountains, crevasses, and nunataks.

We estimated ice discharge (Q) through gates between adjacent stations as the product of surface ice velocity, ice thickness, and a correction factor, R, equal to column-averaged velocity divided by surface velocity. This product was integrated across the gate width normal to ice motion, assuming linear variation of velocity across the gate (Thomas and others, 1998). Airborne ice-thickness measurements were made along the stake line with a coherent radar depth sounder operating at a center frequency of 150 MHz (Gogineni and others, 2001). Values of R were derived from a model simulation of the ice sheet that takes account of basal sliding and a variable temperature with depth (Huybrechts, 1996). We then compared Q with the total flux (V) of ice accumulated as snow over the catchment region, with area S, corresponding to the gate, and estimated an average ice thickening rate T = (V - Q)/S (Fig. 3.a and Fig. 4). Accumulation rates (A) are from published estimates (Ohmura and Reeh, 1991) updated with information from other investigations (Bales and others, 2001; Csathó and others, 1999a). To obtain a regular grid from the irregular distributed ice core data a new method was developed. The approach is based on multivariate regression and kriging, and a correction was applied to consider the effect of sublimation (Csathó and others, 1997; van der Veen and others, 2001; Csathó B., in preparation). The computed accumulation and precipitation grids show very good agreement with the precipitation distribution obtained from climate modeling (Fig. 2). Catchment areas were

estimated by reconstructing flow lines passing through all velocity stations, assuming the ice to move in the direction of maximum regional surface slope (Thomas and others, 1998).

Errors are large for individual gates (Thomas and others, 1998), mainly because of large percentage errors in S, A, and R for the small associated catchment regions. Consequently, we present our results as values of T calculated for several adjacent traverse stations, such that their collective catchment area is about 30,000 km 2 (Fig. 3.a and Fig. 4). The group of gates was shifted, one traverse station at a time, to give values of T plotted in Fig. 4. (solid line) at positions corresponding to the centers of the uncertainty in local values of A and R, which we assume to be ±10% and ±5%, respectively (Thomas and others, 1998). The resulting error in T is about 0.11A, with A ≤ 40 cm of ice per year for about 80% of the ice sheet. Estimates of T derived from satellite radar altimetry are correlated over distances less then about 170 km (Davis, C., personal communication), suggesting that accumulation rates and velocities are correlated over similar distances. Consequently, we assume that errors in A and R are independent over distances greater than 170 km so that errors should be less than 0.11A. For areas larger than 100,000 km^2, errors reduce to about 0.07A, or less than 3 cm/year for most of the ice sheet, apart from the southeast corner, where accumulation rates increase to about 80 cm of ice per year.

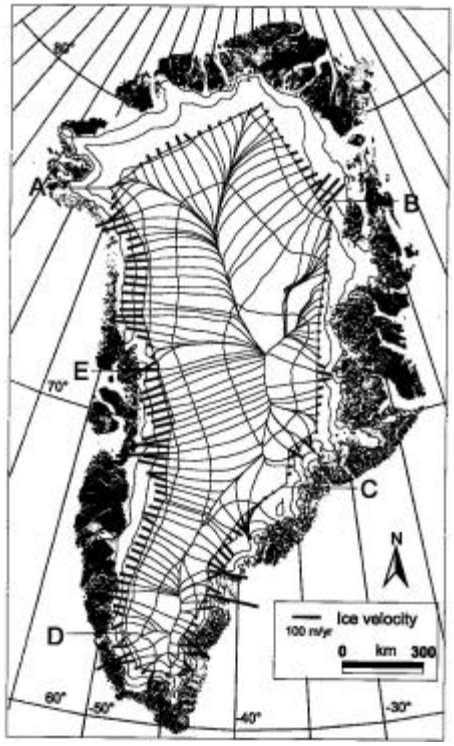

Fig. 1. Greenland, showing ice velocities at traverse stations where ice motion was inferred from repeated GPS measurements.
Elevation contours and ice ßow lines corresponding to the velocity stations are also shown. A, B, C, etc., mark 1000-km intervals along the traverse. From Thomas and others, 2000a.

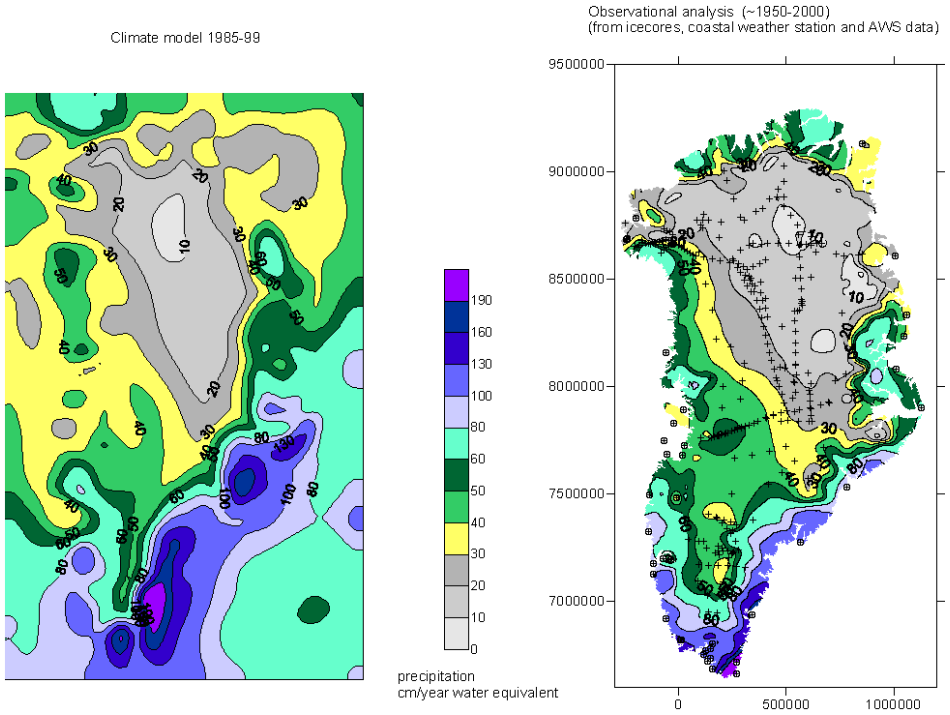

Fig. 2. Comparison of Greenland precipitation grids derived from climate modeling and from ice core and pit observations.
Left panel: climate modeling (L. Bai, in preparation); right panel: ice core and pit analysis (B. Csathó, in preparation).

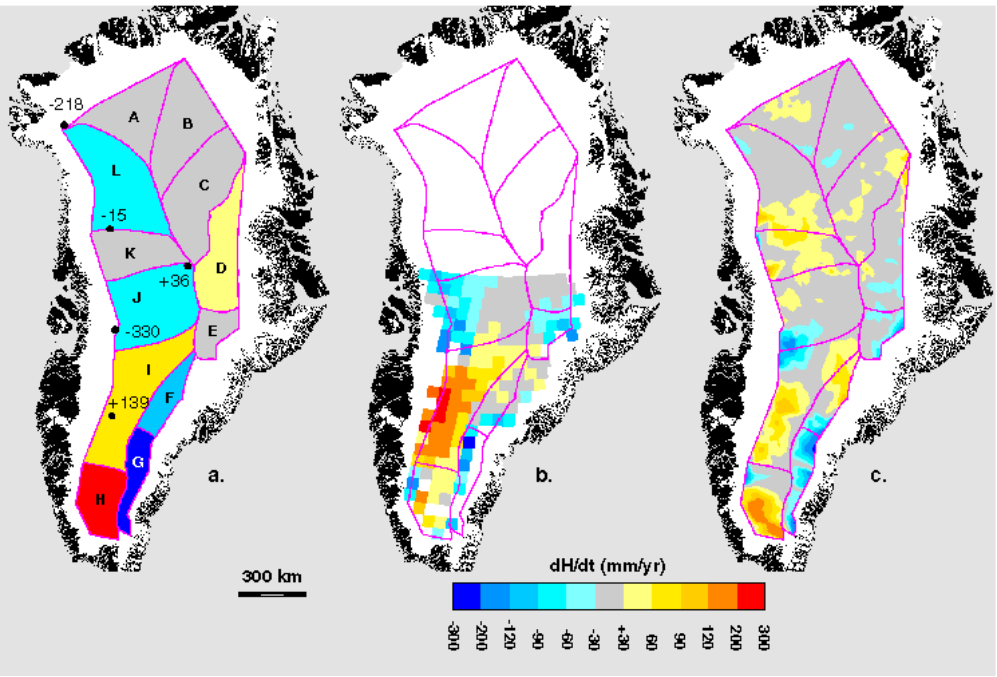

Fig. 3. Three independent estimates of Greenland ice-sheet thickening/thinning rates.
(a) for the last few decades derived from comparison of ice discharge with snow accumulation; (b) for 1978-88 derived from comparison of Seasat and Geosat radar-altimeter data; and (c) for 1993/4-98/9 derived from repeated aircraft laser-altimeter surveys. The altimetry results have been corrected for estimated rates (~5 mm/yr) of isostatic uplift of underlying bedrock. From Thomas and others, 2001.

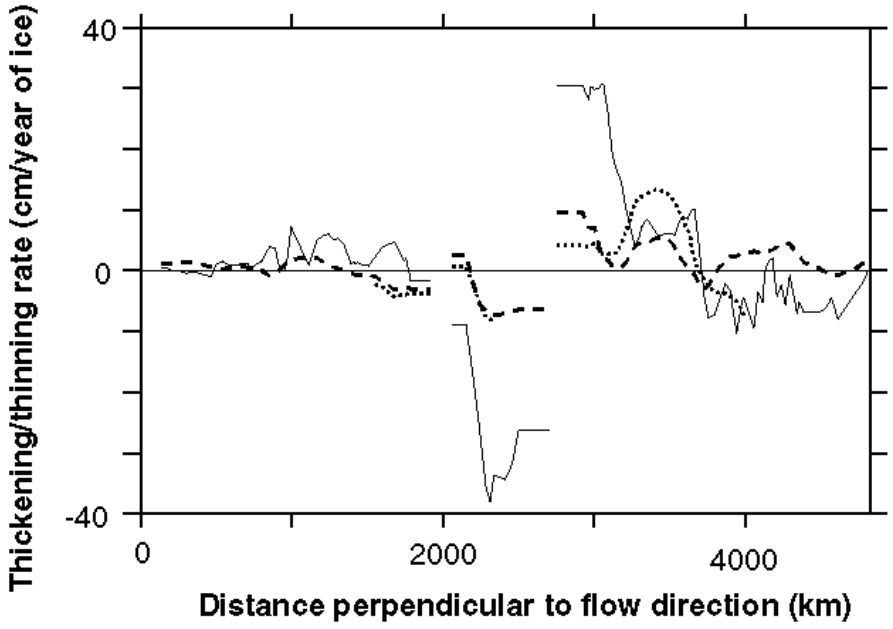

Fig. 4. Rates of ice-thickness change (dH/dt) plotted against clockwise distance around the traverse. Plot starts in the northwest corner of 2000-m contour (Fig. 1), for each of the three sets of estimates. Values of dH/dt are averages for catchment areas of about 30,000 sq km. Solid line: comparison of ice discharge with snow accumulation (Fig. 3.a); dotted line: from comparison of Seasat and Geosat radar-altimeter data (Fig. 3.b); dashed line: from comparison of repeat aircraft laser-altimeter surveys (Fig. 3.c). From Thomas and others, 2001.

Our results are a comparison between current ice discharge and total accumulation based on measurements for time periods ranging from a few years to centuries and for different time windows in the past. Taken as a whole, they refer to conditions averaged over the past few decades, and our estimated thickening rates are appropriate to the same period, assuming that velocities close to the 2000-m contour line change slowly with time. The inferred values of T are spatially variable in the south. Here the western part of the ice sheet is thickening by 66±27 mm/year, increasing to 211±52 mm/year at the southern tip, whereas the eastern part is thinning at an average of 108±62 mm/year, rising to 295±79 mm/year over a 30,000 km^2 area near the southeast tip (Fig. 4, solid line).

South of about 69°N, our study area totals 240,000 km^2, with an overall thickening rate of 22(23 mm/year. North of 69°N, the ice sheet has been thinning in the west at an average of 41±14 mm/year, thickening in the east at 21(6 mm/year, and thinning by 2±13 mm/year in the northernmost zone. There may have been thinning at latitude 70°N on the east side of the ice sheet. Overall, the northern region, with a total area of 737,000 km^2, thinned by 11±7 mm/year. The almost 1 million km^2 of the ice sheet within our area of study thinned by 2±7 mm/year during the past few decades.

Consequently, within the errors of our measurements, the higher elevation parts of the ice sheet have been almost exactly in balance when considered as a whole and as northern and southern parts. However, major changes have been occurring within the southern part of the ice sheet, with a remarkable contrast between rapid thinning in the east and thickening in the west. The north also exhibits bimodal behavior, but at more subdued rates, and a reversal to thickening in the east and thinning in the west. Thickening in the southwest is consistent with a similar pattern of long-term thickening from a model simulation of the ice sheet evolution, forced by the past temperature record *(*Huybrechts, 1994). This suggests that the observed thickening in this area represents a long-term dynamic response of the ice sheet rather than the effects of recent changes in accumulation rates. Our results show close agreement with estimates of Greenland ice thickening rates, for 1978–88 up to latitude 72°N from comparison of satellite radar-altimeter data (Davis and others, 2000) and for 1993/4 –1998/9 for the entire region from comparison of aircraft laser-altimeter data (Krabill and others, 1999 and 2000). These estimates of T are based on changes in measured surface elevation where repeat surveys pass over the same locations and include vertical motion of a few mm/year of underlying rock. Fig. 3 and 4 also include results from the satellite radar altimeter measurements (Davis and others, 2000) and laser-altimeter survey (Krabill and others, 2000), averaged over the regions of our study.

The greater spatial variability in our results is probably indicative of larger errors (about 5 cm/year). However, the two results diverge in the south (between 2000 and 3000 km Fig. 4), where our inferred rates of thickening in the west and thinning in the east are both far larger than the altimetry-derived estimates. This is an area of high accumulation rates (70 to 90 cm of ice per year) with high spatial variability, so our observations could simply result from overestimation in the west and underestimation in the east of local accumulation rates (by about 25%). We believe that this is unlikely, so earlier thickening and thinning rates in this area appear to have been substantially larger than those observed by Krabill and others (2000) between 1993 and 1998. The most likely explanation is recent changes in local snow-accumulation rates, as suggested by the analysis of shallow ice cores. Finally, we stress that these results apply only to average conditions over higher elevation parts of the ice sheet. At lower elevations, the repeat laser-altimeter measurements show that thinning predominates (Krabill, 2000).

1.3. Summary

The major goal of the research presented in this chapter was to calculate the current mass balance of the Greenland ice sheet by using the traditional approach. This approach entails the measurement of ice thickness and velocity as well as the estimation of the precipitation. The mass balance is computed as the difference of the incoming mass and the outgoing flux. My role included the participation in field measurements and data processing (Sohn and others, 1994; Sonntag and others, 1997) and calculating the mass balance distribution. I was also leading the

development of the Greenland GIS Database System (GGDS) that serves for the storage, retrieval and manipulation of all related data set (Kim and other, 2000; Csathó and others, 1999a). To accurately estimate the distribution of the snowfall I have created a new accumulation map of Greenland by statistical method (Csathó and others, 1997 and 1999a). This accumulation map was also used for more detailed, local studies (Rignot and others, 2000) and for comparison with climate modeling results (Csathó and others, 1997; Bromwich and others, 1998.). As new data become available we continue to improve this important data set (Bales and others, 2001; van der Veen and others, 2001; Csathó and others, in preparation).

The Greenland mass balance study, combined with repeat airborne surveys resulted the first reliable estimation of the current mass balance of the Greenland ice sheet (Thomas and others, 1997, 1998, 2000 and 2001).

My results related to the mass balance study are summarized in Section I of the thesis booklet.

2.0 DEVELOPMENT OF AIRBORNE AND SPACEBORNE LASER ALTIMETRY METHODS

2.1. Algorithm Development for NASA's Geoscience Laser Altimetry System (GLAS)

The Geoscience Laser Altimeter System (GLAS) is the first laser altimetry satellite system orbiting the Earth (Fig. 5). The GLAS system consists of both LIDAR and altimetry subsystems and it is the sole sensor of the ICESat, the Ice Cloud, and Land Elevation Satellite that was launched in January 2003. GLAS is designed to map the surface of our planet with unprecedented details and accuracy.

Fig. 5. Official NASA logo of ICESat mission.
ICESat will carry the Geoscience Laser Altimeter System (GLAS) for measurement of changes in the size of Earth's polar ice sheets,the heights of global clouds and aerosols,and global land topography.

The objectives of GLAS surface elevation measurements are stated in detail in Zwally and others (2002) and in the *Geoscience Laser Altimeter System (GLAS) Science Requirements* document available online at http://www.csr.utexas.edu/glas/Science_Objectives/. In summary, they are:

- Measure elevation changes of the Greenland and Antarctic ice sheets for the purpose of assessing:
  - mass balance,
  - seasonal and interannual elevation variability,

- elevation trends, and
- contribution to sea level rise.

- Determine precise elevation topography and surface roughness of ice sheets and sea ice.
- Conduct global topographic measurements to contribute to topographic maps and digital elevation models as well as detect land elevation changes in excess of 1 meter per year in certain selected regions.

In order to achieve these objectives, accurate and consistent interpretation of the waveforms is necessary. Each individual waveform is digitized on-board stored for post-processing. Toward that end, the goals of the waveform surface elevation algorithm development are:

- Define and determine the surface elevation from the laser waveforms,
- Identify and interpret multiple returns,
- Determine surface roughness and slope based on waveform characteristics.

The so called GLAS level 2 products include ice sheet, sea ice and ocean elevation and roughness. The following section summarizes the geometric and optical properties of these surface types and the processing steps to extract geophysical parameters from the return waveform of GLAS. The interested reader is referred to Brenner and others (2003) for more details on the waveform processing algorithm.

2.1.1. Historical Perspective of Altimetry

The idea of using an altimeter in a space orbit to measure the earth's surface was first shown as feasible when a radar altimeter was flown on Skylab in 1974. In 1975 GEOS-3 became operational with a radar altimeter that was designed to measure the ocean surfaces. GEOS-3 covered latitudes of +/- 65 deg that included the southern tip of the Greenland ice sheet. Brooks and others, 1978 showed the feasibility of using these radar altimeter measurements to get topographic measurements over Greenland. Two other U.S. missions, SEASAT in 1978 and GEOSAT (1985-89), flew radar altimeters also designed to measure ocean surfaces. These covered latitudes to +/- 72 deg and could only maintain track over slopes less than 1 deg giving coverage of 40% of Greenland and 24% of Antarctica. NASA developed algorithms (Martin and others, 1983) to post-process the return pulse energy waveform to calculate surface elevations of the ice sheets, and topographic maps were produced (Zwally and others, 1983). Methods were also developed to calculate elevation changes using information from crossing arcs from measurements at different times (Zwally and others, 1989).

The launching of the ERS-1 radar altimeter and its successor ERS-2 have given us continuous ice sheet measurements since 1991 that extended coverage up to +/- 81 deg. These

newer altimeters were also designed with a special ice mode capability to extend coverage of tracking into the more sloping regions of the ice sheets and land. Elevation change estimates have been calculated from the radar measurements giving change histories from 1978 to present day (Wingham and others, 1998; Davis and others, 1998). However, due to limitations of radar altimetry these have large error bounds. Radar altimeter data have also been applied to measurement of land elevations in a few cases. (Frey and Brenner, 1990; Brenner and others, 1990; Koblinsky and others, 1993; Bamber and Muller, 1998).

There are several limitations in measuring ice sheet and land elevations using radar altimetry:

- The footprint is very large 10-20 km in diameter, increasing with the surface slope.
- The measurement is a mean elevation over the footprint surface for flat surfaces with small undulations.
- Over sloping surfaces, the measurement is to the higher elevations that are not necessarily at the sub-satellite location, and topographic knowledge is inadequate to properly geolocate the measurement.
- Tracking can only be maintained over small slopes, ~ 1 deg.

A spaceborne laser altimeter can overcome many of these limitations. The footprint for GLAS is ~70m so that the effect of sloping surfaces is reduced greatly. GLAS should easily be able to track surfaces on slopes up to 3 deg, which includes the majority of the continental ice sheets. The main problem with the small footprint is the accuracy to which the off-nadir angle must be known in order to precisely geolocate it. This is being addressed with the star cameras and the laser spot imaging.

A small footprint (1m), scanning laser altimeter, the Airborne Topographic Mapper (ATM) has been flown successfully over the past 10 years on aircraft over the Greenland ice sheet (Thomas and others, 1994) with the objective of measuring the rate of change of surface elevations towards assessing ice-sheet mass balance. As with all laser altimeters, major limitations are the accuracy of the aircraft position in inertial space and atmospheric interference in the form of clouds or ice fog. Nevertheless, 10-cm accuracy is achieved over flight lines of several hundred km (Krabill and others, 1995), yielding data that have been used to infer rates of ice thickening and thinning over much of the ice sheet (Krabill and others, 2000). The scanning ability of the ATM provides highly detailed surface topography within the 140-300 meter wide surveyed swath, which can be used to help simulate GLAS waveforms and, after launch, to validate GLAS-derived surface elevations and roughness.

The predecessor of GLAS, the Mars Orbiting Laser Altimeter, MOLA, uses algorithms similar to those that GLAS will use and has shown the feasibility of using a spaceborne laser to map a planet surface (Zuber and others, 1998). The accuracy of MOLA is limited by its tracking algorithm (post-processing is not feasible since there are no waveforms telemetered) and the orbit accuracy that is driven by the precision of the gravity models available to date. Orbit determination with the advent of GPS, more accurate force models, and sophisticated computer techniques can give us the position of the earth-orbiting ICESat satellite to an accuracy of 5 cm in inertial space. This precision, combined with the very accurate attitude knowledge, altimeter measurements, and models to account for the atmospheric delays and earth dynamic effects, will allow us, in ideal conditions, to measure the ice sheets to within 10 cm. The Shuttle Laser Altimeter (SLA) experiment provides space-based heritage for the ICESat mission. SLA is a pathfinder experiment devoted to: (1) evaluating engineering and algorithm techniques for high-resolution, orbital laser altimeter observations of terrestrial surfaces, and (2) providing pathfinder scientific datasets of value in addressing global Earth System science issues (Garvin and others, 1998). The first and second flights of SLA characterized ocean, land, and cloud top elevation and vertical roughness in 100-meter diameter laser footprints spaced every 700 meters along a nadir profile. SLA is a hybrid instrument combining ranging electronics modified from the MOLA design (Zuber and others, 1992) with a high-speed digitizer used to record the backscatter return amplitude as a function of time (i.e., waveform). Processing methodologies developed from the Shuttle Laser Altimetry, SLA, missions (Garvin and others, 1998) and radar altimetry (Zwally and others, 1994) have laid a good background from which to produce operational algorithms to process the GLAS measurements and allow us to meet our science requirements.

Airborne laser altimeter heritage also provides experience in utilizing lidar waveforms for characterizing surface elevation and vegetation canopy height. Several implementations of airborne surface lidars have adapted bathymetric water depth sounding lidars in order to assess their ability to measure forest canopy height using green wavelength backscatter waveforms (Aldred and Bonner, 1985; Nilsson, 1996). A near-infrared, ND:YAG lidar system developed at Goddard Space Flight Center was specifically optimized to measure canopy vertical structure and the elevation of the underlying ground (Bufton and others, 1991; Blair and others, 1994). A scanning version of this system, the Scanning Lidar Imager of Canopies by Echo Recovery (SLICER), has been used to measure canopy structure of Eastern U.S. deciduous forests (Lefsky 1997; Lefsky and others, 1999) and Pacific Northwest fir stands (Harding and others, 1994; Harding, 1998; Lefsky and others, 1998; Means and others, 1999). The SLICER waveform measurements of canopy height and structure show strong correlations with ecologically important forest stand attributes such as above ground biomass and stem basal area. The

waveform data used to date to characterize canopy structure and ground topography beneath canopies were acquired using laser footprints on the order 10 m in diameter. Airborne lidar waveform measurements with footprints in a variety of sizes and configurations have been used to monitor topographic change at Long Valley Caldera, California (Hofton and others, 2000). The Goddard airborne lidar system has also been used in a large-footprint profiling mode (Bigfoot) to collect data over the Greenland ice sheet and vegetated terrains of North America that emulate the waveform data to be acquired by ICESat.

2.1.2. Instrument Characteristics

The GLAS instrument uses an Nd:YAG laser with 1064 and 532 nm output. The elevation measurements are determined from the round-trip pulse time of the infrared pulse, while cloud and aerosol data are extracted from the green pulse. The instrument is nadir-viewing with a pointing accuracy of 20 arc seconds. The post-processed pointing knowledge is expected to be 1.5 arc seconds. At a nominal altitude of 600 km, the 375 microradian field-of-view telescope has a spot-size of 70 $\pm$ 10 m in diameter. The pulse frequency is 40 Hz, which results in spots that are separated by 175 meters center-to-center on the ground. The requirement for knowledge of post-processed position is better than 5 cm in the radial direction, and better than 20 cm horizontally.

The platform is to be placed in a 91 day ground track repeat cycle after the initial 90-day verification phase). This will allow for adequate measurements to be able to calculate the required accuracy of mean elevation changes after averaging over 100 km^2.

The GLAS instrument algorithms are described in detail in McGarry and others (in process). The following excerpts give enough information so that the reader can understand the algorithms described in the following sections. The laser altimeter on ICESat will collect about 4,500,000 1-ns samples for each transmitted laser pulse. It will not be possible to telemeter this entire data stream to Earth, so on-board processing of the GLAS waveforms will be essential to retrieve the desired data. 544 samples will be telemetered over ice sheet and land surfaces and 200 samples over sea ice and ocean surfaces. The GLAS on-board altimetry algorithm was developed to maximize the chance that the telemetered data will include the ground return. This meets the science requirement of being able to maintain measurements over 3 deg slopes and gives a large enough range window (81.6 m over land and land ice and 30 m over sea ice and ocean) to measure all levels of expected roughness.

The algorithm does not include an acquisition or tracking phase, but relies on a simpler scheme using a Digital Elevation Model (DEM) to select the region of the echo waveform to be searched for the ground return.

The altimeter algorithm bounds the search area of the digitized waveform using a priori information stored in an onboard Digital Elevation Model (DEM). The DEM is interrogated once per second to determine min and max values of the range window and the type of surface (ocean, sea ice, land, or ice sheet), which will determine the number of elements in the returned waveform and the vertical range it covers.

The digitized waveform information within this DEM bounded region (called the Range Window) is filtered through 6 matched filters (in the hardware electronics) to maximize the probability of finding echoes from sloped or rough terrain and minimize the probability of selecting cloud returns. A separate threshold is determined for each of the filtered waveforms to distinguish the signal level from that of the noise. The thresholds are set as a function of the noise using a 1 km region of the digitized waveform beyond the end of the Range Window where we are sure that no laser light is reflected back to affect the calculation.

Because the echo from the ground is expected to be the last local maximum in the Range Window, the algorithm searches for the surface echo backward in time from the end of the Range Window towards the start. The pulse defined by the first threshold crossing (from below the threshold to above) to the next corresponding threshold crossing (from above the threshold to below) is selected for each filter (providing that such a pulse exists for each filter). A weighting factor that is a function of pulse attributes is used to determine which filtered output is most likely to contain the surface echo.

Once the filter has been selected, it is used solely to determine where the start of the received waveform digitized data sampling will be. The data to be sent to the ground are obtained directly from the received digitizer waveform. 1000 one ns samples are stored on-board from which to select the telemetered return. The samples can be sent at full resolution or compressed to enlarge the measured range span to cover tall trees and large topographic relief. Two different compression ratios can be used, one for the beginning and one for the end of the waveform. The sample, at which the compression ratio changes, is also input. The compression ratio allows one to increase the range window over land if requested in order to assure that all canopy heights are included. Nominally the 81.6 m range window should be adequate, but for special requirements the compression option will be turned on.

2.1.3. Major hydrosphere mapping targets of ICESat mission

The following subsections talk to the properties of ice sheet, sea ice, land, and ocean, and what quantitative measurements will help us understand global climate warming and the interactions with these ecosystems and our environment.

2.1.3.1. Ice Sheets

The following description of the surface properties of ice sheets is from C. Bentley's contribution to Brenner and others, 2003.

There are only two major ice sheets in the world, one on Antarctica and one on Greenland. A good general description of the Antarctic ice sheet can be found in a book by Fifield (1987). The Antarctic ice sheet is composed of two unequal parts. The larger portion (10.35 million km^2) lies in East Antarctica, where it reaches a maximum central elevation of just over 4000 m. This part of the ice sheet is mostly terrestrial, that is, it rests on a bed that would be mostly above sea level if the ice were removed and isostatic rebound allowed to taking place. The massive Transantarctic Mountain chain, which stretches from Atlantic to Pacific across the continent, separates East Antarctica from West Antarctica (the two portions lie principally in the Eastern Hemisphere and the Western Hemisphere, respectively). The West Antarctic ice sheet itself comprises three very different provinces: the "inland ice", the ice shelves, and the Antarctic Peninsula. The inland ice, which is the main part of the ice sheet, 2 million km^2 in area, is mostly marine (i.e. it rests on a bed that would be sea floor in the absence of the ice) and attains a surface height of 2300 m. Abutting it on the Atlantic and Pacific sides are two large floating ice shelves, each about 0.5 million km^2 in area. The Antarctic Peninsula (also about 0.5 million km^2), which stretches far northward from the main body of Antarctica toward South America, is an area of extensive mountainous terrain and complex ice cover, with several merging small ice caps, ice shelves, and outlet glaciers, and many ice-covered offshore islands.

The Antarctic ice sheet is in places over 4000 m thick; it contains 91% of the world's ice and 70% of the world's store of fresh water. Much of Antarctica is technically a desert - each year more than half of its surface receives in snowfall less than the equivalent of 100 mm of water. Essentially no melting of the snow occurs (except close to the more northerly margins) even in summer and each year a new layer is added. As the snow layers are added, deeper layers become compressed, eventually being transformed into ice. Gravity forces the ice to flow downwards and outwards towards the coast, where it is eventually lost to the ocean, principally by calving of icebergs.

The Greenland ice sheet (1.73 million km^2) is a single, bowl-shaped unit whose bed in the interior of Greenland lies more or less at sea level. The ice flows outward through the mountains that ring the island in a series of outlet glaciers, most of which reach the ocean either directly, or, more often, through fjords that connect to the ocean. Snowfall rates in the interior and melt rates around the periphery are greater than in Antarctica. As it is eight times smaller than the East Antarctic ice sheet it has approximately an eight-fold larger perimeter: area ratio. Because of this and the relatively high melt rates surface melting is a much more important

component of the overall ice-mass balance in Greenland than in Antarctica. There are few ice shelves in Greenland.

Slope Characteristics: The speed of outward ice flow from an ice sheet is sufficient large to balance the incoming snowfall (when averaged over many centuries). In this way, ice sheets are able to maintain approximately parabolic profiles. The central regions are consequently very flat, with gradients on the order of 1:1000. Toward the ice margin, surface slopes and flow speeds are higher, the ice is thinner, and stresses from flow over the irregular sub-glacial bed makes the ice surface more undulating. Within 200-300 km of the coast, the ice may become channeled, either through peripheral mountains where outlet glaciers develop, or through ice streams, fast-flowing zones within the ice sheet. Here the slopes are highly variable, from as much as 1:10 where the ice is flowing slowly to as little as 1:1000 on the fast-flowing, low-gradient ice streams. The coastal regions, with their widely variable slopes, are of particular importance in the context of global change, because it is here that any reaction of the ice sheets to changes in climate will first appear. More than half of Antarctica has gradients less than 1:300 and 90% has gradients less than 1.5%. Only 3% of the ice sheet, in the marginal areas, exhibits gradients larger than 3% (Drewry and others, 1985). Greenland has a similar distribution of slopes, except that the ratio of the marginal areas to the total is several times larger.

Most of the ice discharging from the Antarctic ice sheet flows into the sea. In many places it floats and continues to move outward in the form of ice tongues and coalescing ice shelves, which spread out under their own weight. The largest ice shelves are hundreds of kilometers across and exhibit changes in ice thickness on the order of 1 m per kilometer. Since the ice shelves float in hydrostatic equilibrium, this produces surface slopes on the order of 1: 10,000.

Roughness Characteristics: At first glance the surfaces of the ice sheets appear smooth, but in reality they are roughened in three fundamentally different ways. On the smallest scale there is the roughness caused by the wind and variations in the rate of snow accumulation, which comprises irregular features called "sastrugi" and "snow dunes" (Kotlyakov, 1966; Doumani, 1967). Sastrugi are erosional or erosional/depositional features that vary widely in size, both vertically and horizontally, depending on the wind characteristics and history in a particular region. In many areas the irregularities of the surface are 0.1 m or less in height, with typical horizontal wavelengths on the order of several meters. Over parts of the interior of Antarctica, however, the sastrugi can reach heights as great as a meter (e.g. Endo and Fujiwara, 1973); horizontal wavelengths are larger, although not necessarily proportionally larger. Snow dunes are accumulational features that are somewhat larger than sastrugi - they can be up to several meters in amplitude and tens of meters in wavelength. These physical features are larger than the meteorologically defined "surface roughness parameter", which is the height above the mean

surface, at which the wind speed is zero. This latter surface roughness parameter typically has a value of 0.01 m over a snow surface with sastrugi (Paterson, 1994, p. 62-63), because of the streamlined shapes of the sastrugi and dunes.

Roughness due to sastrugi is anisotropic; sastrugi ridges are elongated in the direction of the wind, so the roughness characteristics are different along, and normal to, that direction.

An absence of surface roughness can also be an important characteristic of the ice-sheet surface. In particular, a smooth, glazed surface probably represents a region that has been free of snow accumulation for several years or more (Watanabe, 1978).

The second type of roughness has much longer wavelengths and has two different causes. First, there are the undulations of the surface that result from the flow of the ice over topographic irregularities in the bed. Although the flow characteristics of the ice are such that the vertical scale of the relief of the surface is much less than that of the bed, surface relief nevertheless exists and in many places is pronounced. Amplitudes of this relief are commonly a few meters to tens of meters, with horizontal wavelengths of hundreds of meters to many kilometers. The thickness of the ice sheet modulates the surface relief in two ways - the thicker the ice, the smaller the amplitude of the surface relief and the greater its dominant horizontal wavelengths. The ice sheet acts like a band pass filter - subglacial relief of wavelengths short compared to the ice thickness is damped by the strength of the ice sheet, whereas very long wavelengths are attenuated by the plastic flow of the ice. Second are the megadunes, identifiable on AVHRR and SAR images, which are comparable in size to the flow-produced undulations but more regularly sinusoidal in form. Megadunes, which are believed to be produced by atmospheric standing waves, cover about 20% of the Antarctic ice sheet. They have not been recognized in Greenland.

It is the long-wavelength roughness, which grows more pronounced in the coastal regions where the ice is thinner and moving faster, that causes one of the most serious problems for radar altimetry, with its wide beam. The surface undulations are such that often the nearest point on the surface to the satellite carrying the altimeter is displaced substantially from the nadir point on the surface, or even from the nearest point on the mean sloping surface. Furthermore, the radar altimeter commonly records overlapping returns from two or more topographic high points. Under most circumstances the surface relief is far too complex, and the sampling from the radar altimeter too sparse, for it to be possible to deconvolve the radar returns to extract the real surface topography.

The third type of roughness stems from cracks in the surface - crevasses. These develop anywhere that the stresses in the ice from variations in flow exceed the breaking strength of the ice in tension. They are caused by lateral variations in flow speed and/or direction as the ice

flows over basal topography, around bends in a subglacial channel, or through regions of rapid acceleration (longitudinal or transverse). Crevasses vary widely in scale, from millimeters to tens of meters across and from tens of meters to kilometers long. Spacings between crevasses are characteristically on the order of one or two hundred meters. Like the undulations, crevassing has a strong tendency to be more pronounced in locations nearer to the coast. In extreme cases, (e.g. the Jakobshavns ice tongue in Greenland) the crevassing is so severe that the surface becomes a jumbled series of pinnacles - seemingly more crevasse than ice.

Even a moderately crevassed surface will destroy the coherence of a back-scattered pulse from a satellite radar altimeter if the crevasses are open, because even a single crevasse can provide a multitude of reflecting (or diffracting) points. Furthermore, much of the strength of the signal is lost by being scattered out of the return beam.

Surface and Airborne Observations: In view of the extensive oversnow traverses that have been conducted in Antarctica and Greenland it is perhaps surprising that so little quantitative information has been published on surface roughness. Comments often appear in traverse reports, but they are typically qualitative and subjective, relating principally to the difficulty caused to travel by large and hard sastrugi.

A few studies of small-scale roughness from surface measurements do exist, principally from work of the Japanese Antarctic Research Expedition. The most comprehensive is that of Watanabe (1978) in central Queen Maud Land, Antarctica; that work was extended eastward to Enderby Land by Furukawa and others1992. The emphasis of these analyses has been on the categorization of the wind systems, particularly of the katabatic winds that dominate the East Antarctic slope region and control the orientation of the sastrugi. Airborne Topographic Mapper data were used by van der Veen and others (1998) to determine the surface roughness over large areas in Central Greenland.

Measurements of the undulations related to the subglacial topography were limited to two-dimensional profiles when the only source was the surface traverses. Analyses and theoretical studies led to various quantitative relationships between surface and basal topography (Robin, 1967; Budd, 1970; Budd and Carter, 1971; Hutter, 1981; Whillans and Johnsen, 1983; Reeh and others, 1985). When the results of extensive airborne radio-echo sounding became available, McIntyre (1986) showed the importance of extending the study into three dimensions. He found that wavelengths of two to ten times the ice thickness tend to predominate and that the energy of the surface-relief spectra increases markedly towards the coast.

Measurement Objectives: There are two principal reasons for measuring the small-scale roughness (the first type). In the first place, the interaction between the rough surface and the wind moving over it is an important aspect of boundary-layer meteorology. Furthermore, the

size and time-history of the surface roughness of the first type discussed above is a measure of the magnitude and history of strong winds. Secondly, the roughness is an important limiter on the accuracy of the surface-height measurements. Roughness on this scale will be reflected in the broadening of the pulse and will be indistinguishable, by that measure alone, from a mean surface slope within the footprint. For research purposes the roughness will have to be separated from the slope after the fact, when the surface elevations (and hence slopes) have been mapped.

The second type of roughness is important for the information it will reveal about ice dynamics and the subglacial topography. Those longer-scale irregularities of the surface will be revealed by the main surface-elevation mission.

It is unlikely that any quantitative measurement of crevasse characteristics (the third roughness type) will result from the GLAS measurements. Nevertheless, the occurrence of multiple returns from the ice sheet will provide a warning of the presence of crevasses, which affect the accuracy of the basic height measurements.

2.1.3.2. Sea Ice

The polar oceans are, at least seasonally, covered by a thin, uneven sheet of sea ice. Although its thickness is small (a few centimeters to a few meters), sea ice has a profound influence on the physical, chemical, and biological characteristics of the oceans and the global climate system (e.g., Comiso, 1995). Because of the huge area, hostile weather conditions and long period of darkness, satellite remote sensing systems have been the major tools for mapping and monitoring the sea ice, with emphasis on microwave sensors, both active and passive (e.g., Carsey, 1992; Comiso, 1995; Perovich, 1996).

Sea ice is a complex material consisting of an ice matrix with inclusions of air, brine, solid salt and contaminants. It varies, spatially and temporally in thickness, composition, snow cover, wetness, and surface roughness. Sea ice can be classified by age (typically new ice, first-year ice, and multi-year ice), by structure (e.g. frazil, grease ice, nilas, pancake, columnar etc), or by the degree of deformation. During the winter, the surface is generally covered by snow, which in summer may melt to form slush and melt ponds. Particularly in the Antarctic, where the ice is thin, heavy snow loads can depress the ice sufficiently to permit flooding of seawater above the ice/snow interface.

Sea ice affects both the overlying atmosphere and the underlying oceans in several ways. It is a strong insulator, limiting heat exchange between ocean and atmosphere, it modulates the exchange of momentum between atmosphere and ocean, and with its high albedo it strongly affects the absorption of radiant energy by the Earth. During formation, sea ice rejects salt, and it produces fresh water when melting, thus affecting the salinity structure of the ocean with important ramifications for deep convection, bottom-water formation, and blooms of ocean

biological productivity associated with the ice edge in spring. In addition to these characteristics that influence weather and climate in ways that are still poorly understood, sea ice obstructs shipping, modifies submarine acoustics, and provides an environment essential to the survival of a wide variety of polar animals.

Sea-Ice Surface Characteristics: The most notable sea-ice deformation features are ridges, rubble fields, ice rafts, and open-water leads. Ridges can be long quasi-linear features extending for several kilometers, but they generally are sinusoidal and extend for several hundred meters. Repeated ridging causes rubble fields. Ridges usually are a meter to a few meters high and their appearance depends on their age. First-year ridges are composed of piles of very angular ice blocks, while multi-year ridges are typically well rounded, hummocky features with few, if any, voids.

On a somewhat smaller scale are the broken and rafted ice fields. Broken ice fields are formed from refrozen ice blocks and their characteristic vertical roughness ranges from a few centimeters to a meter. Rafting occurs when convergence causes one sheet of ice to override another, causing linear or sinusoidal features sometimes extending several kilometers, with vertical relief of less than a meter. Often, however, finger rafts occur, which have a distinctive square wave appearance. Wind-induced snow dunes and snowdrifts also frequently occur on snow-covered sea ice. These typically have vertical dimensions of a few cm to tens of cm.

On a very small scale, roughness is determined by the crystal structure of the surface snow or ice layer. Tucker and others, 1992 summarize the standard deviation and correlation length values published in the literature. The surface roughness usually ranges from 0.05 to 2 cm over a correlation length of 0.5 to 20 cm.

Perovich (1996) provides the most recent and comprehensive summary of sea ice optical properties. Albedo values quoted in this section are from Grenfell and Perovich, 1984. The spectral albedo of snow and sea ice is characteristically highest at visible wavelengths, decreasing strongly in the infrared because of increasing absorption by ice and water. Variations are due primarily to differences in the air bubble density, crystal structure, and fresh water content of the upper layer of the ice.

For sea ice, which is covered by fresh, cold snow, albedo is generally high. For sea ice covered by cold snow near-infrared (NIR) albedo can be as high as 0.7[1]. The aging of snow results in an albedo decrease at all wavelengths, because of the increase of grain size and rounding of the grains. This decrease is especially pronounced in the infrared (albedo for melting snow = 0.5), where absorption by ice and water is very large and the upward scattered radiation is very sensitive to the scattering properties of individual grains at the surface.

Bare sea ice has lower albedo values and exhibits more pronounced specular behavior than that of ice covered by snow. Drained white sea ice, which is located above the local freeboard level, has only slightly smaller albedos (about 0.4) than melting snow. Blue ice occurs when the surface becomes saturated with meltwater, which fills in near-surface irregularities so that backscattering is reduced. When blue ice develops into melt ponds, it can reduce the infrared albedo down to the specular reflection limit of 0.05, and it remains constant for the ponds until they refreeze or drain completely. The absorption coefficient of sea ice is very close to that of seawater, therefore the light penetration is negligible at NIR wavelengths.

Multiyear ice has survived a summer melt season, with the attendant surface melting and brine drainage to form a well-developed surface-scattering layer with many air bubbles. Consequently, albedos are typically larger then first-year ice values (Perovich, 1996).

Most sea ice can be regarded as a nearly horizontal, rough surface. The roughness is an indication of the history of the ice, and strongly influences its drag coefficient and hence its response to winds. The surface elevation of flat regions is a close approximation to local sea-surface elevation, but slightly biased upwards, depending on the ice thickness. Sea-ice covered ocean also contains icebergs, with surface elevations significantly higher than that of the sea ice. The algorithms described in this document will be applied to GLAS data to provide estimates of sea-ice elevation and roughness, and of iceberg elevations.

2.1.3.3. Ocean

ICESat will spend most of its lifetime over the ocean acquiring a vast amount of information on sea-surface characteristics. The shape of the GLAS return-pulse waveform will be determined primarily by the surface-height distribution within the footprint, which is small enough to be affected by individual large waves.

Over distances of cm to a few hundred meters, the sea surface is roughened by waves and ocean swell, but over distances of many km, the sea surface is almost flat and horizontal. Nevertheless, surface slopes and long-wavelength undulations are present, caused by variations in Earth's gravity field, associated for instance with seamounts, ocean currents, and variations in atmospheric pressure and seawater density. Satellite radar altimeters have shown remarkable success in measuring sea-surface elevation and significant wave-height, and will continue to be the prime tool for this purpose. Because of its large effective footprint, a satellite radar altimeter averages the effect of the small-scale roughness in the information contained within the composite, 0.05 -0.1 second return pulse from which estimates of surface elevation and roughness are inferred. Consequently, the resulting sea-surface elevations can be used to study the longer-wavelength variability, and estimates of surface roughness are a statistical indication

[1] All albedo values in this section are at the wavelength of the GLAS system, i.e. 1.064 microns

of the wave height. Errors are primarily associated with orbit uncertainty, atmospheric effects, and noise in the instrument system. The noise effects require averaging of several return pulses (at least 1 second's worth) for highest accuracy, which limits along-track spatial resolution. There may also be a range-measurement bias, associated with asymmetry in the shape of ocean waves, which increases with increasing wave height.

2.1.4. Physics of the problem

2.1.4.1. Introduction

The GLAS system will use a pulsed laser to measure the precise range from the satellite to the terrain and to provide clues of the surface elevation distribution within the laser footprint. Average reflectivity of the surface at the monochromatic laser wavelength will also be obtained from the ratio of the transmitted and received energy.

The following sections will summarize the background on the waveform and timing of the backscattered laser signal. Assuming that the effect of forward scattering by clouds and aerosols is negligible the shape of the received signal is determined by the range distribution inside the laser footprint modulated by the local reflectivity and the incident beam pattern. Gardner (1982, 1992) and Tsai and Gardner (1982) have developed detailed analytical expressions (see Section 1.4.2.1) to describe the received pulse for simple ground target geometry. These expressions have been used to evaluate the performance of satellite laser altimeter systems (Gardner, 1992 and Harding and others, 1994) and to develop algorithms for GLAS data processing (Csathó and Thomas, 1995 and 1996). For complex terrain the received waveform can be computed by using the Goddard Laser Altimetry Simulator Software (Abshire and others, 1994).

2.1.4.1.1. Ice Sheet Elevation

The satellite laser altimeter makes three basic measurements: the range between the satellite and the surface footprint, the shape of the return waveform after reflection from the earth surface, and the laser power returned from the surface. The ice sheet elevation for GLAS is measured as the mean surface height of the laser footprint, which is the difference between the satellite height and the range between the satellite and the surface. The satellite height is determined from the orbit and is independent of the laser measurement. The range is measured by calculating the laser pulse travel time to the surface, correcting for atmospheric and instrument effects. The shape of the return waveform is affected by: the transmitted pulse; the surface height distribution within the footprint; atmosphere scattering; and the receiver. If the transmitted pulse is close to a Gaussian, the surface is a mean slope plus random height variations, and there is no atmospheric forward scattering, the return pulse shape will be very close to a Gaussian. Our test results show that fitting a Gaussian pulse to the waveform and then using the centroid of the Gaussian will help to diminish the effects of non-ideal conditions

including irregular surfaces and forward scattering when the fitting using only the gates near the pulse center.

2.1.4.1.2. Ice Sheet Roughness And Slope.

Our approach is based on the assumption that there is a spectral minimum in surface roughness that lies in the range of a few hundred meters and separates the wind-generated roughness at shorter wavelengths from the undulation generated by basal topography at longer wavelengths. That being the case, we can consider the surface within the footprint as characterized by a mean slope, which is a short segment of the long-wavelength undulations; superimposed on that slope is a large number of wind-generated bumps of short wavelength. Correspondingly, we make two calculations, based on the alternate assumptions of a smooth, linearly sloping surface and a rough flat surface. After more quantitative knowledge is gained of the slope from GLAS, we may be able to calculate the roughness using this.

We assume that the surface is a diffuse (Lambertian) reflector, that is the emerging radiance is constant for all directions in a hemispherical solid angle. The surface reflectivity is also assumed to be uniform within the 70 m footprint.

Effect of Roughness: We assume that small-scale roughness has a Gaussian distribution, which also implies that there are a sufficient number of bumps within the footprint to justify a statistical approach. Although there is no reason to suppose that this distribution of heights is realistic for the snow dunes and sastrugi that roughen the surface, since they tend to have a regularity of form and size within a small area (Doumani, 1967), there is no quantitative basis for any other assumption. It will require ground-truth experiments to provide a quantitative correlation between surface conditions and the roughness calculated from the GLAS algorithm.

Effect of Slope: For the purposes of algorithm development we assume a linear slope. Since the dominant wavelengths of surface undulations are generally over 10 km (McIntyre, 1986), this should be a good approximation across the 70 m footprint.

Combined Effect: There is no realistic way to ascertain from the shape of a single returned pulse to what extent the pulse-broadening has been caused by the roughness and to what extent by the mean slope, even though the pulse shapes are slightly different in the idealized, theoretical cases, because the distortion caused by deviations from our idealized assumptions will surely be large compared to that slight difference. We therefore make no attempt to separate the two effects; our data product will have two numbers stemming from alternate analyses of the same pulse. One will give Var(Δx), calculated on the assumption of roughness alone, and the other will give the mean slope, calculated on the assumption of a tilted, planar surface. Which is more nearly appropriate in a given situation is a matter that can only be determined by reference to ancillary information about the nature of the region observed.

2.1.4.1.3. Sea Ice Elevation And Roughness

Within each 70-meter GLAS footprint, incident near infrared (NIR) laser energy will be reflected to the receiving telescope with a time delay determined primarily by surface elevation and surface roughness (for the moment, we neglect the effect of forward scattering by clouds and aerosols), and intensity determined primarily by reflectivity of the surface and the energy beam pattern incident upon the surface. The average time delay of the return energy gives the average range to surfaces within the footprint, and the temporal variation of return-pulse intensity is a measure of the range distribution within the footprint modulated by local reflectivity and the incident beam pattern. The shape of the return pulse is smoothed by the detection system, limiting the information that can be retrieved. Moreover, forward scattering of laser energy in transit through the atmosphere will increase return-pulse spreading beyond that caused by surface roughness. Consequently, little is to be gained by overly sophisticated algorithms, and our objective is to extract the least ambiguous sets of information, and to identify them as objectively as possible.

The major sea-ice parameters determined from GLAS waveforms include elevation, surface slope and roughness, and surface reflectivity. Surface roughness is a statistical description of the surface, representing its deviation from a smooth reference surface (Ogilvy, 1991). The standard deviation of surface elevations from their mean is a good way to characterize the surface roughness of horizontal surfaces. The reflectance (ratio of reflected energy flux to the incident flux) measured by GLAS can be related to the spectral albedo of the surface (ratio of total upwelling irradiance and the total downwelling irradiance).

2.1.4.1.4. Ocean Elevation And Roughness

Each clear-weather GLAS return pulse will provide estimates of average surface elevation and of surface-height distribution within the corresponding 70-meter footprint, at a rate of 40/second. However, these footprints will, in general, cover less than one of the longer ocean waves, and it will be necessary to include information from many consecutive footprints to infer sea-surface elevation and wave height. Surface elevation will be obtained by averaging the elevation of these many footprints, and the maximum wave height will be given by the highest and lowest surface elevations inferred from the all the pulse widths for wavelengths less than twice the footprint diameter. The length of orbit track over which this “averaging” must be done will depend on the sea state, and it should be possible to calculate this length from the sea-state information that GLAS will provide.

2.1.4.2. Analysis Of Waveforms Obtained By Pulsed Laser Altimeters

Pulsed laser altimeters estimate the range to the terrain surface by measuring the round trip time-of-flight of a laser signal. The received signal is spread in time, in part due to the variation

of range between the laser firing point and the surface features. For statistically uniform, diffuse surfaces with uniform reflectivity the expected signal at the receiver output can be expressed as the convolution of the surface profile probability density with the flat diffuse target response (Gardner, 1982). For returns from the ocean surface the shape of the backscattered signal is closely related to the height probability density of the specular points within the footprint (Tsai and Gardner, 1982). The following description of the analytic expressions is adapted from Gardner (1992).

2.1.4.2.1. Analytic Expressions For Flat Or Uniformly Sloping, Terrain

The geometry of the model is illustrated in Fig. 6. The coordinate system is defined by the optical axis of the altimeter (A) and the line from the altimeter to the center of the Earth, which determines the direction of the z-axis. The x-axis lies in the plane defined by z and the optical axis and it is perpendicular to z, and y completes the right hand system. The origin of the coordinate system is at the intersection of the optical axis and the terrain surface (F).

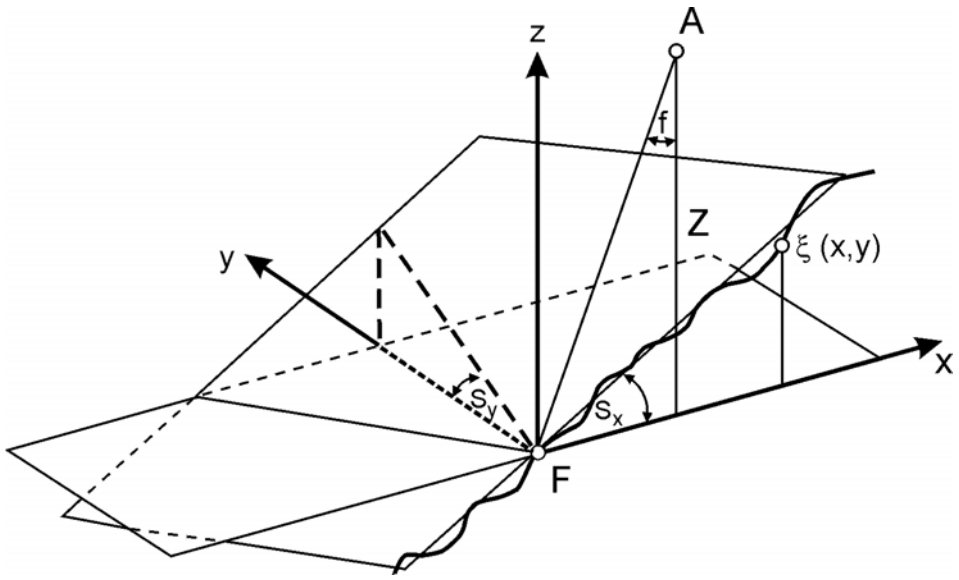

Fig. 6. Generalized geometry of the terrain.

The surface profile within the laser footprint is modeled as

$$\xi(\vec{r}) = \xi_0 + \vec{S} \cdot \vec{r} + \Delta\xi(\vec{r}) \qquad [1]$$

where $\vec{r} = (x, y)$ is the horizontal position vector on the ground, ξ_0 is a constant offset, $\vec{S} = (S_x, S_y)$ is the mean surface slope within the footprint, and $\Delta\xi(\vec{r})$ is the random microstructure of the surface.

2.1.4.2.2. Diffuse Terrain Types (Land, Snow)

Gardner (1982, 1992) analyzed the performance of pulsed laser altimeters for sloping, Lambertian (diffuse) terrain with quasi-random surface roughness and uniform reflectivity. By neglecting the effect of the forward scattering in clouds and aerosols and by assuming a Gaussian laser beam cross-section he obtained analytical expressions of the mean pulse delay and the RMS pulse width.

The expected mean pulse delay is composed from the propagation delay along the center from the laser beam, the additional delay resulting from the phase front curvature of the diverging laser beam, and the biases caused by the pointing jitter, that is

$$E(T_P) = \frac{2z(1+\tan^2 q_T)}{c\cos f} \left[1 + \left(1 + 2\tan^2(f+S_x)\right)\frac{Var(\Delta f_x)}{2} + \cos^2 f\left(1 + \frac{2\tan^2 S_y \cos^2 S_x}{\cos^2(f+S_x)}\right)\frac{Var(\Delta f_y)}{2}\right] \quad [2]$$

where T_p is the propagation delay measured by the pulse centroid time, c is the effective velocity of light (m/s), f is the off-nadir pointing angle of laser beam, S_x is the surface slope in (xz) plane, S_y is the surface slope in (yz) plane, z is the altimeter height above the terrain (m), q_T is the halfwidth divergence angle of the laser beam measured at the *1/SQRT(e)* point (rad), Δf_x is the pointing error parallel to the pointing direction, and Δf_y is the pointing error perpendicular to the pointing direction.

The mean-square pulse width is the sum of the effects of the system, surface roughness, beam curvature, off-nadir angle, and surface slope, that is

$$E(s_P^2) = (s_l^2 + s_h^2) + \frac{4Var(\Delta\xi)\cos^2 S_x}{c^2\cos^2(f+S_x)} + \frac{4z^2\tan^2 q_T}{c^2\cos^2 f}\left[\tan^2 q_T + \tan^2(f+S_x) + \frac{\tan^2 S_y \cos^2 S_x}{\cos^2(f+S_x)}\right] \quad [3]$$

where s_p is the RMS received pulse width(s), s_l is the RMS transmitted pulse width(s), s_h is the RMS width of receiver impulse response(s), and $\Delta\xi$ is the surface roughness (m).

2.1.4.2.3. Ocean Surface

The ocean surface is specular (non-diffuse) reflector. Tsai and Gardner (1982) computed the mean pulse delay and the RMS pulse width over specular surfaces by assuming Gaussian transmitted laser pulse shape and laser cross section. If the altimeter points at nadir ($f=0$, $\Delta f_x=0$, $\Delta f_y=0$), and Gaussian ocean surface statistics are considered, the statistics of the returned pulse

can easily estimated. For beam divergence angles larger than 10^{-2} rad the received waveform is highly asymmetrical. However, for the small divergence angles used on satellite laser altimeters the waveform is nearly Gaussian, and the expected pulse delay can be estimated as:

$$E(T_P) = \frac{2z}{c} + \frac{2z}{c}(\tan^{-2} q_T + 2S^{-2})^{-1} \quad [4]$$

where S = magnitude of $\vec{S}$.

Equation 4 differs from the reflection from the diffuse surface (equation 2) only by the presence of the S^{-2} term. Upon reflection from the ocean surface, the laser cross section is modified by the distribution of the surface slopes and the S^{-2} term accounts for this modification. This additional delay will introduce a small error into the ocean surface elevation. More research needs to be undertaken to determine the size of this error and its effect.

The RMS width of the received pulse is:

$$E(s_P^2) = (s_l^2 + s_h^2) + \frac{4}{c^2}\Delta\xi^2 + \frac{4z^2}{c^2}(\tan^{-2} q_T + 2S^{-2})^{-2} \quad [5]$$

If the beam divergence (q_T) is in the order of 10^{-3} rad or smaller, the last term will be approximately $(4z^2/c^2)\tan^4 q_T$. Then the surface roughness can be computed from the RMS pulse width of the return signal and known system parameters. Tsai and Gardner also derived expression for non-Gaussians ocean surface using the skewness coefficient to describe the non-Gaussian behavior. Due to the complex nature of the ocean returns the errors in the mean elevation and the significant wave height computed from individual returns can be quite large. To reduce the errors several waveforms should be averaged or "stacked" as it is recommended in 2.1.4.1.4.

2.1.4.2.4. Ice Sheet Elevation

The assumption is being made that the return will closely resemble a Gaussian and therefore a Gaussian pulse will be used to fit the waveform. The centroid of the Gaussian pulse will be used to calculate the range to the mean surface. This range then must be corrected for atmospheric delays using algorithms defined in the GLAS atmospheric correction ATBD, and the effect of time-varying tides removed using algorithms in the GLAS tide ATBD. Using this corrected range, the satellite position above the ellipsoid, and the off-nadir pointing angle; the surface elevation can be calculated using the algorithms defined in the GLAS laser location and surface profile ATBD.

2.1.4.2.5. Ice Sheet Roughness/Slope

Rough, Flat Surface**:** For horizontal surfaces $\vec{S} = \vec{0}$ and equation 1 becomes

$$\xi = \Delta\xi + \xi_0 \qquad [6]$$

With $S_x = 0$ and $S_y = 0$ from equation 3 we get

$$E(s_P^2) = (s_l^2 + s_h^2) + \frac{4Var(\Delta\xi)}{c^2 \cos^2 f} + \frac{4z^2 \tan^2 q_T}{c^2 \cos^2 f}(\tan^2 q_T + \tan^2 f) \qquad [7]$$

Satellite laser altimeters have a small off-nadir pointing angle and beam divergence. Therefore the third term in equation 7 can be neglected and we obtain

$$E(s_P^2) = (s_l^2 + s_h^2) + \frac{4Var(\Delta\xi)}{c^2} \qquad [8]$$

From equation 8 we finally have

$$sdev(\xi) = [Var(\Delta\xi)]^{1/2} = \frac{c}{2}\left(E(s_P^2) - s_l^2 - s_h^2\right)^{1/2} \qquad [9]$$

By using this formula the RMS surface roughness of a horizontal surface can be estimated from the received pulse width and from the known system parameters of the GLAS altimeter.

Sloping, Smooth Surface:

Set $Var(\Delta\xi) = 0$, and $f = 0$, from equation 3, we have

$$E(s_P^2) = (s_l^2 + s_h^2) + \frac{4z^2 \tan^2 q_T}{c^2 \cos^2 f}\left(\tan^2 q_T + \tan^2 S_x + \tan^2 S_y\right) \qquad [10]$$

Since,

$$\tan^2 S_x + \tan^2 S_y = \tan^2 S \qquad [11]$$

and for GLAS q_T is on the order of 10^{-5} radians, we can ignore the $\tan^2 q_T$ term and write,

$$E(s_P^2) = (s_l^2 + s_h^2) + \frac{4z^2 \tan^2 q_T}{c^2} \tan^2 S \qquad [12]$$

Then,

$$\tan S = \frac{c}{2z \tan q_T}\left(E(s_P^2) - (s_l^2 + s_h^2)\right)^{1/2} \qquad [13]$$

Or,

$$S = \tan^{-1}\left[\frac{c}{2z\tan q_T}\left(E(s_P^2) - (s_l^2 + s_h^2)\right)^{1/2}\right] \qquad [14]$$

2.1.4.2.6. Sea Ice Elevation And Roughness

Sea ice can be modeled by horizontal, randomly rough Lambertian (diffuse) surfaces, so equation 9 of the previous section applies.

In general, a sea-ice footprint will contain either a mixture of rough and smooth ice (or open water) or predominantly smooth ice (or open water). Less frequently, an entire footprint could be occupied by rough ice, or an iceberg, glacier, land ice, or land could occupy all or part of the footprint. In general, the average elevation of smooth or randomly rough ice (or open water) will be represented by the centroid of the latest, approximately Gaussian peak in the return pulse. Other surfaces in the footprint will have shorter ranges and their effect on return-pulse shape will be determined primarily by their surface height distribution. In some cases, such as when the smooth top of an iceberg fully occupies the footprint, the latest peak will not be smooth sea ice. However, this should be readily identifiable by its height above the geoid.

The key products to be derived for each GLAS "sea-ice" footprint are:

- Average elevation of sea ice or open water,
- Average elevation of features such as ice bergs that partly or entirely occupy a footprint,
- RMS sea-ice surface roughness,
- Average reflectance.

The sea-ice elevations will help improve the geoid, and surface roughness strongly influences both heat and momentum exchanges between the atmosphere and the ice. The reflectance is indicative of sea-ice albedo, which also affects energy exchange. Recent work with satellite radar-altimeter data indicates the possibility of estimating sea-ice freeboard, a proxy indicator of thickness, by comparing elevations of open-water leads with those of the intervening ice. Data from GLAS could be better suited to this application because of their small footprint. Even if identification of open-water waveforms is difficult, it might be possible to identify leads by the abrupt change in elevation between lead and sea ice. This is a research area, and is beyond the scope of a sea-ice algorithm, but if successful it would represent a major enhancement to our ability to monitor sea ice.

2.1.4.2.7. Ocean Elevation And Roughness

The proposed algorithm for ocean products will infer the average elevation (E) of a footprint, and the return-pulse width (above some threshold - initially the noise floor, but to be

adjusted after launch) as the elevation spread (E_{max} - E_{min}) inside the footprint. In general, the 70-m footprint will cover very few waves, often one or less. Consequently, it will be necessary to average many values of E to obtain the mean sea-surface elevation over the corresponding length of orbit track. As an example: Assume that E varies by plus or minus H meters because of the waves. H=1 would probably correspond to either a high sea state or longer waves or swell with amplitude of about one meter. If the variability of E is random, then the average elevation of 100 consecutive footprint elevations has wave-induced errors, ? E = 0.1 meters, appropriate to 2.5 seconds of data, or about 16 km of orbit track. Although this capability is poorer than that of satellite radar altimeters, it may offer improved information over specific regions, such as coastal regions and at high latitudes, and for geodesy. Moreover, it may be useful in assessing radar-altimetry errors associated with wave shape. One concern is the possibility of waves of appropriate length being aliased with the footprint spacing to introduce a bias to the average value of E.

Average elevation of the footprint (E) will be obtained from the centroid of the best-fit Gaussian to the return waveform. E_{max} and E_{min} will be inferred from the timing of the start and end thresholds of the return waveform, with the option of using similar information from the best-fit Gaussian if actual GLAS data reveal significant problems with forward scattering amplifying the tail of the return waveform.

The total area beneath the return waveform between the start and end thresholds (A) will be used to infer the reflectivity of the surface. Values of E, E_{max}, E_{min}, and A will be archived for each footprint location, and they will be strongly affected by local sea state. A mean elevation (E_m) over 1 full second will also be calculated as an average of all N values of E acquired during the second, and both E_m and N will be archived at the full GLAS data rate. The value of N will indicate regions of patchy cloud cover.

Within the one-second window, the extreme values of E_{max} and E_{min} give the full range of wave amplitudes for short wavelengths. However, a better representation of wave-height, and one more comparable to that derived from radar-altimeter data, could be obtained from the width of a composite return pulse formed by stacking many adjacent waveforms. Consequently, the GLAS science team will investigate a level 3 OCEAN product derived from many (N+1) footprints to take account of the wave height. Average values of E will be determined for orbit segments of fixed length, say 10 km, with final selection based on experience with actual data. The averaging process will require temporary storage of N+1 waveforms: the current waveform plus those for the preceding and subsequent N/2 footprints. The waveforms will be "stacked" to yield a composite waveform appropriate to the 10-km segment of orbit track. This composite waveform will be used to provide an alternate estimate of average elevation (from the centroid of its best-fit Gaussian) and an estimate of RMS wave height. From the RMS wave height the

Significant Wave Height (SWH) can be computed. The SWH is defined as the average of heights (from crest to trough) the highest one-third of the waves observed at a point. It is approximately equal to four times the RMS wave height (Tsai and Gardner, 1982). This would yield values of average E at the full rate of 40/sec, each with its own value of RMS wave height depending on sea state.

2.1.5. Variance Or Uncertainty Of Estimates

The estimation procedure will give quantitative values for the uncertainties in the parameters being estimated. However there are many surface, instrument, and atmospheric characteristics that will affect the shape of the return waveform. Our algorithms are based on several assumptions. This section examines the uncertainties in the physical quantities being calculated when these assumptions do not hold, and their effect on the ice sheet, sea ice, land, and ocean products.

The anticipated ranging error of single laser pulses comprises the time of flight measurement error and the clock frequency estimation error. Gardner (1992) developed analytic expressions to compute the variance of the centroid time and the received laser pulse width for the simple terrain surface pictured in Fig. 6. Gardner (1992) and Harding and others (1994a) used these expressions to determine the RMS range and pulse width errors to evaluate the expected performance of different satellite laser altimeter designs.

The analytic expression (adapted from Harding and others, 1994a) separates the sources of the received pulse centroid time variance into five components (impulse response, surface roughness, beam curvature, nadir angle and slope, and pointing uncertainty):

$$
\begin{aligned}
\mathrm{var}(T_p) &= F\mathrm{var}(s_l)/N_r + (FN_B + N_D)T^3/(N_s^2 \cdot 12 \cdot ?\,t) + ?\,t^2/12 + \\
&+ (F/N_r + 1/K_s)\,\frac{4\mathrm{var}(?\,\mathrm{var}(\,s(S_x)}{c^2\cos^2(f + S_x)} + \\
&+ (F/N_r + 1/(2 \cdot K_s))\,\frac{4z^2\tan^4 q_T}{c^2\cos^2 f} + \\
&+ (F/N_r + 1/(2 \cdot K_s))\,\frac{4z^2\tan^2 q_T}{c^2\cos^2 f} \cdot \left[\tan^2(f + S_x) + \frac{\tan^2(S_y)\cos^2(S_x)}{\cos^2(f + S_x)}\right] + \\
&+ \frac{4z^2(1 + \tan^2 q_T)^2}{c^2\cos^2 f}\left[\tan^2(f + S_x)\mathrm{var}(?\,v_x) + \frac{\tan^2(S_y)\cos^2(S_x)\cos^2 f}{\cos^2(f + S_x)}\,\mathrm{var}(?\,a_y)\right]
\end{aligned}
\qquad [15]
$$

where T_P is the propagation delay measured by the pulse centroid time,

F is the avalanche photodiode excess noise factor,

$var(s_l)$ is the variance of transmitted laser pulse width,

N_r is the mean signal photoelectrons,

N_B is the mean solar background photoelectrons,

N_D is the mean detector dark counts,

T is the detector integration time,

Δt is the time-interval-unit resolution,

K_S is the speckle signal-to-noise ratio = $\pi A_r[2 \cdot tan(q_T/\lambda)]^2$, where A_r is the receiver area, and λ is the laser wavelength,

$var(\Delta\xi)$ is the variance of the surface roughness,

c is the effective velocity of light,

f is the off-nadir pointing angle of laser beam,

S_x is the surface slope in (xz) plane, and S_y is the surface slope in (yz) plane,

z is the altimeter height above the terrain,

q_T is the halfwidth divergence angle of the laser beam measured at the *1/SQRT(e)* point,

Δf_x is the pointing error parallel to the pointing direction, and Δf_y is the pointing error perpendicular to the pointing direction.

The first four components in equation 15, that is the impulse response, the surface roughness, the beam curvature, and the geometric component dependent on the off-nadir angle of the laser beam and the slope of the surface, account for effects that cause pulse spreading in time of the received pulse. Note, however, that equation 15 does not include the effects of pulse spreading by forward scattering of the laser pulse by thin clouds and aerosols. With increased spreading of the pulse, range errors are increased because the centroid of the broad pulse is less accurately determined than that of a narrow pulse, given the same total energy, due to a lower peak signal to noise ratio.

These pulse spreading components are dominated by the photon noise. The photon noise contributions are inversely proportional to the mean signal photoelectrons (N_r), which is the number of photoelectrons detected per laser pulse:

$$N_r = \left(\frac{E_r \eta}{h\nu}\right)\left(\frac{A_r}{z^2}\right)\tau_{sys}\tau_{sys}^2\left(\frac{r_{surf}}{\Omega_{surf}}\right) \qquad [16]$$

where E_r is the transmitted laser energy,

η is the quantum efficiency of the detector,

$h\nu$ is the photon energy

A_r is the telescope area,

z is the range from the spacecraft to the Earth surface,

τ_{atm} is the atmospheric transmission,

τ_{sys} is the system transmission,

Ω_{surf} is the surface scattering angle, and

r_{surf} is the surface diffuse reflectivity.

For GLAS values the average number of photoelectrons received is expected to be typically 5,000-40,000. Link margin calculations indicate high SNR for the GLAS system. For example, in the case of moderately sloping ice/snow terrain (slope=3^o, reflectivity=0.6), the estimated link margin is 14.5 dB at night and 13 dB in the daytime. This SNR is high enough to obtain reliable range and surface roughness measurements even in case of large changes in surface albedo and roughness, and atmospheric transmission variability due to aerosol and cirrus cloud scattering process (Bufton, 1989).

The pulse spreading components also include the speckle noise contributions. The speckle noise effects are inversely proportional to K_s, which is the ratio of the receiver aperture area to the speckle correlation area. According to Bufton and others (1982), speckle noise is negligible for the GLAS system because of the large number of spatial and temporal speckle cells averaged during each individual range measurement.

The final component in equation 56 is sensitive to laser pointing angle uncertainties. For small pointing uncertainties Bufton and others (1982) approximated the range error due to this component by

$$\Delta Z = Z \Delta f \tan(S + f) \qquad [17]$$

For the GLAS system both the pointing uncertainty (1.5 arcsec) and the normal off-nadir pointing angles (< 1 deg) are small and therefore the ranging error due to the pointing uncertainty will be dominated by the effect of surface slope.

Gardner (1992) also derived an analytical expression similar to equation 56 for estimating the variance of the received pulse width.

To evaluate the performance of the waveform algorithms the analytical expressions and laser altimetry simulations will be used to compute the RMS range error and RMS pulse width errors of the GLAS system. These errors will be estimated over different types of ice sheet, sea ice, ocean and land topography and they will be analyzed in a similar fashion as it was reported in Gardner 1992, and Harding and others 1994. The algorithm described in the theory section and the analytical expression presented in this section are valid in cases of horizontal, linear sloping, isotropic, and stationary rough surfaces, uniform Lambertian reflectivity, and Gaussian laser beam far field pattern and atmospheric effects are neglected. Further research should be undertaken to analyze the errors introduced by the deviations from this ideal case or by distortions caused by the atmosphere.

2.1.6. Validation of Algorithms

2.1.6.1. Validation of Sea Ice Algorithm

The algorithm has been tested by computing laser waveforms for various sea ice models using the Goddard Laser Altimeter Simulator (Abshire et al., 1994 and notes for version 3.8). The simulator program derives altimeter return-pulse waveforms in a simplified two-dimensional (height versus along-track distance) measurement geometry. The waveform is computed as it propagates to the terrain surface and back to the altimeter receiver. The simulator's receiver includes a telescope, an optical bandpass filter, either a photomultiplier or an avalanche photodiode optical detector (Si APD), a low pass filter, a timing discriminator, a time interval unit and a waveform digitizer. Simulation does not model the effects of atmospheric refraction or scattering. The terrain surface is assumed to be a Lambertian reflector, and its reflectivity and height can be specified for every centimeter of along-track distance. For details on the operation of the simulator see Abshire and others, 1994. Examples of computed waveforms are presented in Fig. 7 and in Csathó and Thomas (1995).

For evaluating the surface roughness algorithm we used the icex.dat sea-ice data set distributed with the GLAS simulator software (Abshire and others, 1994). The surface elevations were measured by an airborne laser altimeter every 1 m along a 110-km profile on May 20, 1987, north of Greenland. Surface roughness was computed from surface elevations and from simulated GLAS waveforms for several different flight segments to evaluate the performance of the estimator. The different stages of the simulation are illustrated in Fig. 7.

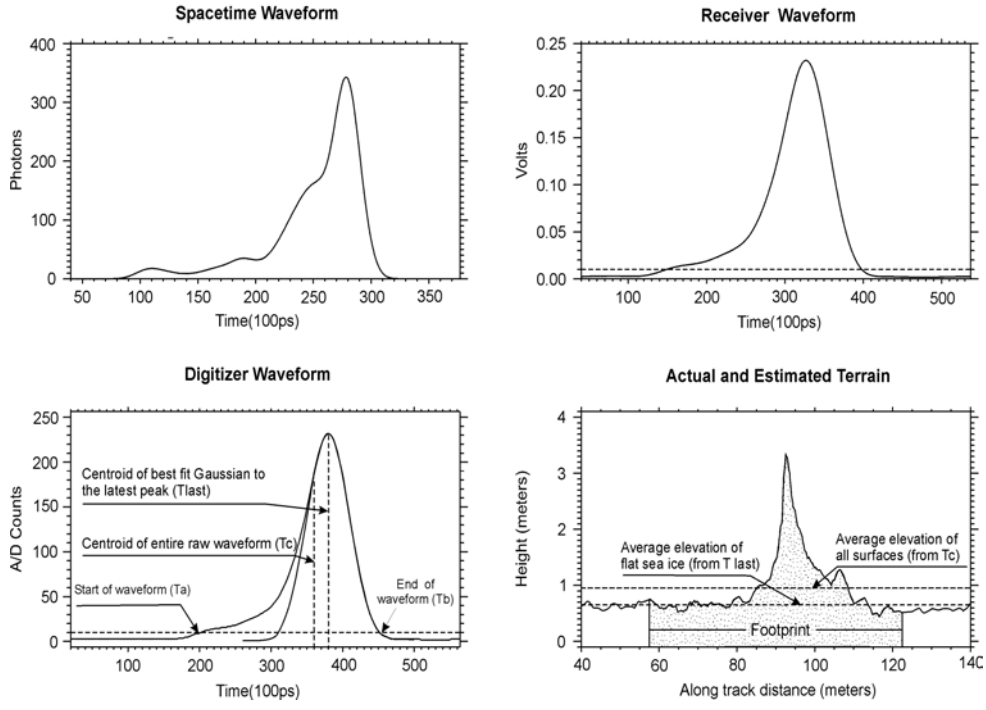

Fig. 7. Validation of sea ice algorithm, stages of waveform simulation

The spacetime waveform (Fig. 7, upper left) shows the laser pulse shape after it is reflected back from the terrain to the receiver. The largest peak is caused by the photons reflected from the nearly horizontal sea ice comprising most of the footprint (Fig. 7, lower right). The small peaks and 'shoulders' on its left are associated with the photons reflected back from the ridges. The spacetime waveform is further processed by the simulator to model the influence of the receiver and the background noise. The smooth electrical waveform emerging from the receiver (upper right) has an asymmetric shape and a single peak associated with the flat sea ice. The final, digitized waveform (Fig. 7, lower left) is used as input for the range and surface roughness computation. Here the average surface elevation is estimated from the centroid time delay, while the centroid of the last Gaussian shaped peak provides a very precise measure of the elevation of the flat sea ice (Fig. 7, lower right).

For the example shown in Fig. 8 the surface roughness computed from the laser-altimeter waveforms compares well with the surface roughness derived directly from the elevation. However, the algorithm generally underestimates the roughness of highly ridged areas, where surface is not "stationary". This happens when ridges are located in the outer part of simulated footprints, because the pulse spreading is determined by the within-footprint elevation profile weighted by the normalized cross section of the laser beam (Gardner, 1982). Ridges located away from the footprint center have smaller weight and therefore produce less pulse spreading.

Soon after the ICESat launch, we plan aircraft measurements of sea-ice topography at very high spatial resolution (using the conical-scanning Airborne Topographic Mapper (ATM)), which will provide a detailed description of the sea-ice surface within many GLAS footprints. Data products derived by the GLAS sea-ice algorithm will be compared with equivalent products derived from the detailed mapping. These flights will probably be conducted out of Thule Air Force Base in northern Greenland in conjunction with underflights to validate GLAS performance over the ice sheet.

2.1.6.2. Validation Of Ocean Algorithm

The ocean algorithm is being tested, using the same approach as described in the previous section, by using waveforms from airborne laser-altimeter measurements of ocean topography. First the surface elevation and surface roughness are estimated from each individual waveform. Then the average surface elevation and the significant wave height are computed from the "composite" waveforms. After launch, GLAS ocean products will be validated against equivalent products derived from satellite radar-altimeter data at locations where the orbits cross at approximately the same time.

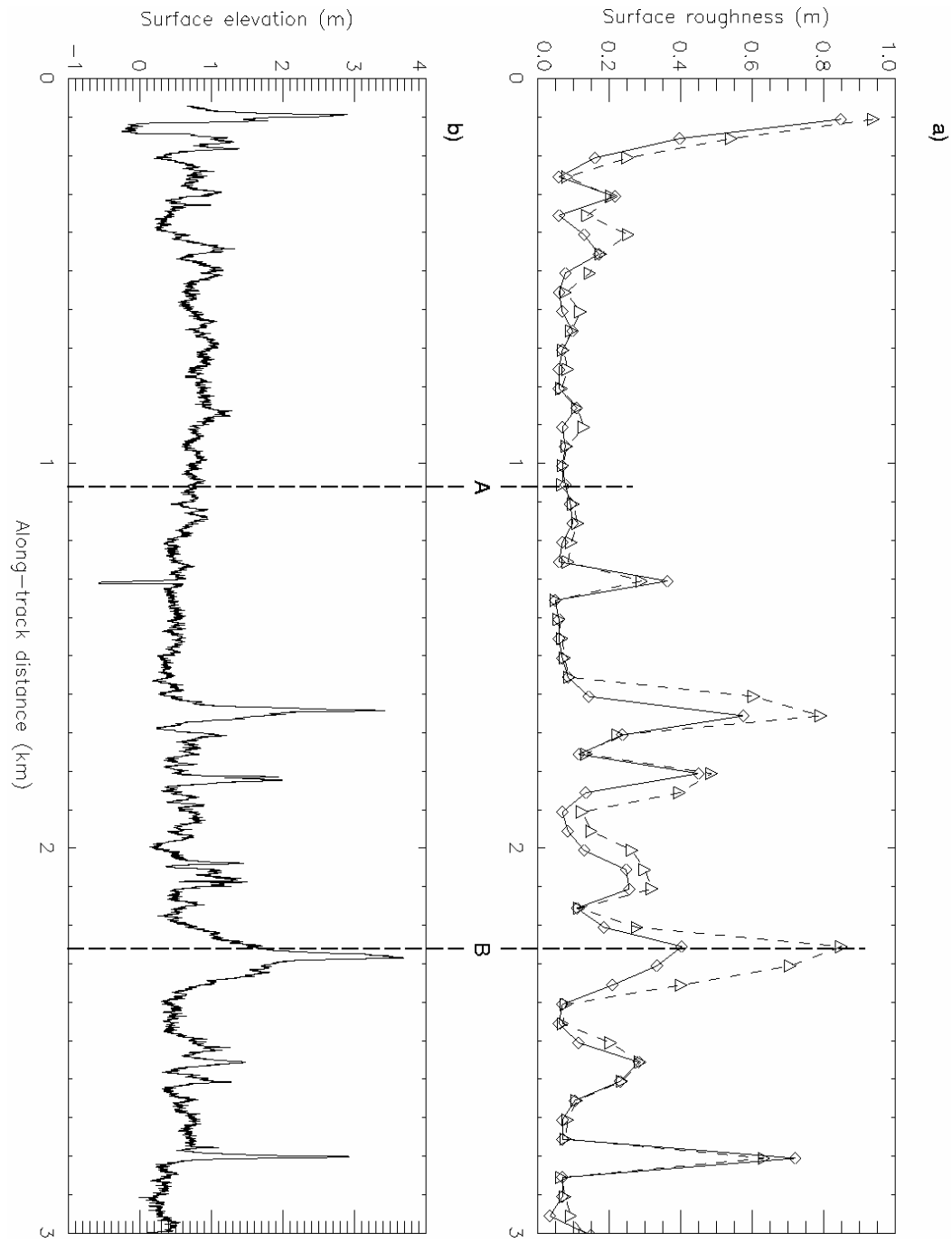

Fig. 8. a) Comparison of surface roughness computed from laser-altimeter waveforms (solid line with diamonds) and from surface elevation (dashed line with triangles).
A uniform surface reflectivity of 0.8 was assumed during the waveform simulation. b) Measured surface elevation profile from airborne laser-altimeter data

.

2.2. Mapping Surface Elevation Changes in Antartica – Calibration and Validation of the SOAR Laser Altimetry System and Science Applications

2.2.1. Introduction

The mass balance of ice in Antarctica is a prime need in science. The ice sheets are major variables in the global budget that controls sea level. It could be that thinning of the ice sheets accounts for the current rate of rise of sea level. There is a limited suite of techniques available for measuring mass-balance in Antarctica. A report is presented on the first of intended repeat surface mapping from an aircraft with GPS position determination and a downward-looking laser ranger. This method has the great merit of being precise and of covering large regions. Moreover, laser flights are used to make topographic maps and describe the shape of unusual portions of the ice sheet. The detection of special surface features raises the possibility of some mechanical understanding of ice sheet change.

Laser altimetry is expected to solve many central problems in Antarctica. A major concern is how ice thickness may be changing and affecting global sea level. A deeper issue is locating the source of ice thickness change and determining its propagation style so that the cause and effect of changes may be deduced. Studies have shown laser altimetry to be a valuable tool in mapping and monitoring glacier thickness in Alaska (Echelmeyer and others, 1996; Adalgeirsdóttir and others, 1998) and Greenland (Csathó and others, 1995a, 1995b, 1996a, 1996b, 1996c; Krabill and others, 1995; Garvin and Williams, 1993; Krabill and others, 1999). The use of laser altimetry to monitor changes occurring in Antarctica is the subject of the present contribution.

This section presents the results of the first precision airborne laser altimetry in Antarctica. First flights were conducted during the 1997-98 austral summer. Repeat flights were performed in January 2000. Data from the first flights have been used to make surface maps of four fast-flowing regions of West Antarctica. There are numerous flight-to-flight crosses with one another to assess repeatability. Other flights cross areas surveyed using snowmobile mounted GPS to assess system accuracy. Long baseline accuracy is determined using flights that go near mass-balance measurement sites known as coffee-cans. Repeat surveys are used to determine elevation changes over time.

2.2.2. Study Sites

Unique features of West Antarctica, known as ice streams, are the focus of this study (Fig. 9). The ice streams are the major conduits that drain West Antarctica. They are located to the east of the Ross Sea meeting the Ross Ice Shelf along the Siple Coast. The ice streams are broad, typically around 50 km, and long, usually greater than 500 km, zones of rapid water-lubricated flow. Unlike mountain glaciers, the ice streams do not follow bedrock troughs. The

ice streams are separated by ice ridges that may be frozen to underlying bedrock. The details of how ice streams operate are not well understood. However, some of these ice streams are known to be changing very quickly with time (Hamilton and others, 1998; Bindschadler and Vornberger, 1998; Joughin and others, 1999; Hamilton, pers. comm.). The cause for the changes is a topic of some debate within the science community.

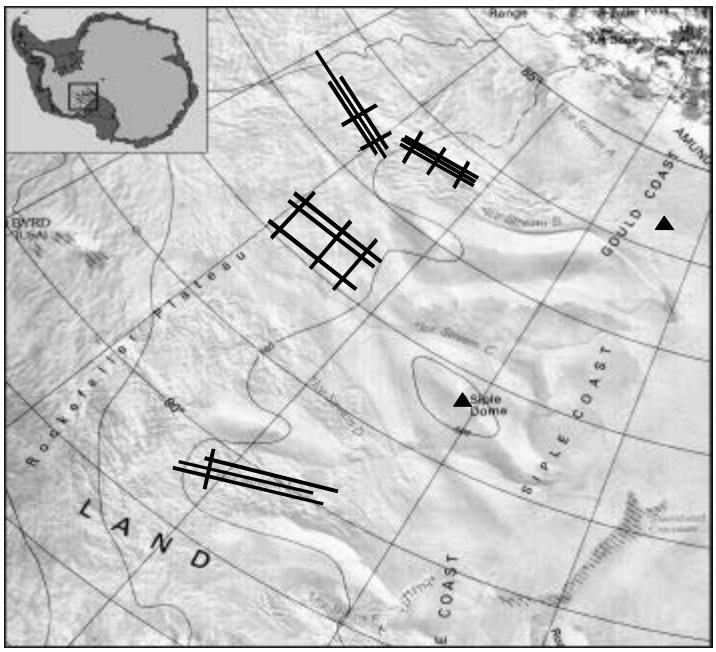

Fig. 9. Inset is a map of Antarctica with the location of the ice stream region enclosed in a black box. The large map is an enlargement of the ice stream region with laser survey lines (black grids). Base map is a mosaic of advanced very high resolution radiometer imagery (Mullins, 1999).

2.2.3. Description of the SOAR Laser Altimetry System

Equipment is mounted on a ski-equipped Twin Otter aircraft that is operated by the NSF-SOAR (National Science Foundation-Support Office for Aerogeophysical Research) facility. The geophysical systems on board include a gravimeter, magnetometer, a laser altimeter and an ice-penetrating radar. Positional information is provided by differential Global Positioning System (GPS), supplemented by Inertial Navigation System (INS), and precision pressure altimetry data. During most of the surveys performed by SOAR all sensors are collecting data allowing to map the ice sheet surface, the internal layering of the ice and the bedrock geometry and composition simultaneously. However, only the laser system, the ice-penetrating radar and auxiliary equipments were used during our laser altimetry missions. The altimetric measurements are made while the aircraft flies over a pre-determined flight path guided by real-time GPS.

2.2.3.1. Base Station Positioning

Two Ashtech dual frequency receivers located at different base camps are used as static base stations. The origin of each flight determines which base station is used. One of these base

stations is located on a very slow moving (0.34 m/a) portion of the ice-sheet known as Siple Dome (Fig. 9). A survey of this nearly static base station was performed on the first and last day of flying. Positions with an overall RMS of 0.02 m were acquired using the Automated GIPSY system developed by Jet Propulsion Laboratory. Ice motions at this site are small and uncomplicated, so time-linear interpolation is used to determine the position of the base station for the intermediate days. Another base station is located at the Down-B camp located near the middle of Ice Stream B (Fig. 9). The ice there moves at a rate of over 500 m/a. The position of the Down-B receiver relative to the Siple Dome receiver is computed using GPSurvey processing software (Trimble Inc.). A position is determined for each flight originating at Down-B. The calculated horizontal position of this station changes in a linear fashion as expected (Fig. 10.a). The calculated vertical position of the station changes in an irregular manner (Fig. 10.b). This magnitude of elevation change is not characteristic of an ice sheet over such short distances and is most likely an error in the GPS positioning due to the long baseline between receivers (280 km) and the horizontal movement of the Down-B receiver during each survey. The elevation of this base station is estimated to be the mean from five out of six surveys with an RMS of 0.065 m. The calculated position of the sixth survey is considered an outlier because it deviates from the mean by more than four times the reported RMS and is therefore not used (Fig. 10).

2.2.3.2. Aircraft Positioning

Once the base station position is established, the relative position of the Ashtech or TurboRogue receiver on the aircraft is calculated using GPSurvey. Shi and Cannon (1995) showed that the accuracy of GPS positioning on a moving aircraft can be at the 0.10 m level if tropospheric, ionospheric, precise satellite orbits (ephemerides), and multipath corrections are used during differential carrier phase post-processing (Shi and Cannon, 1995). GPSurvey software is used for processing and found to be reliable when used on a computer with a large amount of memory and a fast processor. For 11 out of twelve flights the maximum RMS reported by GPSurvey is 0.10 m. The 12^{th} flight was not used, because phase ambiguities were not resolved for a large portion of the flight.

To assess the performance of the GPSurvey processing, one survey was processed with GUITAR (GPS Inferred Trajectories for Aircrafts and Rockets, courtesy of John Sonntag, EG & G). The two solutions agree well, having a maximum difference of 1 cm in the horizontal and 8 cm in the vertical.

2.2.3.3. Laser Ranging

The Azimuth LRY 500 is a diode pumped Nd:YAG pulsed laser transceiver, operating in the near infrared domain (1064 nm). Pulsed lasers measure the travel time of a laser pulse from the

laser firing point to the surface and back to the receiver. To measure the time between the transmitted and the received pulses the Azimuth LRY 500 rangefinder uses 50% constant fraction discrimination. The timer starts at some consistent point on each transmitted pulse. Each timing event ends when the return pulse strength reaches half of its maximum amplitude. Thus the need of "range walk" correction is eliminated. The manufacturer reports a single pulse accuracy of 0.1m for distances up to 1.7 km. The ranger records at 500 Hz and 64 pulses are averaged to yield one range. The beam divergence was set for 4.5 mrad, producing a footprint with 1.5 meter diameter from the 300 m nominal flight height. This results in one average elevation for every 1.5 by 8 m area when the aircraft flies at 300-m terrain clearance.

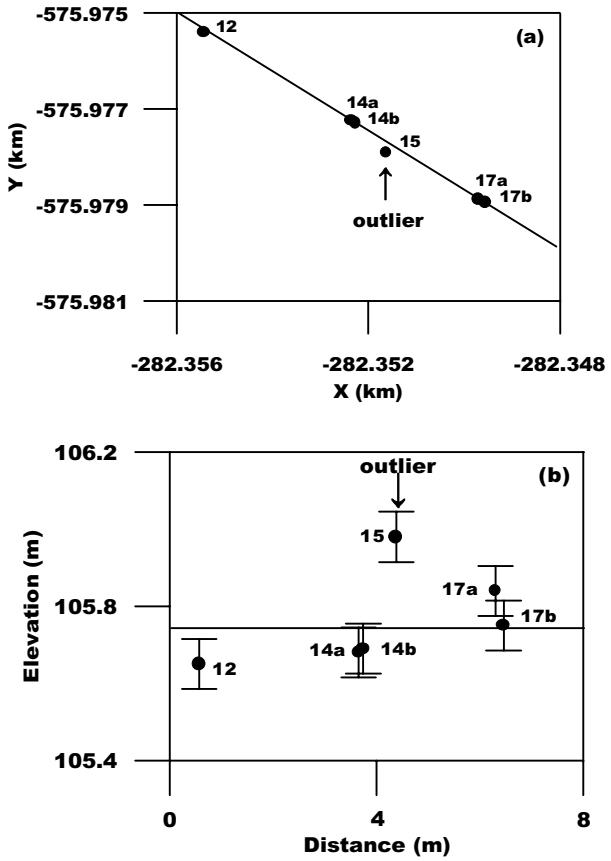

Fig. 10. (a) Measured changes in horizontal position of the Down-B receiver. (b) Elevation of each Down-B position plotted versus horizontal movement.
In panel (a) the points are labeled according to the day of the year that the survey took place. Two surveys, a and b, were conducted on days 14 and 17. Black line is a linear best fit through the data calculated without the point marked "outlier". The X and Y coordinates are polar stereographic. In panel (b) the black line is the mean elevation calculated without the point marked "outlier". Error bars are based on a 1-sigma RMS about the mean elevation.

2.2.3.4. Aircraft Attitude

The attitude of the aircraft, that is the heading, pitch, and roll angles determine the pointing direction of the laser. These angles are measured with a laser gyroscope that is part of the Litton

Aero Products LTN-92 INS unit. The INS has a quoted accuracy of 0.05° in all three angles (Vaughn and others1996), which translates to less than a 0.06 m error in calculated surface elevations when the aircraft is flying at less than 300 meters terrain clearance and the off-nadir pointing angles are less than 15°. These angles are not exceeded during survey missions, so the measured attitude contributes very little to the overall error budget.

2.2.3.5. System Timing

Each data collecting system operates independently and not in synchrony with the others. Universal Coordinated Time (UTC) is used as the standard to which all other times are corrected. The laser and INS measurements are tagged by a counter time that is corrected to UTC using information provided by the GPS time code generator. An additional correction is required for the individual attitude parameters, because the INS only records one angle at a time. The manufacturer specifies that these time lags are as follows: 110 ms in true heading, 60 ms in pitch and 50 ms in roll for the LTN-92 (Vaughn and others1996). It is possible to check whether these values are correct using pitch and roll maneuvers over a flat test field because timing offsets cause deformation of the measured surface when off-nadir angles are large. When performed, this test yielded slightly different time lags of 60 ms in roll and 85 ms in pitch. The measured time lags are preferred over the reported ones. The final step in correlating the data streams is to interpolate the INS and GPS data for the times when laser ranges have been recorded. Interpolation is necessary because the GPS data are recorded at 2 Hz, while laser measurements are recorded every at 500/64 Hz, and INS measurements at 8 Hz.

2.2.4. Computation of Laser Footprint

The laser range recorded during the flight is a slant range to the surface. To compute the position of the laser footprint in a global, geographic coordinate system, the laser range, aircraft position, and aircraft attitude are combined according to the scheme described in Lindenberger (1993), Vaughan and others (1996), and Ridgway and others (1997). Equation 1 sums up the procedure, which includes a series of coordinate transformations starting at a local reference system centered at the laser firing point (indicated subscript L) and ending in the WGS-84 Cartesian reference frame (indicated subscript W).

$$\vec{p}_W^{LPF}(X,Y,Z) = \vec{p}_W^{GPS} + d\vec{p}_W^{GPS} + R_z(-lon^{GPS}) \cdot R_y\left(lat^{GPS} + \frac{\pi}{2}\right) R(r,p,h) \cdot$$
$$R(\Delta r, \Delta p, \Delta h)\left(\begin{bmatrix} x_A^{GPS.LFP} \\ y_A^{GPS.LFP} \\ z_A^{GPS.LFP} \end{bmatrix} + R(dp,dr,0) \cdot \begin{bmatrix} 0 \\ 0 \\ r_L^{LFP,S} + \Delta r_{atm} + \Delta r_{bias} \end{bmatrix}\right) \qquad [18]$$

The notations in equation (18) are explained in the next setions. Rotations are indicated by R (x, y, or z) subscripts indicate a rotation about a specific axis.

2.2.4.1. Range measurement corrections

The laser ranger is mounted inside the aircraft pointing towards nadir. The ranger measures the distance $\left(r_L^{LFP,S}\right)$ between the Laser Firing Point (LFP) and the snow surface (S) from points along the flight trajectory. The measured laser range is corrected for atmospheric delay and a range bias:

- **The atmospheric correction ($?\,r_{atm}$)** accounts for the reduced speed of light and refraction in the atmosphere. It reduces the measured range by approximately 2 cm for every 100 m of altitude. The computation of this correction is taken from Vaughn et al. (1996), Ridgway et al. (1997), and Marini and Murray (1973). Pressure, temperature and water vapor are extrapolated at the aircraft location from data collected by automatic weather stations at Siple Dome and on Ice Stream C. The meteorological data are collected and distributed courtesy of John Stearns of the Automatic Weather Station Project (Stearns, via internet)

- A **range bias ($?\,r_{bias}$)** of 0.35 m is added to each range measurement. This bias is determined by comparing surface elevations derived using laser altimetry to elevations derived using precise surveying methods on the ground (see details in Section 2.6). The bias is most likely due to a constant lag in the timing of the laser pulse, although this has yet to be proven and is currently being investigated.

2.2.4.2. Transformation from local laser reference system to local Earth tangent reference system

The corrected laser range vector $[0,0,r_L^{LFP,S} + \Delta r_{atm} + \Delta r_{bias}]^{-1}$ is transformed into a local aircraft reference system (indicated subscript A) centered at the GPS antenna. The aircraft reference system is defined using several symmetrical 'hard' points on the aircraft (joists, flap indicators, and seats) whose positions are measured using a theodolite. One axis runs the length of the aircraft between symmetric points. A second axis is perpendicular to the first axis and is aligned with the aircraft wings. The third axis is vertical and perpendicular to the other two. This transformation is carried out by rotating the laser range vector by the laser mounting bias *R(dp,dr,0)* (see Section 5.2). The offset vector between the laser firing point and the GPS antenna $\left([x_A^{GPS,LFP}, y_A^{GPS,LFP}, z_A^{GPS,LFP}]^{-1}\right)$ is then added. The measured offset of [-1.378, 0.411, 1.566] is found using a theodolite and tape measure. The next rotation uses the INS mounting biases $R(\Delta r, \Delta p, \Delta h)$ to transform the laser vector from the local aircraft reference system into the local INS reference frame with axes defined by the roll, pitch, and heading axes of the INS. The INS mounting biases account for the angular differences between the aircraft body system and the roll, pitch and yaw axes. This step also accounts for the difference between local vertical and the direction perpendicular to the geodetic ellipsoid (WGS-84). SOAR reports a -0.30 degree

bias in both pitch and roll. Because these angles are small, the SOAR values are simply added to the attitude angles reported by the INS. The last rotation of this series transforms the laser vector from the INS reference from to the local-level reference frame using the attitude of the aircraft $R(r,p,h)$. The local-level reference frame is an Earth-tangential reference system centered at the GPS antenna. The z-axis is perpendicular to the WGS-84 ellipsoid and points downward. The x-axis lies along the intersection of the local GPS meridian and a plane parallel with the tangent plane to the ellipsoid (i.e., points north). The y-axis completes the right hand system.

2.2.4.3. Transformation from local-level reference system to WGS-84 Cartesian system

The laser vector from the GPS antenna to the laser spot on the snow surface is transformed into the WGS-84 global Cartesian system. Rotations for the latitude, $R_y(lat^{GPS} + \frac{\pi}{2})$, and longitude, $R_z(-lon^{GPS})$, of the aircraft are performed to align the local-level reference frame axes with the WGS-84 axes. The final position of the laser footprint is computed by adding the laser vector to the vector recorded by the GPS on board the aircraft. Because the GPS position has uncertainties, some authors (e.g., Lindenberger) use an adjustable parameter ($d\vec{p}_W^{GPS}$) to remove any GPS bias. Lindenberger (1993) calculated this parameter by surveying a rough but stable surface before and after each flight. Ice sheet surfaces are too flat and not stable enough for this kind of calibration. Other researchers use an adjustment scheme based on the analysis of large set of cross-overs to remove any GPS bias. Our data set does not have enough flights and cross-overs to take advantage of this method either. For these reasons, $d\vec{p}_W^{GPS} = \vec{0}$ is assumed to be zero for this study. After applying simplifications Equation 18 becomes:

$$\vec{p}_W^{LPF}(X,Y,Z) = \vec{p}_W^{GPS} + R_z(-lon^{GPS}) \cdot R_y\left(lat^{GPS} + \frac{\pi}{2}\right) \cdot R(r+\Delta r, p+\Delta p, h+\Delta h)\left(\begin{bmatrix} x_A^{GPS.LFP} \\ y_A^{GPS.LFP} \\ z_A^{GPS.LFP} \end{bmatrix} + R(dp,dr,0) \cdot \begin{bmatrix} 0 \\ 0 \\ r_L^{LFP,S} + \Delta r_{atm} + \Delta r_{bias} \end{bmatrix}\right) \quad [19]$$

2.2.5. Calibration and Validation

2.2.5.1. Laser range calibration

Two skiways next to the Siple Dome base camp were surveyed using both snowmobile-mounted GPS and laser altimetry in mid-December, 1997 (Fig. 11-13).

The snowmobile (also referred to as skidoo) surveys are used to produce a reliable surface profile for comparison with laser derived elevations. A +0.35 m bias was found for the elevation derived from the laser altimetry. This bias is due to a systematic timing error in laser ranging

and is added to every laser range during processing. To determine this bias the data are converted into a local, Earth-tangential reference system where the x-axis points to true North, z-axis points toward the center of the Earth, and the y-axis completes a right-hand system. The position of the GPS base station antenna mounted on the SOAR tent was selected as the origin $\left(p_W^{calsite}(X,Y,Z)\right)$. Equation 20 describes the transformation and Fig. 11-13 show how the reference system is used.

$$\vec{p}_{loc}^{\,LFP}(x_{loc},y_{loc},z_{loc}) = R_y(-lat^{calsiteO} - \pi/2)\cdot R_z(lon^{calsiteO})\cdot (\vec{p}_W^{\,LFP}(X,Y,Z) - p_W^{calsiteO}(X,Y,Z)) \quad [20]$$

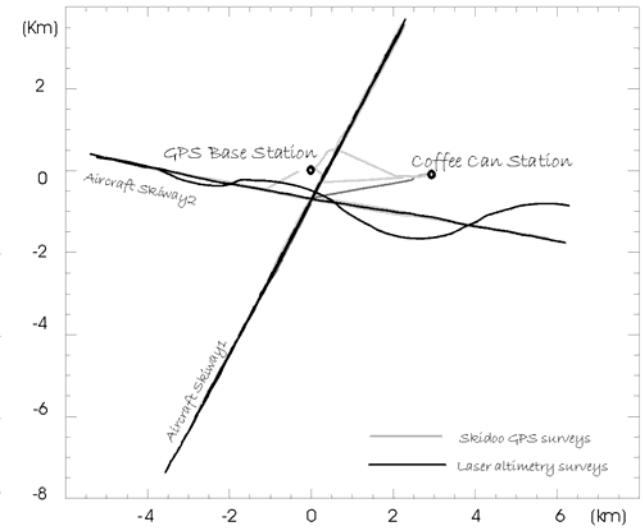

Fig. 11. Laser altimetry calibration surveys at Siple Dome, West Antarctica.

2.2.5.2. Laser mounting biases

Due to mounting errors, the laser is not perfectly aligned with the aircraft's roll and pitch axes, as defined by the INS. The laser mounting bias is defined as the angular difference between the aircraft body and the laser axes. The estimated laser mounting bias is -1.2 degrees in pitch and -0.3 degrees in roll during the 1997/98 field season (SOAR field notes). Pitch and roll maneuvers over a relatively flat test field are used to check these values. The deformed surface shown in Fig. 12 is the result of a laser survey where no mounting bias corrections were used. By changing dr and dp to minimize the surface deformation the mounting bias can be estimated. In this case the initial estimate of -1.2 degree in pitch and - 0.3 degree in roll was first confirmed by using a simple grid search.

2.2.5.3. Calibration of Laser Systems using a Least Square Solution

To obtain the 'best' estimates of the calibration parameters we developed a new calibration method. This analytical method combines the model of data acquisition system with a locally

linear representation of the topographic surface and minimizes of the difference between a precisely mapped reference surface and the surface derived from the altimetry. The calibration problem formulated as an extended Gauss-Markov model and it is solved with an iterative scheme. We have applied our novel solutions for recovering the angular and range bias of the SOAR system and to simulate calibration scenarios for the ICESat mission (Filin and Csathó, 1999 and 2002; Filin and others, 2001).

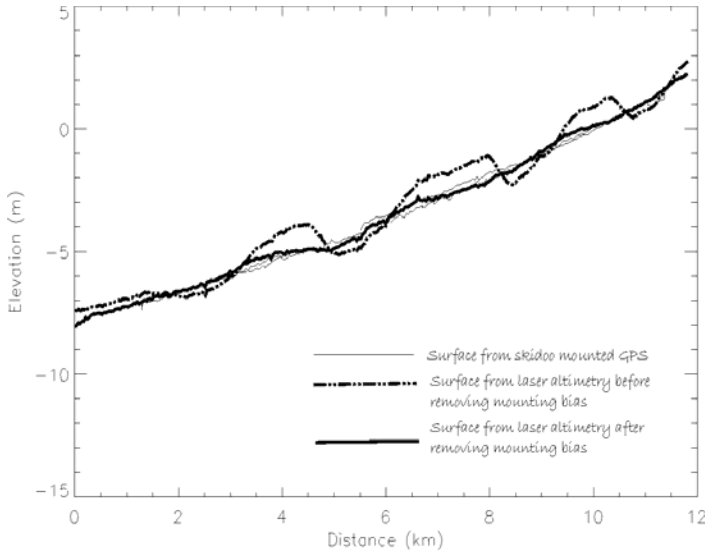

Fig. 12. Comparison of measured elevations along Skiway 2 surveyed with snowmobile-mounted GPS and laser altimetry.
The two laser profiles are derived from the same survey before and after the removal of the laser mounting bias. The magnitude of the pitch maneuvers are about 8 degrees off nadir.

2.2.5.4. System Accuracy

After correction of range and angular biases the SOAR system performed well over short distances. Repeat flights over Skiway1 show a 2.8 cm bias with an overall RMS of 10.3 cm (Fig. 13). The bias is attributed to surface slope, because the repeat flight lines were approximately 25 m apart. The RMS difference is measurement of surface roughness caused by sastrugi. Sub-decimeter accuracy was also found when laser derived elevations were compared to elevations measured with the snowmobile surveys.

2.2.6. Repeatability and Accuracy

2.2.6.1. Crossing flight lines

Laser surveys that cross nearly perpendicular to one another are evaluated to determine the repeatability of the procedure over long baselines. Crosses are evaluated by finding laser measurements within a 10 m radius of the cross-over point. The average elevation difference of crosses on Ice Stream C are shown in Table 1. Table 1 also shows how crosses compare if both

laser surveys were conducted during the same or independent GPS surveys. The agreement is better for crosses measured during the same flight.

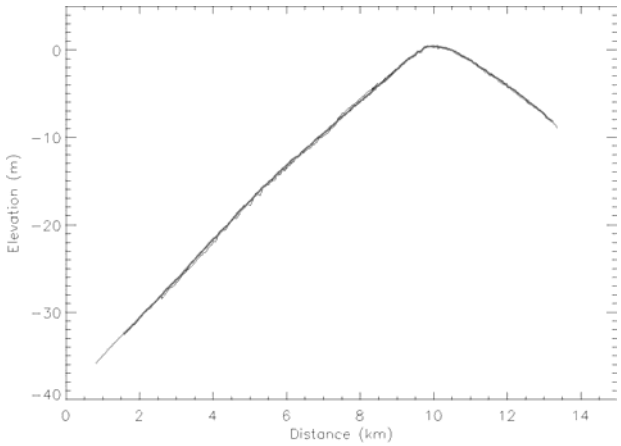

Fig. 13. Surface derived from repeat laser altimetry (grey lines) and snowmobile-mounted GPS (thin black lines) along Skiway1.

Elevations produced from Ice Stream C survey flight number 26 were found to have large biases of up to 84 cm. This large bias is 8 times greater than the reported GPS RMS for that flight, which suggests that the phase ambiguities were not resolved throughout the entire flight. Poor GPS initialization practices (i.e. the aircraft started and ended at different base camps over 280 km apart) are the most likely source of the problem. The end result is that the flight is of limited use for change detection on a two year time-scale, and topographic maps made with this flight could have an error of nearly a meter. Average elevation differences are given for Ice Stream C with and without this flight (Table 1).

2.2.6.2. Coffee-can comparisons

Laser surveys go near distant coffee can stations providing a means for evaluating accuracy over long baselines (Fig. 13). The coffee-can markers are surveyed using precision GPS methods and are used to study ice sheet mass balance (Hamilton and others, 1998). GIPSY is used to determine marker positions with a vertical error of less than 0.01 m. The laser flights missed the coffee can site on Ice Stream C by 840 m, therefore linear interpolation is used to estimate laser elevations at the coffee can site. Results showed that laser elevations agreed to within 0.10 m of the coffee can elevation.

Surveys Considered	Number of Crosses	Number of Laser Measurements	Mean Elevation Difference Between Surveys
All surveys	8	34	0.36 m
w/o 26:	4	16	0.25 m*
From same GPS survey	2	8	0.18 m*
From independent GPS surveys	2	8	0.32 m*

* Values do not include measurements from survey flight 26.

Table 1. Cross-over comparisons for Ice Stream C

2.2.6.3. Topographic Maps

Large portions of ice streams B1, B2, C, and E have been surveyed. Topographic maps have been made for all four ice streams with varying uncertainties. An example is shown in Fig. 10 for Ice Stream C. Ice surface contours compare very well with an earlier radar study (Retzlaff and others, 1993), although the older maps have uncertainties that are too large to be useful for detection of changes in surface elevation. The laser derived surface map is superimposed over bed elevations taken from radar measurements (Fig. 14) to illustrate how bed features affect the ice in terms of velocity vectors, surface elevations, and slope.

2.2.7. Glaciological Interpretation

Ice Stream C was chosen to investigate rapid ice thickness change because the downstream portion is nearly stagnant while the upstream portion is still active (Fig. 14). Within the laser grid, the ice velocities changes from 25 m/a to 3 m/a (Whillans and Van der Veen, 1993 and Joughin and others1999). As more ice moves into the region, ice thicknesses are expected to increase by 0.50-1.0 m/a (Whillans and Van der Veen, 1993 and Joughin and others, 1999). Fig. 14 also shows that surface slopes are greater in the zone where velocity decreases the quickest. This is an impossible scenario for steady-state conditions and could be evidence that Ice Stream C is being reactivated. It seems sensible that a build-up of ice will cause the ice to begin streaming again.

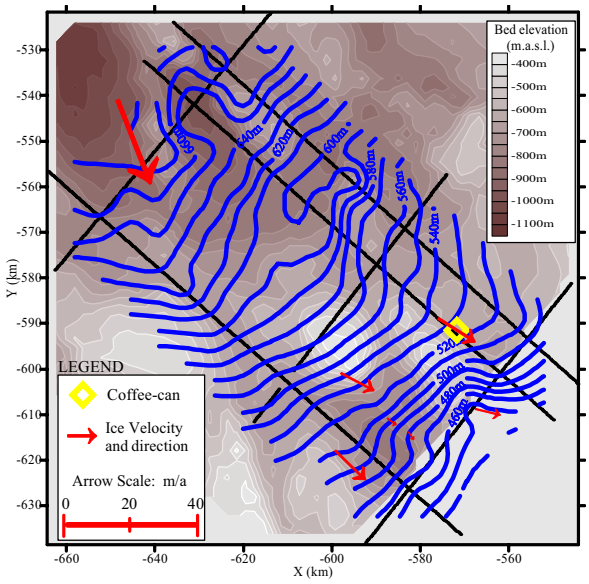

Fig. 14. Laser derived elevation contours (blue) of Ice Stream C superimposed over bed elevations from airborne radar surveys (Retzlaff and others, 1993).
Red arrows show ice flow direction and magnitude (from Whillans and van der Veen, 1993, and Hamilton, pers. comm.). The yellow diamond marks a coffee-can validation site. Dashed black lines are the tracks of the laser surveys.

The pattern of ice thickness, ice velocity, and surface slope observed on Ice Stream C are unlike what is normally expected. Ice thickness decreases by a factor of two from the upstream portion of the grid to the downstream portion mostly as a result of increased bed elevations. The velocity decreases by a factor of four for the same region and the surface slope increases by a factor of 2. In an ordinary glacial setting, the velocity would increase with increased surface slope and decreased thickness. The ice seems to be piling up as it reaches the bedrock ridges. This could be due to a lack of subglacial water at the downstream end. If the upstream portion of the ice stream is sliding over clay-rich sedimentary rocks, basal friction would be very small for two reasons. First, ice thicknesses are great enough in this region to induce pressure melting despite cold temperatures. Second, clay rich materials have very low permeabilities so water is not able to escape. This scenario has been shown to exist beneath other fast flowing ice streams (Anandakrishnan and Bentley, 1993; Engelhardt and others, 1990). As for the downstream portion of Ice Stream C, Anandakrishnan and Bentley (1993) found basal seismic noises that were not sensed beneath fast flowing ice streams. The interpretation was that Ice Stream C must have experienced a dewatering and loss of dilatency in the lubricating till layer. Without well-distributed water the ice can become frozen to the bed, forming 'sticky' spots, or in this case an entire 'sticky' region. The future course of the growing bulge will determine the behavior of ice stream C and will illustrate the effect of glaciological processes, presumably the advancement of a lubricated bed. One can expect a major change of the studied region as this thickening continues.

2.2.8. Computation of thickness changes

To map thickness changes the laser altimetry surveys were repeated in the 1999/2000 austral summer. First surface elevation changes for computed from neighboring repeat points. Then corrections for change accumulation rate changes, vertical motion of the bedrock and snow compaction were applied to convert the elevation change into thickness change. Details of the procedure and results are presented in Spikes and others, 1999 and Spikes and others, in press.

2.2.9. Conclusions

Ice sheet mass balance was estimated by measuring surface elevation changes over time. The main objective was to assess the accuracy and precision of the laser altimeter system of the Support Office of Aerogeophysical Research (SOAR) facility, and to evaluate its performance for measuring high precision ice sheet surface topography and ice thickness changes. I have developed a suite of data processing and calibration software to compute precise ice sheet elevation from the measured GPS and INS data and laser ranges. Aircraft positions were obtained with an accuracy of 0.1-0.2 m by differential carrier phase processing. Instrument biases were determined by laboratory, ground and in-flight calibrations. A new calibration algorithm, facilitating calibration over arbitrary, natural surfaces, was developed to determine the mounting biases of the laser system. The accuracy of the system was checked by flying over areas mapped by snowmobile mounted GPS, over permanent markers anchored deeply in the ice sheet (‘coffee cans’) and by comparing elevations where different flights are crossing each other.

We conducted repeat laser altimetry surveys on several sites of glaciological interest on the West Antarctic Ice Sheet. The mapped trend of surface changes agrees well with previous observations, but localized, complex pattern of thickening/thinning was detected both on the Whillans Ice Stream and on Ice Stream C. We will continue to monitor these sites using ICESat satellite laser altimetry data. As a part of our NASA funded project we will combine remote sensing, laser altimetry and bedrock elevation data to describe the relationship between surface elevation changes and ice dynamics.

2.3. Summary

In this chapter I presented some of my contributions to the ICESat mission and results from the first precise, repeat airborne laser mapping in Antarctica. As part of the ICESat team my duties included to summarize the physical basis of the laser waveform processing for inclusion in the ICESat Waveform Algorithm Theoretical Basis Document (ATBD, Brenner and others, 1999), and to develop and validat waveform processing algorithms for sea ice and ocean mapping (Csathó and Thomas 1995 and 1996; Filin and Csathó, 2000b). I also participated in the development of new calibration algorithms for spaceborne altimeters (Filin and Csathó, 1999;

Filin and others, 2001) and I am responsible for ICESat calibration and validation at the Dry Valley site, Antarctica (Csathó and others, in press).

The goal of the second investigation described in this chapter was to improve the accuracy of the SOAR laser system and to perform repeat surveys to measure the mass balance of selected site in West Antarctica. I developed the prototype software in IDL programming language to compute the laser point position from the different raw data streams, directed the processing of the kinematic GPS data for positioning and designed and supervised the field data acquisition and calibration-validation experiments. We have also developed new calibration and validation algorithms (Filin and Csathó, 2002). Finally, using the novel approach and tools developed in this study we could perform first accurate, repeat airborne surveys in the Antarctica (Spikes and others, 1999; Spikes and others, in press).

Since 1994 I have been investigating a wide range of other research topics in laser altimetry. These topics included topographic mapping in Greenland (Csathó and others, 1995, 1996a, 1996b), detailed analysis of the error models of airborne laser methods (Schenk and Csathó, 2001) and the application of laser mapping in urban environment (e.g., Csathó and others, 2001c; Schenk and others, 2001). These topics are not presented in the dissertation, and the interested reader is referred to the original publications.

My results related to the development of laser mapping methods are summarized in Section II of the thesis booklet.

3.0 APPLICATION OF REMOTE SENSING FOR MAPPING ICE SURFACE CHANGES FROM SINCE THE LITTLE ICE AGE -- TRIMLINE MAPPING FROM MULTI-SPECTRAL LANDSAT TM IMAGERY

3.1. Introduction

Constructing longer glacier histories, spanning the last few hundred years or so, is of particular interest for outlet glaciers draining the interior of the Greenland Ice Sheet. Repeat surveys by airborne laser altimetry in the 1990s have revealed significant thinning of the ice sheet at lower elevations (Krabill and others, 2000). Specifically, some of the larger outlet glaciers are thinning at rates of several meters per year, with the most extreme thinning observed near the terminus of Kangerlussuaq Glacier in southeastern Greenland, where rates as high as 10 m/yr were measured (Abdalati and others, 2001). Such large thinning rates cannot be explained by a recent increase in ablation or decrease in snowfall and, instead, point to ice-dynamical processes as drivers of glacier retreat (Van der Veen, 2001). To fully appreciate the significance of these recent glacier changes, the magnitude of retreat and surface lowering must be placed within the broader context of retreat since the Last Glacial Maximum (LGM) and, more significantly, retreat following the temporary glacier advance during the Little Ice Age (LIA). The instrumental record of glacier observations in Greenland dates back to aerial photography conducted by the Danes in the 1930s and 1940s. Glacier histories extending farther back in time must be based on geological information retrieved from formerly glaciated regions. Depending on the age of mapped glacial-geological features, histories may be extended to the LIA and possibly as far back as the LGM, some 18,000 years BP.

The traditional approach to reconstructing paleo ice sheets from geomorphological and geological information has been to map such features during detailed field investigations. Clark (1997) noted several barriers inherent to this approach that impede synthesizing such fragmentary information into a coherent ice-sheet wide picture. In most cases there are few links between spatially separate studies, or there may be large gaps void of observations. Moreover, in many instances, control on dating is rather poor, thus casting doubt on the commonly-made assumption that similar features reported in different studies are synchronous. These difficulties can be partially overcome through the use of remote sensing, which allows for greater spatial coverage of geological features (Clark, 1997). As he has noted,

> a major problem in validating ice sheet models is that geologically-based information has been derived mostly from fieldwork and usually relates to only small sectors of ice sheets which can be thought of as point evidence. Furthermore there are frequently unresolved contradictions between local areas. A methodology that attempts to provide information on wider spatial scales and

> promote greater analysis and coherence of all evidence is by use of remote sensing and … GIS.

Early geological applications of remote sensing were based on high-resolution aerial photogrammetry. According to Clark (1997), the study of Sugden (1978) was the first to demonstrate the usefulness of satellite images to provide glacial-geomorphological information over large areas. In that study, a Landsat MSS photomosaic was used to produce a proxy map of the intensity of glacial erosion by the Laurentide Ice Sheet. Subsequent applications have included mapping of depositional landforms (e.g. Punkari, 1982), identification and mapping of previously unrecognized mega-lineaments (e.g. Clark, 1993; Clark and others, 2000), and mapping margins of paleo ice streams (Stokes and Clark, 2002). A review of earlier work is provided by Clark (1997). The objective of the present study is to explore the feasibility of using multi-spectral Landsat TM images to map trimlines in the coastal regions of Greenland.

In mountainous regions, former higher stands of glaciers that retreated recently (e.g. since the Little Ice Age maximum) are frequently marked by trimlines on the walls of valleys and fjords previously occupied by these glaciers (Fig. 15). Erosional action of the moving ice causes vegetation to be removed where the ice is in contact with the surrounding rock walls. The upper limit of this eroded region, which becomes exposed as the glacier retreats and its surface is lowered, is called the trimline (Flint, 1971, p. 144). Mapping of trimlines and other glacio-geomorphological features thus allows reconstruction of the Neoglacial history of glaciers.

Fig. 15. Trimline zone on steep slopes, north of Sermeq avangnardleq

Historical evidence indicates that in many parts of the Greenland Ice Sheet the major historical maximum occurred almost simultaneously during the last decades of the 19th century (Weidick, 1984). Therefore, mapping of the trimline zone over larger areas and possibly the

entire ice sheet, could provide an estimate of the total area deglaciated as well as the total ice volume lost since then. Indeed, based on comparison between trimline elevations and the current ice-surface elevation in west Greenland, Weidick (1968) estimated an average loss of 200 km^3/year ice from the whole Greenland Ice Sheet since the Little Ice Age, corresponding to an average rise of 0.6 mm/year in global sea level. This is equivalent to a 15,600 km^3 total loss or 48 mm global sea level rise since ~1850 A.D.

The ability to map surficial features from satellite imagery depends on obtaining spectral signatures of these features that are markedly different from the signatures of surrounding regions. With respect to trimlines, spectral reflectance differences may be associated with variations in vegetative cover above and below the trimline. The LIA trimlines are usually characterized by sharp vegetation boundaries. Outside the trimzone, the flat and gentle slopes are often covered by tundra vegetation, while steeper rock surfaces are lichen covered. Inside the trimline region, rock surfaces are fresh and bare, retaining their original color and spectral properties (Knight and others, 1987). It is well known that vegetation can easily be mapped using visible and near infrared (NIR) spectral imagery. Several studies have demonstrated the pronounced effect of lichens on the reflectance spectrum of the land surface (Ager and Milton, 1987; Rivard and Arvidson, 1992; Satterwhite and others, 1985). Thus, spectral property information from multi-spectral satellite images can be used to locate the boundary between lichen-covered and lichen-free surfaces. This boundary is the trimline.

Lichens are "an association of a fungus and a photosynthetic symbiont resulting in a stable thallus of specific structure" (Hawksworth and Hill, 1984). Lichens occur in most habitats around the world and communities are usually classified according to their substrate. Worldwide, approximately 13,500 taxa of lichenized fungi are recognized (Hawksworth and Hill, 1984). Lichens, which do not have special organs or structures for water storage, shut down metabolically when dry, allowing them to withstand longer periods of dryness. Because of this opportunistic usage of available moisture, lichens can survive in environments that are low or deficient in moisture available for the support of plant life. In these so-called xeric environments, lichens spend much of the time in a dry, inactive state (Lawrey, 1984).

Rock substrates provide stable habitats for the establishment of long-term lichen communities. On these surfaces, lichens grow at relatively uniform rates of time scales of centuries or millenia. Once attached to a substrate, lichens do not move during their lifespan and thus the age of a lichen can be considered a proxy for the minimum exposure time of the substrate to the atmosphere and sunlight. These two characteristics form the basis for lichenometry, a biological technique for estimating the age of exposed and stabilized rock surfaces (Locke and others, 1979). In short, the assumption is made that the size of the largest individual thallus on a substrate is a function of the time the substrate has been exposed. Using surfaces of known exposure age, a lichenometric dating curve can be established that relates

surface exposure age to the largest lichen size. This dating curve is then applied to estimate the exposure age of other surfaces based on the largest size of lichens found on these surfaces (c.f. Noller and Locke, 2000). Lichenometry has been applied in glacial geology and geomorphology at many sites around the world including dating the LIA maximum in Iceland (e.g. Kirkbridge and Dugmore, 2001), in South America (Winchester and Harrison, 2000) and in Alaska (Haworth and others1996). Beschel, who is regarded as the "Father of lichenometry", has pioneered lichenometric dating in west Greenland (Beschel, 1961). While the study presented here focused on determining the spatial extent of lichen-covered rocks, exploratory lichenometry was conducted and a tentative dating curve for dating glacio-geomorphological features exposed since the LIA was derived. Results of that part of our study will be discussed elsewhere.

3.2. Spectral characteristics of lichens

As noted by Ager and Milton (1987) more than 15 years ago, very little research has been done to investigate spectral reflectance characteristics of lichen, or how lichen cover affects the spectral reflectance of rock substrates. Since that study, it appears that little further work on this topic has been undertaken. Early studies on the reflectance of lichens (Gates and others, 1965, 1966; Hoffman, 1970) failed to note differences between spectral properties of lichen and those of vascular plant leaves, which may explain why no further studies were conducted on lichen until the 1980s. In the context of heat resistance and the energy budget of different Scandinavian plants, Gauslaa (1984) measured the reflectance in 24 lichen species at wavelengths ranging from the visible (400 – 700 nm) to the near infrared (700 – 1400 nm). As in earlier studies, however, no obvious differences between lichen and various alpine vascular plants were found that could be used to differentiate lichen cover from other vegetation. Some of these earlier studies (e.g., Gates and others, 1965) were restricted to the visible and to the lower part of the near infrared region (wavelength < 1100 nm) and therefore failed to identify clear spectral signatures of lichen that becomes more pronounced at greater wavelengths. Occasionally a lichen species, such as *Parmelia conspersa* (Hoffman, 1970, fig. 6), will exhibit spectral properties quite similar to that of typical plants throughout the whole 400-2500 nm spectral range. *Parmelia conspersa* is a common lichen in both the eastern and western United States occurring in large loose patches on rock surfaces.

More relevant to the present investigation is the study of Satterwhite and others (1985) who examined the effect of lichen cover on the reflectance spectrum of granite rock surfaces. Samples of bare granitic rocks and of lichens found on these rocks were collected from the East Pioneer Mountains, near Melrose, MT. These samples were subjected to spectral measurements in the laboratory using a spectroradiometer covering the 400 – 1100 nm range in 10 nm increments. The findings of this study were somewhat ambiguous with the authors concluding that (1) the reflectance spectra of lichen-covered rocks can be significantly different from that of

bare rock and, (2) that lichens can increase, decrease, or have no effect on the spectral reflectance of rock substrates, depending on the spectral contrast between the lichens and the bare substrate. These somewhat inconclusive results may have been the consequence of the limited spectral range considered by Satterwhite and others (1985), as the spectral signatures of lichens appear more distinct at greater wavelengths. Ager and Milton (1987) collected rock and lichen samples from the Extremadura region in west-central Spain, and made spectral reflectance measurements in the laboratory with readings at 1 nm intervals from 400 to 800 nm, and at 4 nm intervals from 800 to 2500 nm. For smaller wavelengths (400 – 700 nm), comparison of three lichen groups showed differences in spectral properties associated primarily with pigmentation (i.e. lichen color). Over the 700 – 1350 nm region, reflectance increases steadily and remains high at greater wavelengths. This is distinctly different from the reflectance curve of green, leafy, plants, which tends to rise almost vertically from the visible to the near-infrared and decreases slowly from 800 to 1300 nm (Ager and Milton, 1987, fig. 2).

To evaluate the effect of lichen cover on rock spectra, Ager and Milton (1987) applied a linear mixing model to compute the spectra of partially lichen covered rock surfaces. Linear mixing assumes that the incident energy is scattered only once (from the surface to the sensor) and does not undergo multiple scattering, for example, among foliage components or between the vegetation canopy and soil surface. In short, this technique involves computer averaging of the spectrum for each rock type considered and the spectrum derived from a combination of all the lichens found on that rock type. Mixed spectral curves were obtained for lichen cover ranging from 0% (bare rock) to 100% (no rock visible) on different rocks such as slate, hornfels, and granite substrates. The spectrum of slate and hornfels is comparatively flat at wavelengths greater than 800 nm with a more or less uniform spectral reflectance of less than 25% (slate) and 30% (hornfels). Because of the greater overall reflectance of lichens throughout the near infrared, lichen cover increases the reflectance of these rock types. Granite on the other hand, is more reflective than lichens over the entire spectral range considered (except for strong absorption bands at 1400 nm and 2200 nm) and lichen cover reduces the reflectance of a granite substrate.

Whereas the studies referred to above involved laboratory measurements on field-collected samples, Rivard and Arvidson (1992) conducted field observations for different surfaces on the island of Qilangarssuit, about 30 km south of Nuuk on the west coast of Greenland. The objective of that study was to investigate whether Landsat Thematic Mapper (Landsat TM) multispectral imagery can be used for lithologic mapping in Arctic regions. These authors concluded that, while Landsat TM data can be used as first order products to distinguish between tundra vegetation that typically covers older moraines at lower elevations, and lichen-covered bedrock exposed at higher elevations. Mapping of different lithologic rock facies with Landsat TM imagery is severely hampered by the limited spectral and radiometric capabilities of the

sensor as well as by the ubiquitous lichen cover. For the purpose of mapping trimlines, however, requirements are less stringent and the results of Rivard and Arvidson (1992) are encouraging as these indicate the possibility of distinguishing between tundra cover, lichen-covered rocks, and bare rock surfaces.

Field measurements were carried out by Rivard and Arvidson (1992) over the range 450 to 2400 nm with band spacing ranging from 9 nm at 450 nm to 40 nm at 1300 nm. The sensor of the spectrometer was placed ~1 m above the surface, giving a field of view of ~5 cm^2 at an observation angle of a few degrees. Raw spectral data were smoothed using a five-band arithmetic moving average and converted to reflectance by dividing with the measured signal of a reference surface. Typical reflectance spectra for the most common surface types in the region studied by Rivard and Arvidson (1992) are shown in Fig. 16.

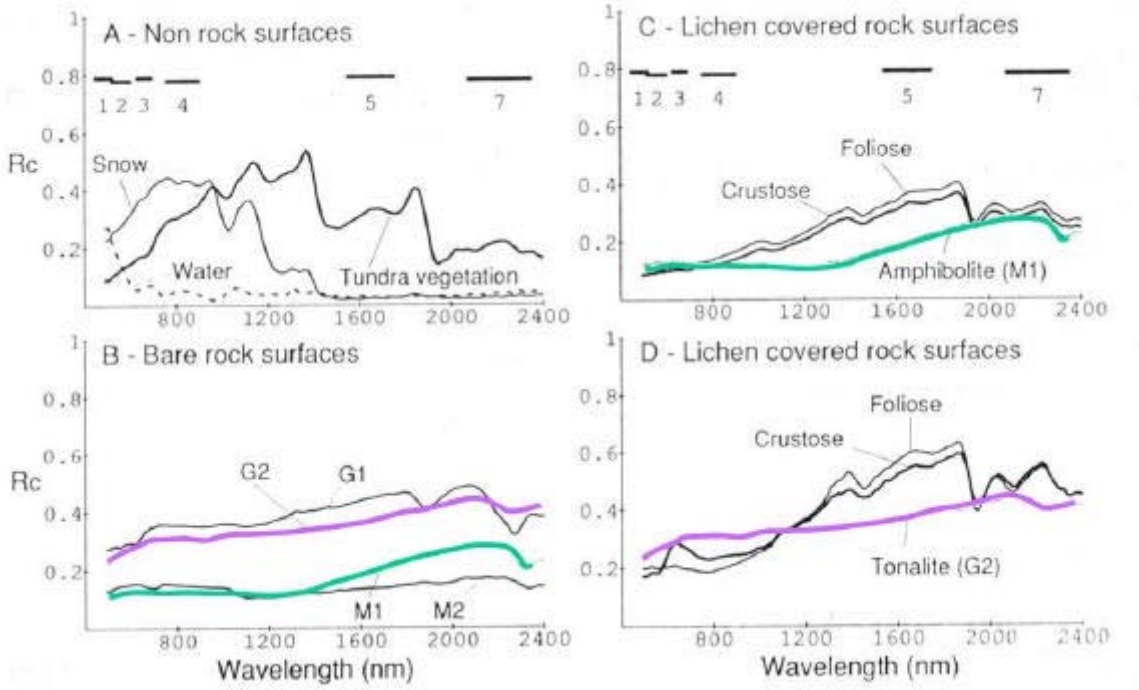

Fig. 16. Radiance coefficient spectra acquired in the field for snow, water, and tundra vegetation (A), bare rocks (B), and lichen covered rock surfaces (C, D) from Rivard and Arvidson, 1992.
M1 and M2 are amphibolites, G1 is granodiorite and G2 is coarse-grained tonalite. Band positions of the Landsat TM and ETM+ sensors are shown on the top graphs.

A full discussion of these curves is given in Rivard and Arvidson (1992), but for the present investigation, most significant is the effect of lichen cover on rock substrates. At intermediate wavelengths, ~1200 – 2000 nm, the reflectance is significantly increased by lichen cover compared to bare rock. Again, the reason for this is that the rock substrates considered by Rivard and Arvidson (1992) have lower spectral reflectance than do lichens. Amphibolite consists mainly of the mineral hornblende which is usually dark green to black in color. In external appearance, tonalites are similar to granites but usually darker in color. Thus, these

field observations confirm the most important features of the computer-generated mixed spectra predicted by Ager and Milton (1987).

3.3. Previous trimline studies

It has long been recognized that trimlines can be mapped using aerial photography. For example, Hughes (1998, fig. 1.5) showed glacial erosion trimlines along the margins of Jakobshavn Isbræ, west Greenland, mapped photogrammetrically by Prescott (1995) from an aerial photomosaic of the region. However, as noted by Clark (1997), aerial photographs, while capable of providing excellent high-resolution information on geomorphological features, typically cover limited areas and extending this procedure to cover regions formerly occupied by entire ice sheets is a daunting task. Because of the greater area captured by a single image (typically 60 by 60 km or more), satellite imagery permits greater areas to be studied efficiently. To our knowledge, the study of Knight and others (1987) is thus far the only study to use satellite images to map trimlines and ice-sheet retreat.

Landsat Multispectral Scanner (MSS) imagery, acquired in July, 1982, was used by Knight and others (1987) to identify recently deglaciated regions bordering the present-day ice sheet margin. In the MSS-5 band (red, 600-700 nm), a light-tinged zone fringing the ice sheet and extending down both flanks of Jakobshavns fjord was noted. The outer limit of this zone appeared to be marked by a sharp boundary in vegetation cover. Using all four MSS bands, Knight and others (1987) distinguished six different classes of surface types, namely sediment filled lakes, clear lake, ice cap, glacier debris, vegetated area, and poorly vegetated areas within the trimline. These classes are uniquely defined by parallelepiped shaped regions in the four-dimensional image feature centered at the average reflectance value of the particular class. The size of each region is defined by the standard deviations of the reflectance in the four MSS bands. In particular, poorly vegetated areas within the trimline were isolated from regions covered with shrub tundra and lichen cover, primarily through their higher reflectance in MSS band 4 (green, 500-600 nm) and MSS 5 (red, 600-700 nm). The good separability of different classes in feature space indicates that sufficient spectral contrast exists between fresh rock surfaces and the vegetation and lichen-covered rock. As discussed above, Satterwhite and others (1985) found that a lichen cover may increase, decrease, or have no effect on the spectral reflectance, depending on the spectral contrast between the lichens and the bare rock surface. This suggests that the Landsat MSS sensor may be able to detect trimlines only for certain combinations of lichen and rock reflectance and therefore, the procedure followed by Knight and others (1987) may not be directly applicable to other sites. Indeed, the results of Ager and Milton (1987) suggest a broader spectral range may be required to unambiguously distinguish between fresh and lichen covered rock regardless of rock and lichen type. The more recent Landsat Thematic Mapper (TM) and Enhanced Thematic Mapper (ETM+) systems cover the

spectral range from 450 to 2350 nm and are therefore more suitable for mapping trimlines than the older MSS system. Moreover, the higher resolution of the Landsat TM and ETM+ systems (30 m instantaneous field of view (IFOV) compared with the 79 m IFOV of the Landsat MSS) is more suitable to map geomorphological features, such as moraines.

3.4. Feasibility study: Jakobshavn Isbræ

The drainage basin of Jakobshavn Isbræ on the west coast of Greenland is one of the most dynamically active parts of the Greenland Ice Sheet. According to Weidick (1992), between 1850 and 1950, the calving terminus of this glacier receded 25 km from the head of the fjord to its current position. Fresh moraines and trimlines exposed on the fjord walls suggest a lowering of the glacier surface by up to 250 – 300 m since the LIA maximum (Weidick, 1968). Recent results indicate further retreat and widespread thinning over the lower part of the drainage basin. Because of these ongoing changes, as well as the availability of prior studies in this region (Knight and others, 1987; Thomsen and others, 1988; Weidick, 1992), this area was selected for the feasibility study.

The Landsat ETM+ scene shown in Fig. 17 was used for the feasibility study. The imagery, taken on July 7, 2001, covers the surroundings of Jakobshavn Isfjord and a 100 km long stretch of the ice sheet margin north of the fjord.

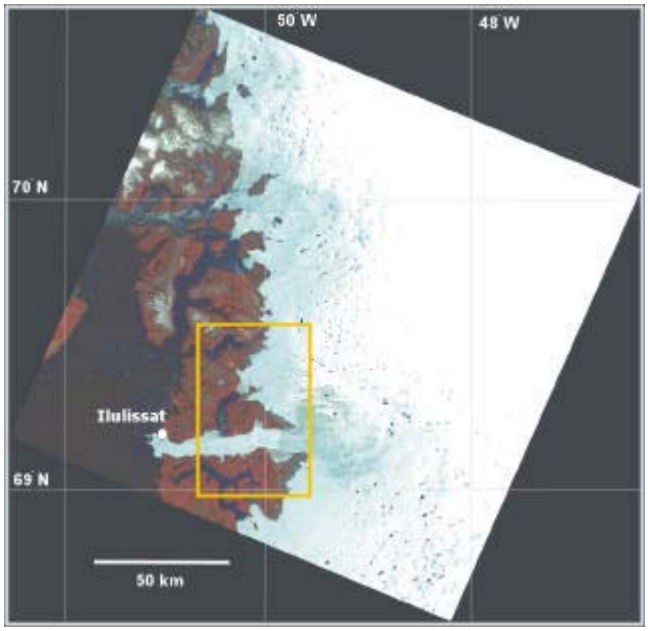

Fig. 17. Location of the study site (boxed area) on Landsat ETM+ imagery (July 7, 2001; scene ID: LE7009011000118850).
Classification results of the boxed area are shown and analysed in this work.

The boxed area around the fjord is selected for this pilot study and is shown in Fig. 18. This color composite is formed from the green, the red and the photographic portion of the near infrared (NIR) of the spectrum (Landsat bands 2, 3 and 4). The resulting "color infrared"

images show vegetation in different hues of red. Different water, snow and ice surfaces are depicted in blue, ranging from the dark blue over sea-water to white over snow covered regions. Exposed rock surfaces and man-made objects are characterized by grayish-brownish hues. At the time of the image acquisition, most of the seasonal snow cover had melted from the coastal mountains, exposing the rock and vegetation surfaces.

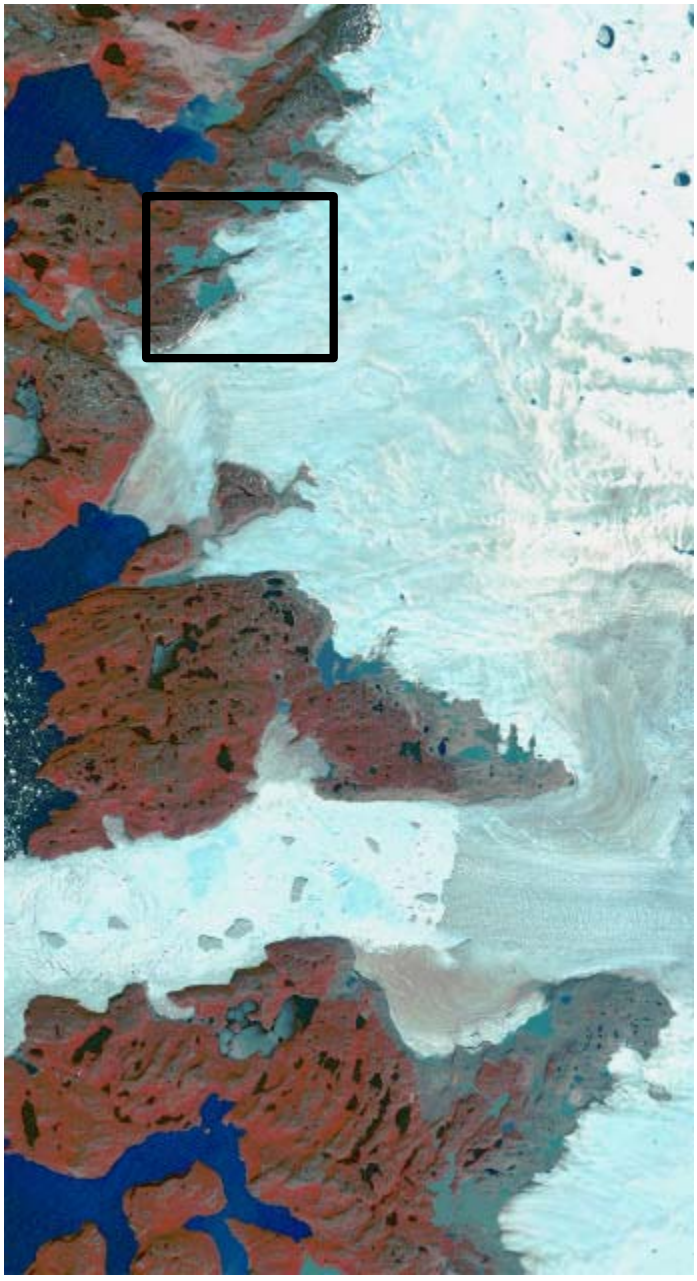

Fig. 18. False color composite of Landsat bands 2 (blue), 3 (green) and 4 (red). Reddish colors indicate vegetation, snow and ice have different tones of blue and white, and exposed rock surfaces and sediments have grayish-brownish hues. Boxed area is enlarged in Fig. 24.

The land area is hilly upland, composed of rounded knolls of crystalline bedrock with elevation ranging from sea level to ~650 m. The bedrock is made up of Precambrian crystalline

rocks, mostly gneiss, with amphibolite and quartzite veins (Geology of Greenland Map Series, 1997). Mica schist and chlorite and sericite schist occur only in the northern part of the area covered by the Landsat imagery, around the glacier of Eqip Sermia. The vegetation is of low-arctic type with predominant plant communities of heath (moor), fell-field, herb-slope, willow-scrub, fen, river- and seashore vegetation. Mikkelsen and Ingerslev (2002) include details on these plant communities as well as a comprehensive plant list of the Ilulissat area.

The area, typical of west Greenland, is characterized by a landscape of aerial scouring (Sugden, 1974). The satellite image depicts the landforms of glacial erosion. Joints, faults and dykes of the bedrock were scoured to form irregular depressions, often occupied by lakes in the deeper basins. Over the exposed land the predominant reflectance feature is the high NIR reflectance (reddish color of the IR composite) indicating that the surface is covered by a patchwork of vegetation and lichens. The brownish-grayish band between the ice sheet and the land corresponds to fresh rock surfaces exposed by retreat of the ice sheet since the LIA. Similar light bands are around many of the lakes, where the former higher water level destroyed the lichen cover.

The open, clear water of Labrador Sea and the supraglacial lakes are shown in dark blue. Most of the lakes in the ice free terrain also have dark blue colors. Lakes close to the ice sheet margin have lighter blue shades indicating higher reflectance in the visible and in the NIR, probably caused by fine grained, suspended sediments from the ice sheet. Fresh snow covering the higher elevation parts of the land and ice sheet surface, is white, while older snow, firn and glacier ice are shown in different shades of blue. The image also depicts the details of the ice sheet surface morphology, including crevasse zones, meltwater streams, and debris cover adjacent to the margin. The Jakobshavns Isfjord is filled with brash ice surrounding a few icebergs and bergy bits. Some of the lakes on the surrounding land are still covered by ice.

In addition to image analysis, exploratory fieldwork was conducted in July 2003, with the main objective of measuring spectra of various land surfaces and vegetation cover, and to map glacio-geological features. In this contribution, only results directly pertaining to analysis and interpretation of the Landsat scene are discussed. A full discussion of the results of the fieldwork will be provided elsewhere.

3.4.1. Spectral measurements

Reflectance spectra were collected in the field using a Fieldspec FR spectroradiometer [on loan] from Analytical Spectral Devices, Inc. This instruments covers the spectral range from 350 to 2500 nm with a sampling interval of 1.4 nm for the region 350 – 1000 nm and 2 nm for the region 1000 – 2500 nm, giving a spectral resolution (defined as the full-width half-maximum of the instrument response to a monochromatic light source) of 3 nm for the interval 350 – 1000 nm and 10 nm for the interval 1000 – 2500 nm. The reflectance of a target surface is computed

by dividing the measured signal from the target by the measured signal from a Lambertian white reference surface illuminated under the same lighting conditions. All field measurements were taken using solar illumination under varying cloud conditions. Because of absorption of solar radiation by atmospheric water vapor in the spectral bands around 1400 nm and 1900 nm, at these wavelengths essentially no solar energy reaches the Earth's surface and the measured signal from both the target and the white reference surface should be zero. In practice, the measured signals contain small but non-zero random noise generated by the instrument and the target reflectance at these wavelengths is computed by dividing two random numbers. Consequently, at these frequencies, the target reflectance spectrum exhibits large noise peaks. For ease of interpreting the measurements, data corresponding to the atmospheric water absorption bands are omitted from the spectral reflectance curves shown below.

All measurements of rock and vegetation reflectance were conducted on approximately horizontal surfaces with the optical sensor enclosed in a pistol grip mounted on a tripod and looking vertically downward through a 1 degree foreoptic. The nominal distance between the target surface and the foreoptic ranged from ~20 cm to ~80 cm, corresponding to a circular viewing area with a radius of 0.3 – 1.4 cm. While ASD failed to provide a viewfinder which would have allowed for viewing the target as seen by the optical sensor directly, the pistol grip was placed above the target as best as possible using a plumbing string. Further, where possible, only relatively large areas (~ 5 × 5 cm or greater) with uniform surface characteristics were selected for spectral measurements. For measuring the reflectance of surfaces composed of morainal material, a similar set up was used, except that a larger target area was viewed (~ 42 cm radius) through a combination of a greater distance between the target and the optical sensor (~ 130 cm) and a 18 degree foreoptic. Reflectance of the Lambertian white reference surface was measured regularly to ensure comparability between reflectance measurements collected at different times and under different illumination conditions. For each target, at least five reflectance spectra were collected and averaged to produce the curves shown below. Some of the reflectance curves are slightly noisy at greater wavelengths due to less than optimal lighting conditions (primarily cloud cover).

The dominant bedrock type in the study region is gneiss ranging in color from light grey to dark charcoal grey. Locally there are clotty segregations of xenoblastic pink orthoclase and grey quartz. It should be noted that the surface is covered with different types of boulders of foreign origin, transported and deposited by the glacier. These various rock surfaces have clearly different spectral reflectances due to their different mineral compositions, as illustrated in Fig. 19 (left panel). Most outstanding is the bright white quartz, which has a high reflectance in the visible range of the spectrum.

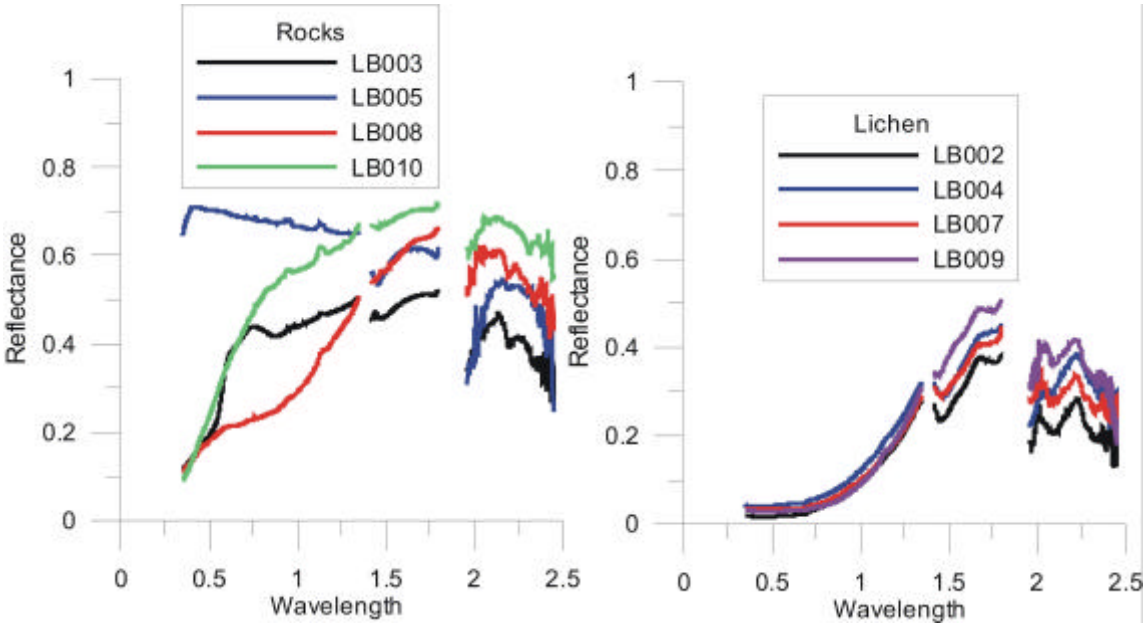

Fig. 19. Left panel: spectra of different rock types; right panel: spectra of same rocks covered by black lichen.

Above the trimline, few of the boulders and exposed bedrock surfaces are free from lichen. Indeed, most of the rock surfaces have a grey to black appearance as a result of being covered with various types of mostly black lichen. While lichens of other colors are present (e.g. green, rusty brown, orange, and white), these cover a significantly smaller surface area and need not be considered in this exploratory study. The effect of dark lichen cover on the reflectance of rock surfaces is obvious from comparison of lichen spectra with the rock spectra in Fig. 19. The right panel of Fig. 19 shows the spectral reflectance curves of the various rock types shown in the left panel, but covered with black lichen. For all rock types, reflectance at visible wavelengths decreases to near zero, while in the near infrared, reflectance is high.

Above the trimline, the land surface is composed of lichen-covered bedrock and boulders, mixed with typical tundra vegetation consisting of differently-colored mosses (ranging from dull black to almost white, but mostly green) and low, shrub-like leafy vegetation. Typical vegetation and moss reflectance spectra are shown in Fig. 20 (left panel and right panel, respectively). The spectrum of leafy plants shows the characteristics of a typical vegetation spectrum. Leaf pigments, namely carotenoid pigments and chlorophyll absorb most light in the visible region, leaving only a minor peak at 550 nm leading to the green color of vegetation. There is a sharp increase in reflectance at 800 nm, called the red edge of the chlorophyll absorption band. The high reflectance of the near-IR plateau is governed by leaf tissue and cellular structure. The reflectance in the short wave IR (SWIR) region is related to biochemical content of the vegetation cover, such as proteins, lignin, and other leaf constituents and the

region also contains prominent water absorption bands at 1400, 1900 and 2450 nm. For mosses, the shape of the spectra is quite similar, although red edge is less developed, or often missing.

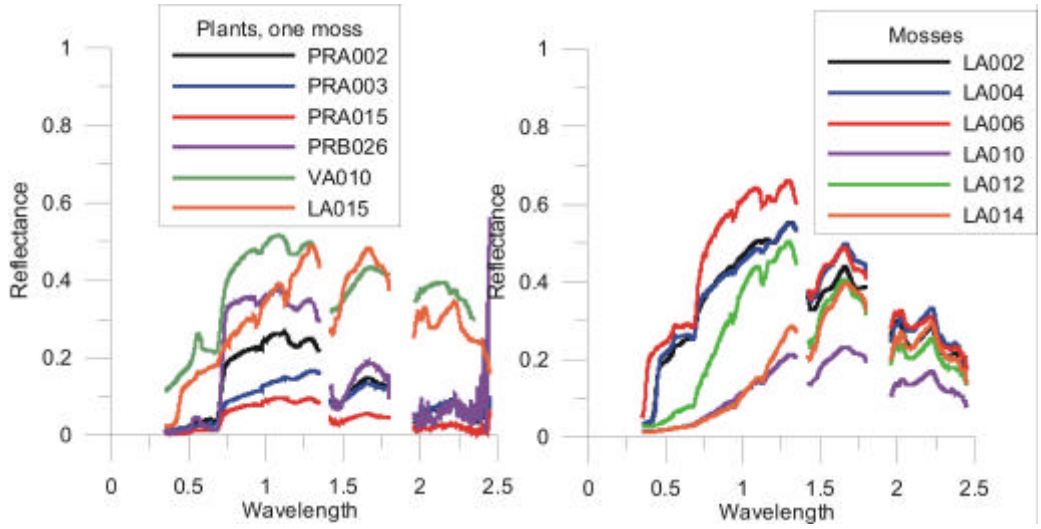

Fig. 20. Left panel: spectra of tundra vegetation; right panel: spectra of mosses

Immediately below the trimline is a narrow zone (1 – 10 m wide) where vegetation is absent and rock surfaces are covered with young black lichens although to a much lesser extent than above the trimline, thus allowing the original rock surface to be readily identified. This zone is, however, too narrow to be distinguished on the Landsat imagery. Below this zone, the surface is mostly devoid of any vegetation and lichen (occasional patches of flowers may occur but these are too small to significantly affect the spectral properties of the surface as viewed by Landsat) and consists of bare bedrock and boulders, gradually transitioning into boulder fields and gravelly glacial till towards the ice margin. Fig. 21 shows reflectance curves characteristic of the recently deglaciated morainal plains. Clearly, these surfaces posses much different spectral reflectance properties than does the surface above the trimline.

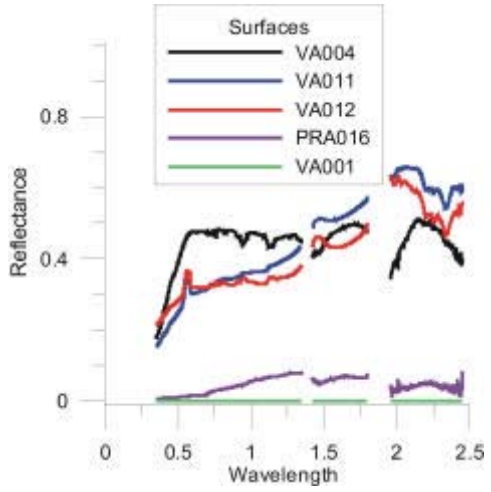

Fig. 21. Spectra of moraines and soils on recently deglaciated terrain

In summary then, the spectral reflectance measurements conducted during the field campaign agree with earlier observations. Lichen cover on rock substrates is reduces reflectance in the visible spectral domain and increases reflectance in the near infrared region. Combined with the typical reflectance signature of vegetation (generally low reflectance in visible with sharp increase at 800 nm, then large reflectance at the NIR plateau that slowly decreases at greater wavelengths), the unvegetated and lichen-free surfaces below the trimline are readily distinguished from the more complex surface structure above the trimline.

3.4.2. Analysis of Landsat imagery

3.4.2.1. Preprocessing

A Level 1, geometrically corrected (L1G) Landsat ETM+ scene, purchased from USGS EROS Data Center, was used in this study (Fig. 17). The Landsat ETM+ sensor collects images in six multispectral bands with 28.5 m pixel size, covering the spectral range from 450 to 2350 nm with 60-200 nm wide spectral bands. The high spatial resolution panchromatic band has a pixel size of 14.25 m and the thermal band has a pixel size of 60 meter.

To facilitate the comparison of the spectral information derived from the Landsat imagery with library and field spectra, the raw Digital Number (DN) values of the six multispectral bands were converted to surface reflectance using an Empirical Line Correction (EML) model (ref). The EML technique uses a band-to-band linear regression between the pixel samples and field reflectance spectra to establish the transformation from the DNs to surface reflectance. The three spectra selected for the correction include the laboratory spectra of felsitic gneiss, clear water and snow (all samples from John Hopkins University IR Spectroscopy Lab, included in spectral library with ERDAS Imagine v 8.6).

3.4.2.2. Surface classification

To identify and characterize the different surface types of the site, different supervised and unsupervised techniques were applied. The results shown in this paper are obtained by maximum likelihood (ML) classification. ML classification is a supervised classification technique that uses training sets of the different cover types to determine the decision boundaries needed to separate the points in the parameter space. First a probability model, usually normal (Gaussian) distribution, is chosen, and then the training samples are used to estimate the statistics (mean and covariance) of the different classes and to determine the discrimination surfaces. The last step is the labeling, when the discrimination function is applied to the entire feature space and all pixels of the image are labeled according to their position in feature space.

We selected thirteen classes with a total number of almost 40,000 training pixels (in 18 regions) on the basis of spectral pattern differences and by using topographic and geologic maps of the area. Prior to the ML classification we also applied unsupervised classification to explore

the spectral information content of the imagery. Unsupervised classification is also called clustering, because it explores the distinct grouping (clusters) of pixels in feature space by optimally partitioning the feature space.

The ML classification map is shown in Fig. 22 (left panel) and the average spectra of the thirteen different surface classes are depicted in Fig. 23.

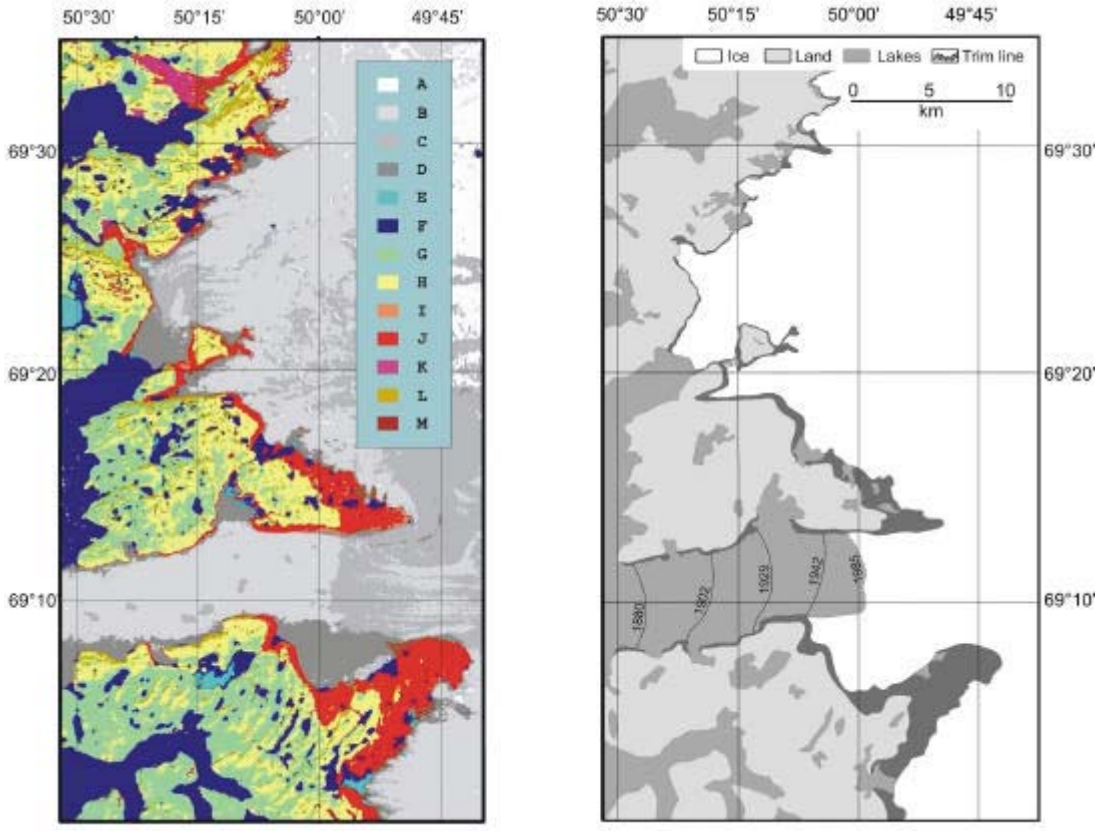

Fig. 22. Left panel: result of ML supervised classification. Right panel: trimline zone mapped from photogrammetry and field surveys.
Classes: A: fresh snow, B: firn; C: glacier ice; D: glacier ice with debris or melt water ; E: melting or thin lake ice and open water with suspended sediments; F: open water; G: lichen and tundra vegetation; H: lichen and tundra vegetation (more lichen than in class G); I: Trimline zone, rock outcrop; J: Trimline zone, clastic rocks; K: Fluvial deposits, outwash; L: Shaded slope; M: Debris covered ice. Southern area on trimline map is from Weidick, 1992, and the northern part is from Thomsen and others, 1988.

Stratified random sampling was used to assess the accuracy of the classification (Richard and Jia, 1999). First random samples were selected in each class; next, their labels were checked against the labels determined by the interpreter from reference data, including field observations and aerial photographs. An overall average classification accuracy of 97.265 % (based on 2 sets of 256 reference pixels) has been achieved.

The spectra in Fig. 23 represent the major landcover types of the area, namely water, different types of ice (snow, firn, cold and melting glacier ice), exposed rock surfaces, and lichen

and tundra vegetation Due to the low spectral resolution of the Landsat sensor (spectral bands are marked in the left panel of Fig. 23), these curves do not depict the fine details of the reflectance spectra. The major spectral features of the different surface types can be clearly identified, however.

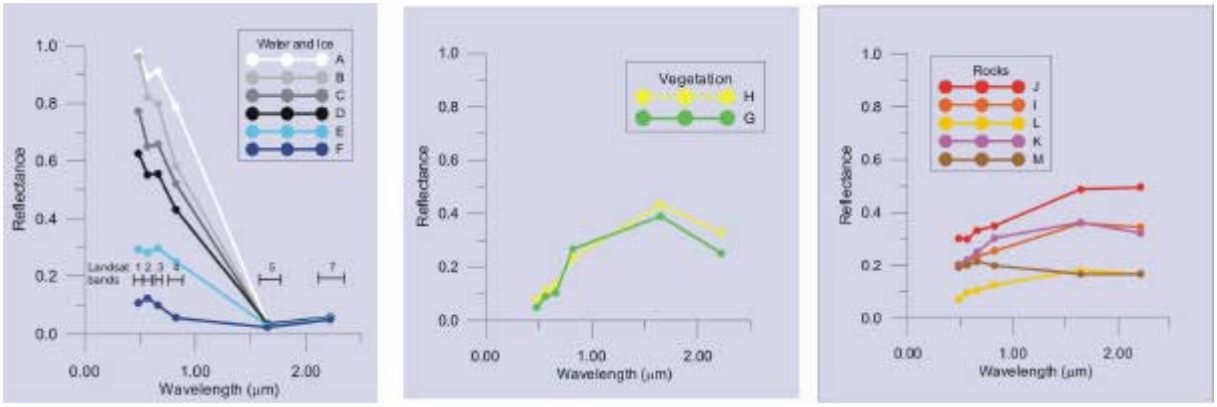

Fig. 23. Average spectra of landcover classes of class map shown in Fig. 22.
Left panel: Water and different types of ice; A: fresh snow, B: firn; C: glacier ice; D: glacier ice with debris or melt water; E: melting or thin lake ice and open water with suspended sediments; F: open water. Middle panel: Lichen and tundra vegetation; G: lichen and tundra vegetation; H: lichen and tundra vegetation (more lichen than in class G). Right panel: Exposed rocks and sediments; I: Trimline zone, rock outcrop; J: Trimline zone, clastic rocks; K: Fluvial deposits, outwash; L: Shaded slope; M: Debris covered ice.

Freshly fallen snow has a very high reflectance in the visible wavelength and the reflectance rapidly decreasestoward the NIR and MIR (spectrum A). Reflectance of snow, firn, and glacier ice can show large variations, depending on the grain size, impurities, and the presence of debris cover and surface meltwater (Hall and Martinec, 1985). Glacier ice has lower reflectance than snow and firn for all wavelengths and the presence of debris or meltwater can decrease the reflectance even further (Spectra 'B', 'C', 'D'). Spectra 'E" cannot be interpreted unambiguously. It occurs on lake surfaces, both along the ice sheet boundary and in land areas. The reflectance in the visible and NIR is significantly higher than the typical values for clear water. This increase can be explained by multiple scattering caused by suspended silt in the water, or by thin ice covering the lake surface. Although the image was acquired in the middle of summer (July 7), the fresh snow in the mountainous area and on the ice sheet implies cold, possibly freezing temperatures. Class F, open water has an overall low reflectance in the visible, NIR and MIR frequencies.

The spectra of biogenic surfaces ('G' and 'H') show the typical spectral signatures of lichens, that is the reflectance maximum in the MIR band (1550-1750 nm). Class 'G' shows more pronounced vegetation signature (increase in the reflectance at the red edge, band 4) with a smaller maximum in band 5, suggesting that this class has more tundra vegetation and less lichen covered rock than class 'H'.

The spectra of the trimline zone classes ('I', 'J', 'K') have very similar shapes, but different overall brightness. These spectra have near constant reflectance in the visible and increasing reflectance in the NIR/MIR and they are in good agreement with the reflectance spectra of the common rocks in the area (see field reflectance curve of gneiss). The brighter surface of class 'I' can be caused by the excess return energy from steep southern slopes illuminated by the sun (no topographic correction was applied to the scene). This, and the slight minimum on spectra 'J' in band 5 (clay minerals or water absorption?) suggest that class 'I' includes mostly rock outcrops, while class 'J' has probably more morainic material. Class 'K' is another typical sand/rock spectra but with an overall low reflectance. Because it usually occurs over shaded slopes with northern exposure, we label this class as shaded slope. Glaciofluvial and fluvial deposits cover the floors of all major, non-ice covered valley, occurring as outwash plains and fluvial terraces deposited from braided rivers. Class 'L' mostly occurs on these outwash plains. The spectral curve shows a red edge, but the surface is much brighter in the visible wavelength than the spectra of vegetation. We assume that this class includes outwash plains with bright, sandy soils, partially covered by vegetation. Finally, class 'M' has medium reflectance in the visible and NIR and slight decrease in the MIR. This surface type is restricted to small zones located in the ice sheet, close to the ice sheet margin and it corresponds to debris covered ice.

3.4.2.3. Trimline mapping

In addition to the pixel based accuracy assessment we also evaluated the accuracy and completeness of the glacial geomorphologic information of the classification map. Our main interest is the distribution of bare rocks and thus the trimline zone around the ice sheet (distribution of classes 'I' and 'J' in Fig. 22, red and orange colors).

The ground truth, shown in the right panel of Fig. 22, is compiled from Thomsen and others (1988) and from Weidick (1992). The 1:75,000 scale photogrammetric map of Thomsen and others is based on aerial photographs of 1:150,000 scale acquired on July 10, 1985. The map was plotted on a Kern PG-2 stereo-plotting instrument connected to an HP computer. It provides physiographic information and surface topography with contour intervals of 50 m on the ice free area and 20 m over the ice sheet. All features of the trimline zone and the glaciers, as well as those related to surface hydrology of the ice sheets are mapped. The mapped ice sheet surface features include supraglacial lakes and streams, moulins, crevasses, as well as lineaments influencing the drainage pattern. The map plotting was supported by surface and aerial field observations. The trimline mapped from the Landsat imagery agrees very well with the trimline mapped by traditional methods. In some valleys connecting the ice sheet with the head of the fjord, the Landsat image shows a spectral signature that could be erroneously interpreted as a trimline zones. These valleys are known to have extensive fluvial deposits and, indeed, our visit to Qingua Kujatleq confirmed that the valley floor is covered by unvegetated sand and silt

deposits. The low spectral and spatial resolution of the Landsat imagery does not allow us to distinguish these fluvial deposits from the moraines of the trimzones.

The detailed map of Thomsen and others (1988) was also used to assess the suitability of the Landsat ETM+ based satellite image maps and classification maps for mapping glacial geomorphology. Fig. 24 compares the satellite image map (upper panel), the supervised classification map (lower left panel) and the detailed geomorphologic map from aerial photography (Thomsen and others, 1988, lower right panel).

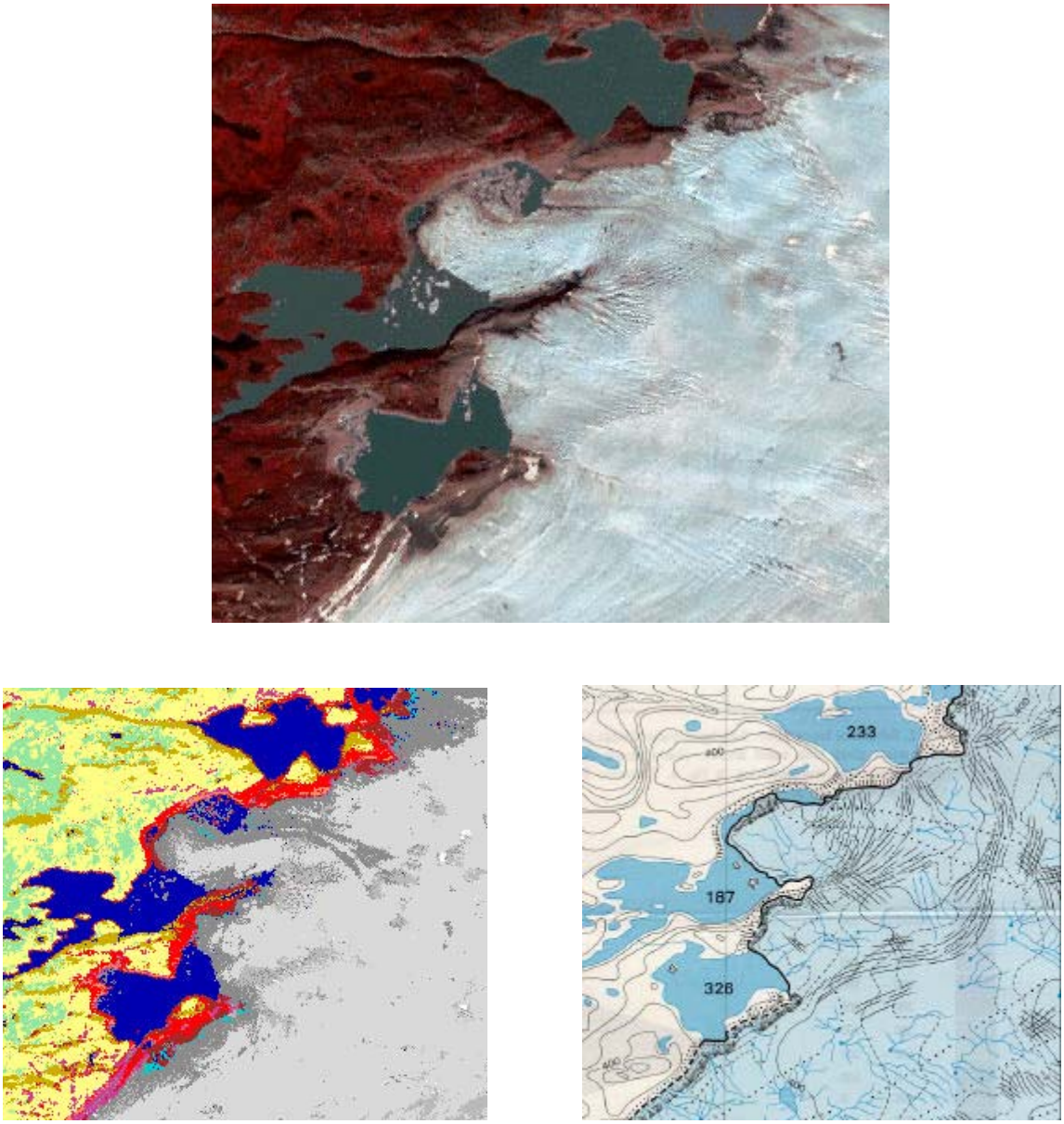

Fig. 24. Geomorphologic mapping with Landsat imagery (black boxed area in Fig. 18)
Upper panel: pansharpened color composite of Landsat bands 2, 3 and 4. Lower left panel: landcover distribution from supervised classification shown in Fig. 22. Lower right panel: enlargement from the geomorphologic map of Thomsen and others, 1988.

The satellite image map is a pan-sharpened false color composite of bands 2, 3 and 4. A special image fusion technique, called Bovery transform (Gupta, 2003, p. 268) was used to merge three multispectral bands with the higher spatial resolution panchromatic band. The fused image has the spatial resolution of the panchromatic band, while preserving the spectral information of the multispectral bands.

The satellite image map is a very rich source of geometric information. It shows many details of the physiography of the ice sheet surface such as crevasse fields, supraglacial lakes, and flow traces that can be used to infer drainage patterns. On the adjacent land, the image shows glacial geomorphological features. This information can be combined with the classification map which distinguishes surfaces based on composition or nature of the land cover (e.g. debris-covered ice, fresh snow, etc.). Together, this provides a more comprehensive picture of the landscape than can be obtained from the pan-sharpened image or the classification map alone.

3.5. Discussion

The primary motivation for the present study is the need to place recent changes observed on Greenland outlet glaciers in the broader context of glacier changes since the LIA maximum, ~1850 A.D. Recognizing the limitations inherent to traditional field-based geological approaches, a multi-spectral Landsat TM scene was anaylyzed to map trimlines in the vicinity of Jakobshavn Isbræ, west Greenland. By utilizing information contained in the six spectral bands, imaged surfaces can be classified according to their spectral reflectance characteristics. As demonstrated in Fig. 24, this classification encompasses more than the distinction between bare rock and vegetation cover that defines the trimline. Indeed, different snow and ice facies are distinguished, as well as various surface lithologies on the surrounding land.

Different surface types can be identified using multi-spectral imagery because of their spectral characteristics. In particular, the shape of the reflectance spectra for lichens is generally very different from that of other surface types or landcovers. Notably, the NIR maximum, around 1600 nm, is a unique feature of the lichen spectra. This suggests that trimlines can be mapped reliably over different rock types using images that cover the broad spectral range up to 2400 nm. As such, the techniques applied in this study present an advantage over trimline mapping from aerial photographs, which may be efficient where the bedrock consists primarily of gneiss, but which may not work very well in the case of dark, basaltic bedrock (Weidick, 1968).

In most cases, the trimline zone and debris-covered ice can be distinguished, but there may be problematic areas, depending on the distribution of surface material. The spectrum of debris-covered ice is the linear mixture of the spectrum ofg the debris material and that of ice. Because ice has a large contrast in NIR, even relatively small patches of exposed ice will significantly lower the reflectance in the NIR as observed in individual Landsat pixels. While this may, in

places, render the boundary between debris-covered ice at the margin of the ice sheet, and ice-free morainal plains, uncertain, this has little impact on locating the actual trimline which is usually found further inland.

In this study, supervised surface classification was used in which different cover types are selected by the operator. This is a feasible approach when considering small regions, as was done here, and it allowed assessing the usefulness of multi-spectral imagery for trimline mapping without the need for designing more automated techniques. For larger projects, however, automation of trimline mapping is not only possible but also desirable. Such automation can be achieved for example by using a multi-dimensional edge detector algorithm to find simultaneous changes in all or most spectral bands. This procedure would extract all boundaries, not only the transition between exposed rock and lichen and vegetation cover. Thus, to obtain the actual trimline, additional constraints are needed, possibly based on a geometry-topological model. For instance, defining the trimline zone as a narrow band bordering the ice margin, candidate boundaries for the trimline can be selected from the entire ensemble of boundaries. It should be noted, however, that in all likelihood the final selection will rely on input from the operator.

Mapping trimlines provides information on the spatial extent of ice margin retreat. While such map-view changes can be obtained with pixel-size accuracy, obtaining a fully three-dimensional reconstruction requires additional information. Accurate determination of the elevations of trimlines is essential for estimating loss in ice volume. Printed maps are available for the region but their accuracy is insufficient for use as reference DEM. Instead, a better approach would be to use stereo pairs of aerial photographs to extract ground control points and to measure a DEM of the study region. Using these ground control points and the DEM, the Landsat image and the aerial photographs can be precisely co-registered and the elevation of the trimline be directly measured from the stereo photographs. This is an established procedure, albeit time consuming, and we are currently in the process of applying this to Jakosbhavn Isfjord and its surroundings.

In addition to mapping different types of surfaces based on their spectral properties, Landsat imagery can also be used for geomorphologic mapping, in particular of features on the ice surface such as flow lines, surface lakes and streams, and crevasse zones. By merging three multi-spectral bands with the higher spatial resolution panchromatic band, the spatial resolution increases from 30 m (Landsat TM) to 15 m for the pan-sharpened image. This dramatically improves the ability to identify morphological features than can be used to describe and constrain the spatial pattern of ice flow and drainage.

In summary then, the pilot study presented here has demonstrated that glacier trimlines can be mapped with confidence from multi-spectral Landsat images (Csathó and van der Veen, in press; and van der Veen and others, submitted). The key to success is the wide spectral range of

Landsat, from 400 to 2400 nm. The procedures are sufficiently expedient to allow for mapping trimlines around the entire perimeter of the Greenland Ice Sheet. Doing so would provide a benchmark for the maximum extent during the LIA. Comparison of this benchmark with the present-day ice sheet would provide more quantitative estimates of changes in ice volume over the past ~150 years, and hence of the contribution of the Greenland Ice Sheet to global sea level since the Industrial Revolution. This would allow the estimated current contribution to be placed in a broader context and aid in better understanding the behavior of the ice sheet and its interaction with climate.

3.6. Summary

This chapter describes a new method that uses spectral information to map trimlines in glaciated terrain. Results from a pilot study are presented to illustrate the accuracy. Ground spectral measurements are used to analyze the spectral information content. I proposed and developed this method (Csathó and van der Veen, in press) with C. J. van der Veen, who participates in glacial geomorphological interpretation and the ground data acquisition is (van der Veen and others, submitted).

During the laser decade our team developed new approachs and novel algorithms for processing remote sensing and photogrammetry data. We are active in several different research areas. For example we have exciting new results for geometric modeling of Declassified Reconnaissance Satellite Photographs and for creating time series of different remote sensing imagery (Csathó and others, 1999d, 2002a and 2002b; Thomas and others, 2000b; Methakullachat and others, 2001; Schenk and others, in press; Abdalati and others, in press) and for the fusion of different sensory data and collateral information (Csathó and others, 1999c; Schenk and Csathó, 2002). No details are presented from these research topics in the dissertation, and the interested reader is referred to the original publications.

My results related to the application of remote sensing and photogrammetry methods for polar research are summarized in Section III of the thesis booklet.

4.0 SUBGLACIAL CONTROLS ON FAST GLACIER FLOW IN GREENLAND

4.1. Introduction

Over the past two decades or so, evidence for active ice sheets – both present-day and in the past – has mounted and the traditional view of ice masses responding sluggishly to external forcings has been replaced by the understanding that large ice sheets can undergo rapid changes. For example, analysis of deep-sea sediment cores has revealed major oscillations in the volume of the Laurentide Ice Sheet, believed to be associated with surges of the Hudson Bay lobe (e.g. Broecker, 1994). On a smaller scale, at the height of the Last Glacial Maximum (~20,000 years B.P.) the ice margin in the Great Lakes region of North America advanced and retreated over several hundreds of km within a short time span (Karrow and others, 2000). Such rapid changes cannot be explained by "conventional" models that have been used so far to simulate ice-sheet evolution. The majority of these models are based on the so-called shallow ice approximation in which the gravitational driving force is balanced by friction at the glacier bed. Allowance has been made for basal sliding where the bed is lubricated, or for deformation of a deformable sediment layer. However, these models may not fully capture the controlling dynamics of ice streams, vast rivers of fast-moving ice embedded in the more slow-moving main ice sheet.

In West Antarctica, ice streams draining into the Ross and the Ronne-Filchner ice shelves have been identified and some of these have been the subject of extensive field campaigns aimed at better understanding the controls on ice streams (c.f. Alley and Bindschadler, 2001, for a recent collection of papers summarizing the current state of understanding). While much progress has been made in elucidating these controls, one unanswered question is why ice streams form where they do? There is no obvious topographic control although the Siple Coast ice streams appear to broadly overlie subglacial troughs and there is some indication that the association between subglacial troughs and ice-stream axes becomes closer up-glacier, where the subglacial relief is greater. Inspection of more fully-developed ice streams, however, shows that their margins may be situated over subglacial highs, lows, or slopes (Shabtaie and Bentley, 1988).

While ice streams are commonly associated with West Antarctica, recent evidence indicates these features may be more common. The first Radarsat mosaic of Antarctica shows ice streams extending far into the interior of East Antarctica (Jezek, 1999). In Greenland, the Northeast Ice Stream was identified on a composite SAR mosaic (Fahnestock and others, 1993). Using paleo indicators, ice streams have been proposed for the Laurentide Ice Sheet as well (e.g., Stokes and Clark, 2001). Thus, without an understanding of why ice streams form in certain locations, and how they move, it may not be possible to fully understand and model the evolution of both the

present-day ice sheets in Antarctica and Greenland, as well as of the paleo ice sheet covering the North American continent during most of the last glacial cycle.

Several recent studies have pointed to the influence subglacial geology may have on the onset of West Antarctic ice stream tributaries. Bell and others (1998) used aerogeophysical observations to construct a model of the magnetic and gravity anomalies along a profile perpendicular to a tributary connected to Whillans Ice Stream. Results indicate that the lateral ice-stream margins coincide with the margins of a sedimentary basin. The upstream edge of this basin is closely coincident spatially with the onset of streaming flow, and Bell and others (1998) conclude that the position of the sedimentary basin controls the position of the ice-stream margins and onset. A similar subglacial geologic control was proposed by Anandakrishnan and others (1998) based on ground-based seismic observations. A seismic profile across the same tributary provides evidence that one margin of the ice stream directly overlies the boundary of a sedimentary basin. The ice stream is within the basin, while outside the basin the ice moves at slow speeds. Anandakrishnan and others (1998) suggest that the sedimentary fill offers much reduced frictional resistance compared to the subglacial material outside the basin, thereby allowing the glacier to reach greater speeds.

Blankenship and others (2001) reviewed available (aero-) geophysical observations to identify geological controls on the initiation of fast glacier flow in the southeastern Ross Embayment. These authors propose three possible geological controls, namely: (1) the availability of mid-Cenozoic sediments deposited on pre-existing rift-controlled topography of the embayment and up onto the flanks of the surrounding crustal blocks; (2) the gradient in geothermal flux from the cold, thick crust characterizing the Whitmore Mountains, across the intermediate thickness of the transitional crust, to the thinner and warmer crust of the southeastern Ross Embayment; and (3) focused geothermal flux associated with localized volcanism or, alternatively, a passive volcanic capping of the mid-Cenozoic sediments.

The objective of the work presented here is two fold. First, the available geophysical data are interpreted to obtain information about the lithology, the structure and the geophysical parameters of the bedrock in the ice covered are in Greenland. Then techniques similar to the ones applied for investigations of the WAIS ice streams are to be applied to data available for Greenland and to explore possible linkages between subglacial geology and ice-sheet flow and to evaluate to what extent basal conditions that facilitate fast glacier movement can be explained in terms of bedrock geology. As discussed more fully below, the working hypothesis (similar to that adopted by Blankenship and others, 2001) is that ice streams form preferentially in regions where the geothermal flow is higher than elsewhere, and where abundant subglacial sediments are available. This hypothesis is based on a comparison between crustal thickness calculated from the gravity and magnetic fields, and estimated balance velocities on the Greenland Ice

Sheet. Where the crustal thickness is comparatively small, and geothermal flux likely to be large, the balance velocities are large. This hypothesis will be developed further by adopting a more quantitative approach to correlate subglacial geology to ice-flow features on the Greenland Ice Sheet.

Available data include a high-resolution Digital Elevation Model (DEM) (Scambos and Haran, 2001; Bamber and others, 2001b) and balance velocities on the Greenland Ice Sheet (Bamber and others, 2000), as well as a suite of geophysical data, remote sensing imagery, and maps. Together, these provide a current snapshot of the ice-dynamical state of the ice sheet. Geophysical data (including gravity and magnetic anomalies) provide information on the current bedrock lithology and geodynamics and can be used to estimate subglacial heat flow and make predictions on the nature of the bed (sedimentary versus crystalline). Furthermore, ice-penetrating radar data obtained by the University of Kansas (Gogineni and others, 2001) are also available and can be used to make quantitative estimates of basal melting in regions of fast glacier flow.

The combined information will provide necessary boundary conditions for a coupled thermo-mechanical ice flow model. This model was developed for application to West Antarctic ice streams but can be readily applied to other fast-moving glaciers and ice streams.

Our approach is essentially different from previous studies aimed at linking subglacial conditions to ice-stream dynamics. Most of these studies have focused on the deformational properties of subglacial material and how changes in these may lead to onset or shutdown of ice streams. In the proposed work, we intend to take a larger-scale view and will seek to answer the question whether large-scale bedrock geology exerts an influence on the flow of overlying ice, perhaps through spatial variations in subglacial heat flow, availability of sedimentary material, and other factors. This approach is similar to that adopted by Bell and others (1998) but extended to the whole ice-sheet scale.

4.2. Subglacial and englacial structures and properties from geophysical data

4.2.1. Potential field data (gravity, magnetics)

The ice sheet covers ~80% of Greenland's interior with an average thickness of about 1.6 km so that direct evidence of the subglacial properties and tectonic processes of Greenland is limited to geological outcrops along its ocean margins. These outcrops reveal crust that is made up of igneous, metamorphic, and sedimentary rocks with contrasting density and magnetization properties (Escher and Watt, 1976; Okulitch, 1991; Escher and Pulvertaft, 1995; Roman, 1998). The physical property variations of these rock types, in turn, generate anomalies in the gravity and magnetic fields of Greenland. The airborne gravity and magnetic data recently acquired for Greenland (Brozena, 1995; Verhoef and others, 1996) offer an exciting opportunity to

extrapolate geologic features from the margins into the ice-covered interior for important new constraints on modeling ice flow.

Fig. 25 gives an example of the enhanced mantle relief (i.e., the Moho) beneath Greenland that can be developed from the terrain for constraining crustal heat flow variations at the base of the ice sheet. Here Braun, Csathó, Kim and von Frese (in preparation) modeled the gravity effects of the water, ice, and rock components of the topography for comparison with the free-air gravity anomalies at 20 km altitude. The terrain and gravity data were obtained from the Danish Cadastre and Survey. The free-air gravity data, which included the results of an extensive aerogravity survey of Greenland by the US Naval Research Laboratory (Brozena, 1995), were upward continued to 20 km altitude to enhance the regional signals of the uncompensated crustal components.

Using the correlation spectrum between the two data sets, spectral correlation filters separated the terrain-correlated and terrain-decorrelated (i.e., uncorrelated) components of the free-air anomalies. By subtracting the terrain-correlated free-air anomalies from the terrain gravity effects, the compensated terrain gravity effects were estimated for insight on the isostatic properties of the crust. The lack of compensated terrain gravity effects in the ambient free-air gravity field reveals the existence of annihilating gravity effects that constrain mantle relief and crustal thickness variations assuming an appropriate crustal compensation model and density contrasts between crust and mantle. The Moho in Fig. 25 was obtained by the inversion of the annihilating terrain gravity effects assuming a 0.4 gm/cm^3 density contrast across the seismically determined mean Moho depth of 25 km. This methodology was developed and validated in crustal studies of the Antarctic (von Frese and others, 1999), and East Asia where the estimated Moho was found to be well within 10% of that observed by a relatively limited number of large offset seismic studies. Warmer crust is suggested where the gravity Moho (Fig. 25) is shallowest in northern Greenland, which may enhance neotectonics and glacial activity. These gravity estimates were developed to augment seismic Moho estimates from 20 broadband stations on Greenland (e.g., Dahl-Jensen and others, 2003) and about 65 offshore seismic estimates that are clustered mostly along the oceanic margins of Greenland and Iceland (Roman, 1999; Leftwich and others, 2001, 2003). The gravity Moho estimates match the seismic estimates quite well except for three stations in central and southern Greenland where the gravity estimates are shallower by 5-10 km. These mismatches can reflect the occurrence of cold Archean crust in central and southern Greenland with somewhat higher density rocks than we had assumed for the analysis, and/or seismic errors due to strong converted phases generated at the base of the ice sheet (Dahl-Jensen and others, 2003), or other errors. Within the adjacent regions, the gravity and seismic Moho estimates also match very well except over the thermal plume in east central Iceland where the gravity estimates are deeper by about 7 km. Assuming the seismic estimate is an accurate benchmark, we can obtain a matching gravity estimate by

reducing local upper mantle density by a few percent. This mantle density reduction can result from the enhanced temperature effects of partial melting and thermal expansion (Leftwich and others, 2003).

4.2.2. Radar

During the 1990s, extensive radar surveys of the Greenland Ice Sheet were conducted by the University of Kansas (Chuah, 1996; Chuah and others, 1996; Gogineni and others, 2001). The data have been used to track internal layers in the ice and to estimate melt rates using continuity arguments and spacing between layers identifiable on the radar images (Fahnestock and others, 2001). A profile from the ice penetrating radar data set is shown in Fig. 27. The left side is a typical profile line from the radar data, illustrating internal layering within the ice and the ice-subglacial boundary. Most of the profile lines show similar simple features. However, some of the profile lines show some spectacular features above the subglacial boundary, as illustrated in the right side of the profile in Fig. 27. These features were noted previously (Legarsky and others, 1997) and attributed to hills in the subglacial topography. However, it is fairly clear from these images that a reflection is obtained directly beneath the anomalous features and this lower reflection corresponds to the depth and morphology of the subglacial reflection. Therefore, it is very likely that the anomalous regions are caused by density changes (and hence the dielectric properties that can cause a reflection) within the ice related to some post-emplacement event, such as development of shear zone along an ice stream boundary. Part of the objective of an on-going research is to investigate the University of Kansas data set in a thorough manner to determine the true dimensions and morphology of these features and to correlate the size location of these features with anomalous features determined from the other geophysical measurements. Features that are common to the ice sheet anomalies and the geophysical interpretation suggesting the location of hot spots (e.g. volcanic activity) may indicate the presence of post glacial volcanic activity, including the possibility of age dating the volcanic activity.

4.2.3. Linkage between subglacial geology and ice flow

Existing models of the Greenland Ice Sheet assume uniform basal boundary conditions. However, as noted above, the Moho under the ice varies considerably and, consequently, spatial gradients in geothermal heat flow are to be expected. Preliminary results suggest a correlation between subglacial geology and flow of the ice sheet. The seismically most active area of Greenland is located over the thinned crust of the Caledonian mountains of East Greenland. The ice flow in the interior of the NE quadrant of the Greenland Ice Sheet is focused in a large ice stream draining the north side of the summit dome (Fig. 26). The rapid ice flow was first detected from surface undulations mapped with satellite imagery (Fahnestock and others, 1993). This Northeast Ice Stream is also distinctly visible in the surface topography, with high

amplitude undulations within the stream and deep troughs along the margin (Fahnestock and others, 2001).

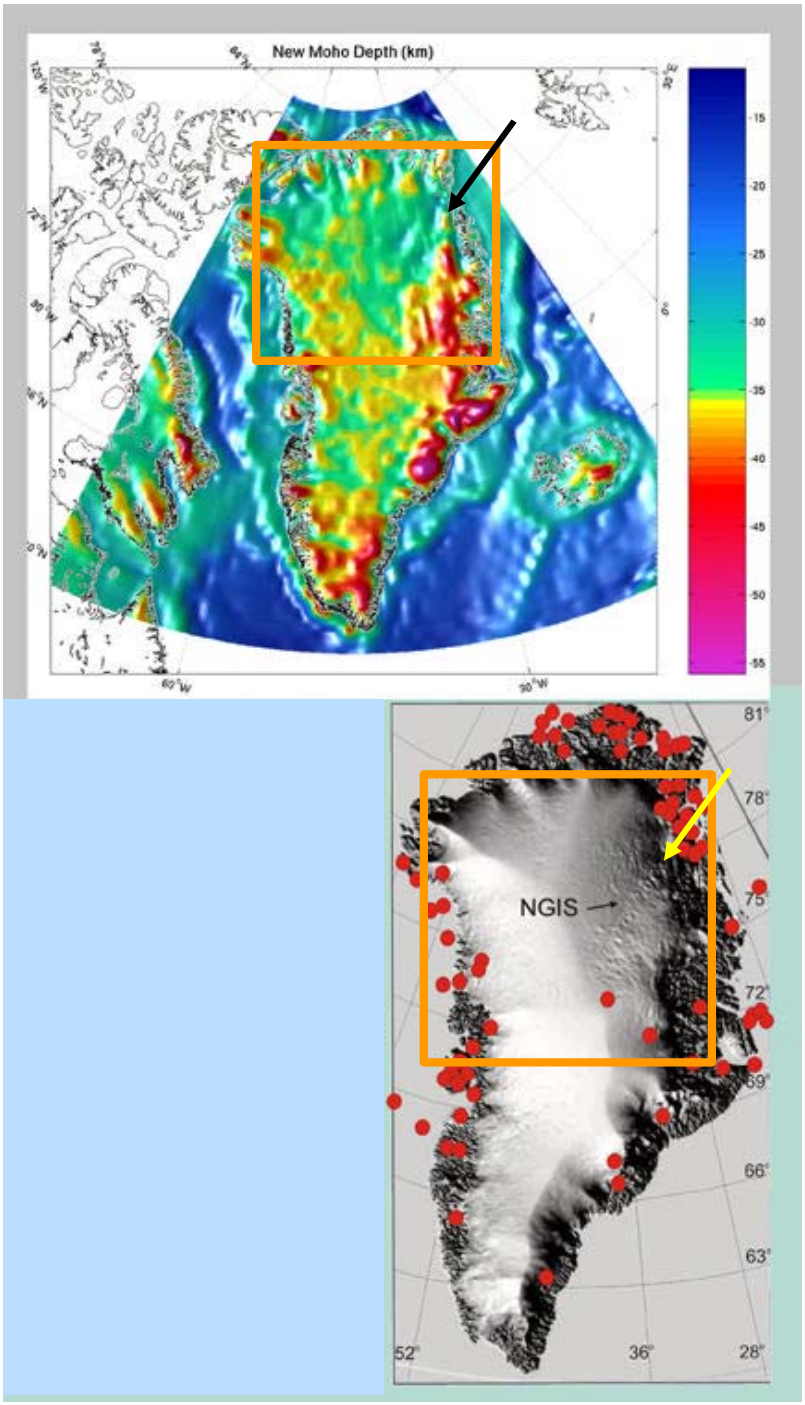

Fig. 25. Moho depth estimated from free-air gravity anomalies.
Gravity data were provided by R. Forsberg, KMS, Denmark

Fig. 26. Shaded relief topography of Greenland ice sheet showing the Northeast Greenland Ice Stream (NGIS) and earthquake locations between 1940 and 1978.
DEM is from J. Bamber and others (2001b) and earthquake locations (red circles) from Gregersen, 1997.

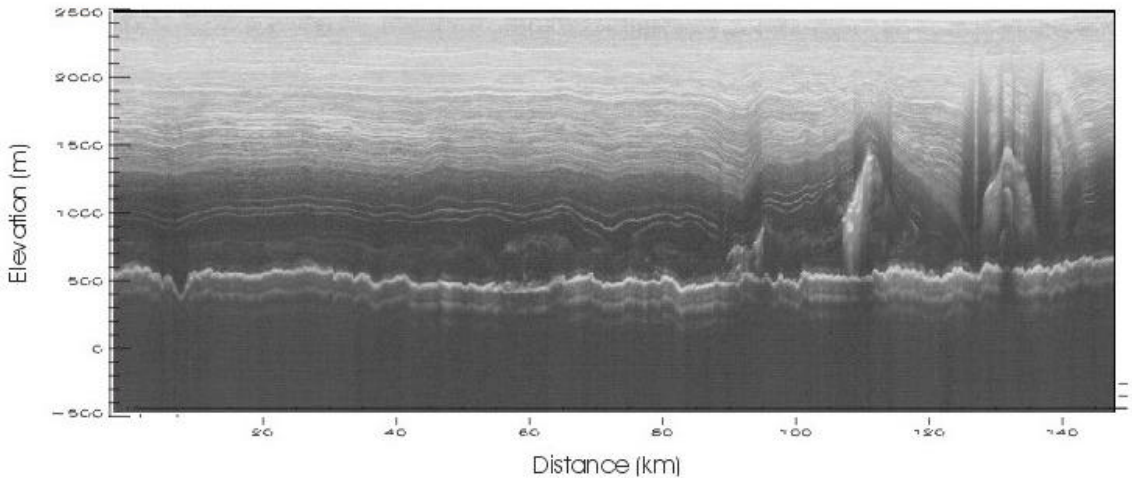

Fig. 27. B-B' Ice penetrating radar profiles showing englacial reflectors.
Data were collected by Prasad Gogineni, Univ. of Kansas, for location of profile see Fig. 28.

Analysis of the surface topography, the velocity distribution, and the bedrock topography has shown that the ice stream overlies a channel along part of its length and the bed topography appears to play a role in the initiation of the ice stream (Joughin and others, 2001). Joughin and others (2001) also argue that the bedrock geometry alone cannot explain the linear geometry of the stream and its sharp onset. The geophysical data suggest that the Northeast Ice Stream is strongly controlled by crustal structure. The southern margin of the ice stream roughly coincides with the large change in crustal thickness along a SW-NE structure (Fig. 25 and 26, arrows) and the seismically most active area is located where the ice stream forks feeding Storstrommen and Zachariæ Isstrom (red circles in coastal region of NW Greenland in Fig. 26). Moreover, high basal melt rates, detected by radar sounding indicates geothermal fluxes 15 to 30 times the continental background at the onset of the ice stream, possibly related to a caldera structure indicated by the aeromagnetic survey (Fahnestock and others, 2001).

In the NW part of the ice sheet the relationship between the surface undulations, bedrock troughs, and the present ice flow pattern is not as evident as for the Northeast Ice Stream. This section of the ice sheet is drained through the Humboldt, Petermann and Ryder glaciers. Joughin and others (1999) and Rignot and others (2001) combined satellite radar interferometry, ice-penetrating radar profiles, and elevations, to study the ice flow and estimate mass balance of the drainage basins of these glaciers. The analysis of existing data over the Petermann and Humboldt glaciers and their catchment areas in northwest Greenland has provided new insight into the glacier dynamics of the region, especially into the development of recent changes. Petermann Glacier, which is confined by a narrow fjord, drains the largest part of the section and has the greatest overall discharge. Inspection of the SAR imagery and the DEM shows that the catchment area of Peterman Glacier extends into what would be expected to be the catchment basins of the Humboldt Glacier to the west and the Ryder and Steensby glaciers to the east.

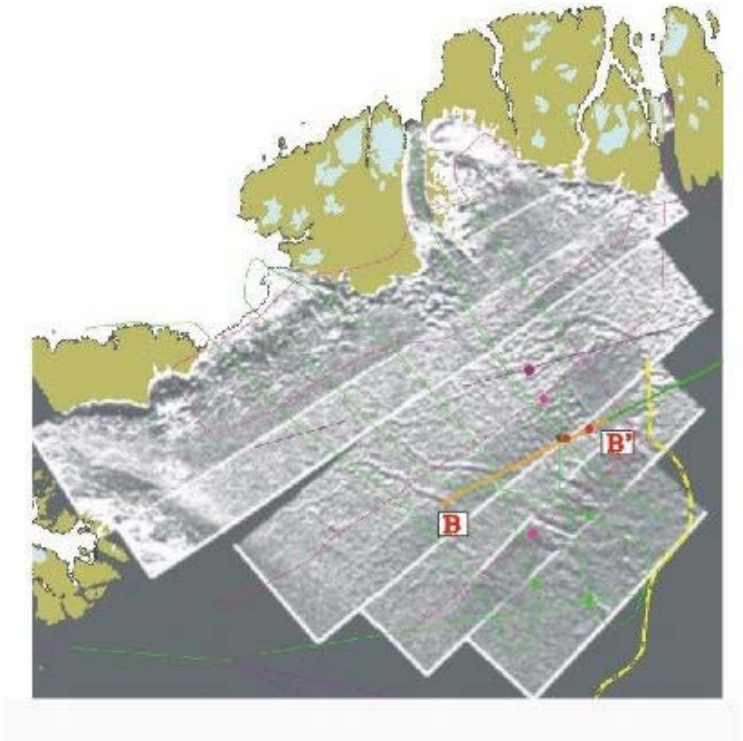

Fig. 28. High-pass filtered ERS-1 SAR imagery showing ice sheet surface features. Yellow line marks subglacial trough.

Evidences of recent changes in ice dynamics include relict flow features on the Humboldt Glacier, strong englacial reflectors under surface lineations along the major channel of the Petermann Glacier (Fig. 27), and a deep, water-filled bedrock trough located under an elongated surface depression extending across the upper part of the Petermann catchment basin (Fig. 28). The signatures of surface lineations and bedrock reflectors near the main channel of Petermann Glacier are similar to the recently abandoned shear margin between ice streams B1 and B2 in West Antarctica, mapped by Clarke and others (2000). The water-filled bedrock trough, first described by Ekholm and others (1998), coincides with the eastern boundary of one of the largest magnetic anomalies of the ice sheet. Here, basal melting is possibly caused by increased geothermal flow related to recent volcanism. Disturbance of internal layers, similar to the signature observed over the Northeast Ice Stream by Fahnestock and others (2001), also indicates basal melting along the major channel of the Petermann Glacier. These evidences suggest that some of these features represent former shear margins of an ice stream which has recently shut down.

These recent results suggest important differences in crustal structure between northern and southern Greenland. Large magnetic anomalies (Fig. 29, left panel) and the basal melt detected by radar (Fig. 27) might be indications of underice volcanism or shallow intrusions. Comparison of free air-gravity map (Fig. 29, right panel), bedrock surface elevation (Fig. 30) and ice velocity reveals that the flow of Humboldt glacier is not controlled by bedrock topography only. For

example, the southern boundary of the glacier is over flat bedrock and it coincides with the flank of a free-air gravity maximum and probably with the southern boundary of the sedimentary Franklinian basin. Taken together, the thin, hot crust, recent volcanics, sedimentary basins and ice stream flow in northern Greenland suggest that the ice dynamics are strongly modulated by the underlying geology, much like the case for the West Antarctic Ice Sheet.

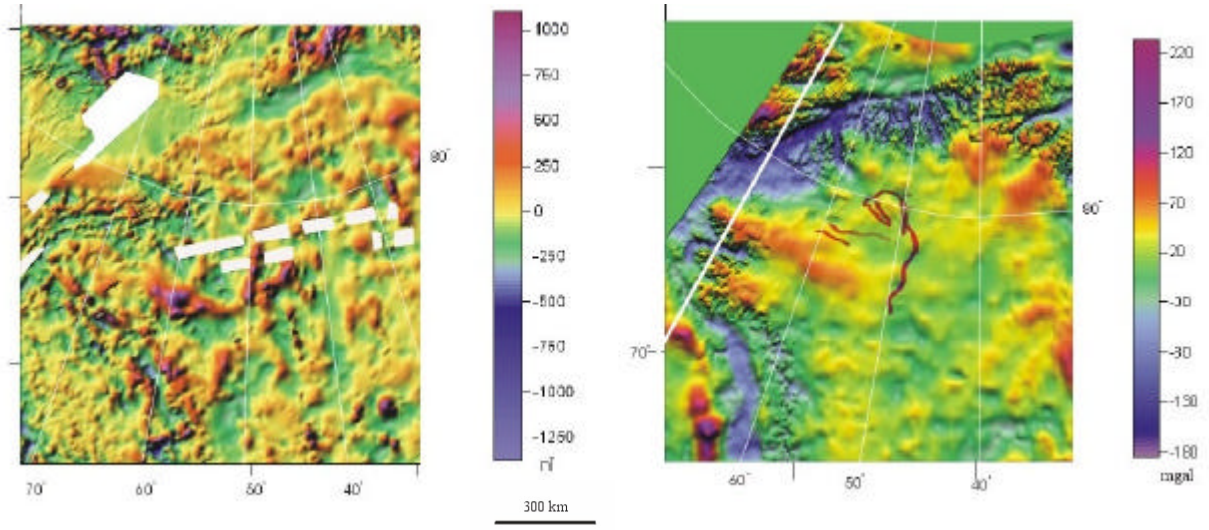

Fig. 29. Total field magnetic and free-air gravity anomaly maps of NW Greenland (data from Verhoef and others, 1996, and from R. Forsberg, KMS, Denmark)

A preliminary comparison between estimated balance velocities (Bamber and others, 2000) and bedrock properties and crustal thickness inferred from geophysical data suggests that other regions of fast flow may also be linked to the underlying geology (e.g., Jakobshavn Isbræ, Kangerlussuaq Glacier). A more formal and quantitative correlation will be conducted using the surface topography (Scambos and Haran, 2001), balance velocities and, where available, measured speeds. Ice velocities cannot be directly correlated with parameters describing subglacial geology because ice discharge increases towards the margin to evacuate snow accumulating in the interior. However, as a start, spatial gradients in ice velocity may be considered similar to the analysis of Layberry and Bamber (2001). Following Bindschadler and others (2000), these authors consider the logarithm of the surface velocity to identify onset regions of streaming flow. Where ice flow is mostly due to internal deformation, this quantity is in first approximation a linear function of the logarithm of the driving stress. However, the introduction of a weak bed will introduce an increase in ice discharge for a decreasing driving stress, and thus result in an inflection point in the plot of log(speed) as a function of log(driving stress). Other quantitative measures for locating switches in ice flow regime include the transverse velocity gradient, which characterizes lateral shear margins.

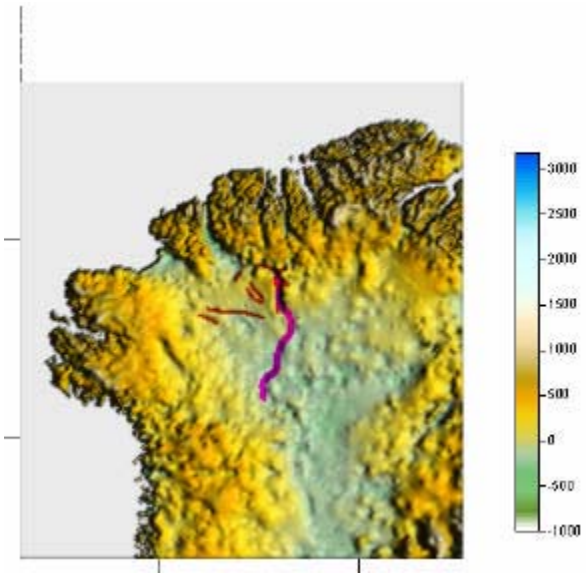

Fig. 30. Bedrock surface elevation from airborne radar data
(data from courtesy of J. Bamber, University of Bristol, UK, Bamber and others, 2001a)

Another objective of the study is the mapping of subice lithology. First a 3-D model of ice stratigraphy and englacial reflectors is created from ice-penetrating radar data (see section entitled 'Radar' above). Then to study the sub-ice geology, I follow the methodology recommended by Bell and others (1998) and Studinger and others (2001). I use 2 ¾ and 3 D potential field modeling to map the extent of sedimentary rocks and the shape of volcanic and intrusive bodies. The bedrock surface and lithology, the estimated basal melt, and the location of relict shear margins will be used to describe recent changes in ice flow history. These studies are essential to understand the dynamics of the region, such as the migration of catchment basin boundaries, the timing of the shut down of streaming flow, and the influence of increased basal heat flow to the current flow regime. The results are also relevant to the reconstruction of the tectonic history of the central part of the Greenland Ice Sheet, since the increased geothermal flow may indicate thin crust resulting from thermal erosion related to the hotspot activity about 110-90 Myr B. P.

4.3. Summary

This chapter presents the first results of the integrated interpretation of geophysical, glaciological and remote sensing data of the Greenland ice sheet. The data were collected and provided by different research groups and they are compiled and stored in our Greenland GIS Database System. The computation of the Moho surface from the free air gravity data is done by Kim and von Frese. The postprocessing and rectification of the different data sets as well as the interpretation is my work (Csathó and others, 2001b). The glaciological interpretation is provided by C. van der Veen. We propose to collect additional geophysical data, needed for

quantitative analysis, during the IGY (Braun and others, in press). We are currently seeking funds for post-processing of the radar profiles (migration, 3D visualization and interpretation).

My results related to the geological control on the ice flow and to the study of the bedrock lithology and geophysical properties of the ice covered areas in Greenland are summarized in Section IV of the thesis booklet.

5.0 Application of Geophysical and Remote Sensing Methods for Mapping the Transantarctic Mountains Rift Zone, Southern Victoria Land, Antarctica

The Transantarctic Mountains (TAM) rift flank uplift has been developed along the ancestral margin of the East Antarctic craton, rimming the thin lithosphere of the West Antarctic rift system. TAMARA was a collaborative research program integrating new aerogeophysical data, acquired as part of the project in 1997-98 by a cooperative US-German field campaign, with satellite imagery, geological and structural mapping, and existing geophysical data, to map the large-scale structural and magmatic elements of the crust of TAM in Southern Victoria Land where the rift flank is along a transverse accommodation zone.

The TAMARA survey area can be divided into three main complexes of distinct magnetic character (Fig. 31). To the east of the line coinciding with the mountain ridge of the Royal Society Range a broad magnetic low is dominating the area toward the McMurdo Sound. This low encompasses the strong magnetic high associated with the Mt Discovery - Mt Morning complex.

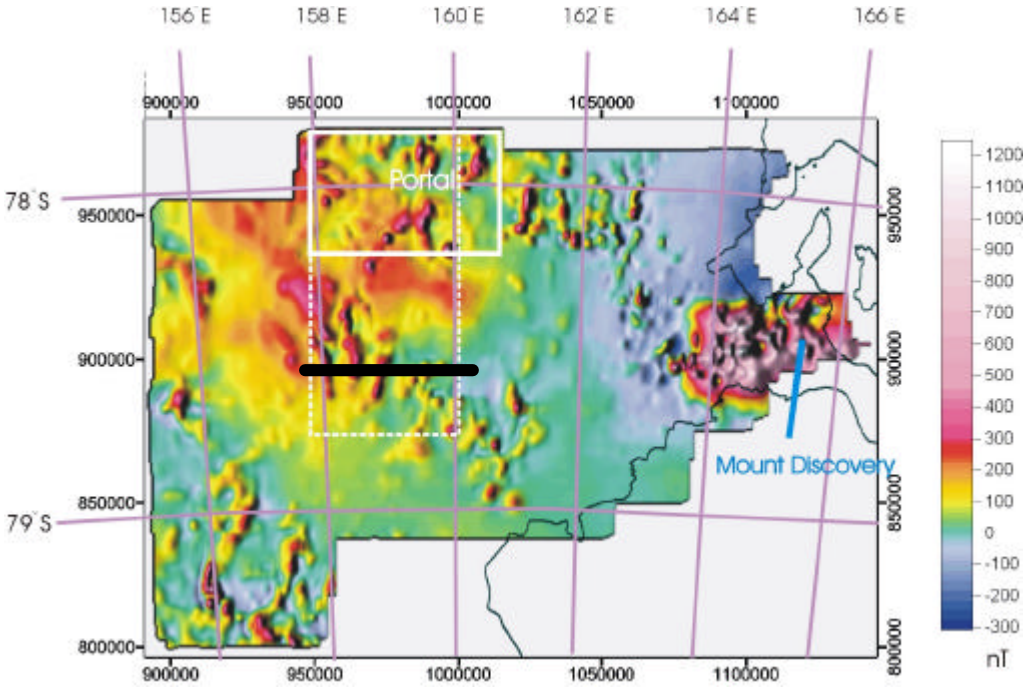

Fig. 31. Total field aeromagnetic map, TAMARA area, Southern Victoria Land. Airbornne magnetic data were processed by Detlef Damaske, BGR.

To the west a broad magnetic high appears to extend from the polar plateau into the TAM. In parts, smaller scale anomalies or anomaly chains of positive amplitude appear to overlay this high, extending from the third, basically magnetically quiet zone of the central and southern survey area. Numerous Ferrar dolomite outcrops, usually indicated by small scale, high amplitude magnetic anomalies, are found in the western and central part of the site (Fig. 32).

Fig. 32. Thick Jurassic Dolerite sill in outcrop at the Warren Range.
Photograph is from courtesy of Terry Wilson (OSU)

The magnetic anomaly map indicates that the Ferrar dolerite province continues under the ice cover and so does the Radian lineament, which is ESE-WNW structure extending from the mountain toward the ice sheet through the Portal (Fig. 31). To remove the topographic effect we upward continued the anomaly map and a pseudogravity map was also computed. Our interpretation suggests that the Radian lineament does indeed extend westward across the entire mountain belt and that it is not a single, straight structure, but rather a series of asymmetric grabens. A range of modeling experiments confirmed that the simplest interpretation of the magnetic data over Ferrar dolerite outcrops consists of a set of asymmetric, low-angle dykes with a large, subvertical feeder body below them (Fig. 33).

Joint interpration of the geophysical and glaciological data suggested that the mountain belt structure and geology has a profound influence on ice flow pattern and ice dynamics. For investigating the role of geologic control on glacial drainage and to map major geological boundaries on ice covered areas we combine and jointly analyse geophysical, remote sensing and glaciological data. Changes in structurally- or lithologically-controlled bedrock relief, in the type of the materials constituting the glacial bed and in heat flux associated with volcanism, are aspects of subglacial geology that can fundamentally affect ice sheet flow behaviour. Understanding the relationship between sub-glacial geology, regional ice-flow and ice sheet surface features help to assess the controls on glacial drainage system, mass balance and stability of the Greenland and Antarctic ice sheets.

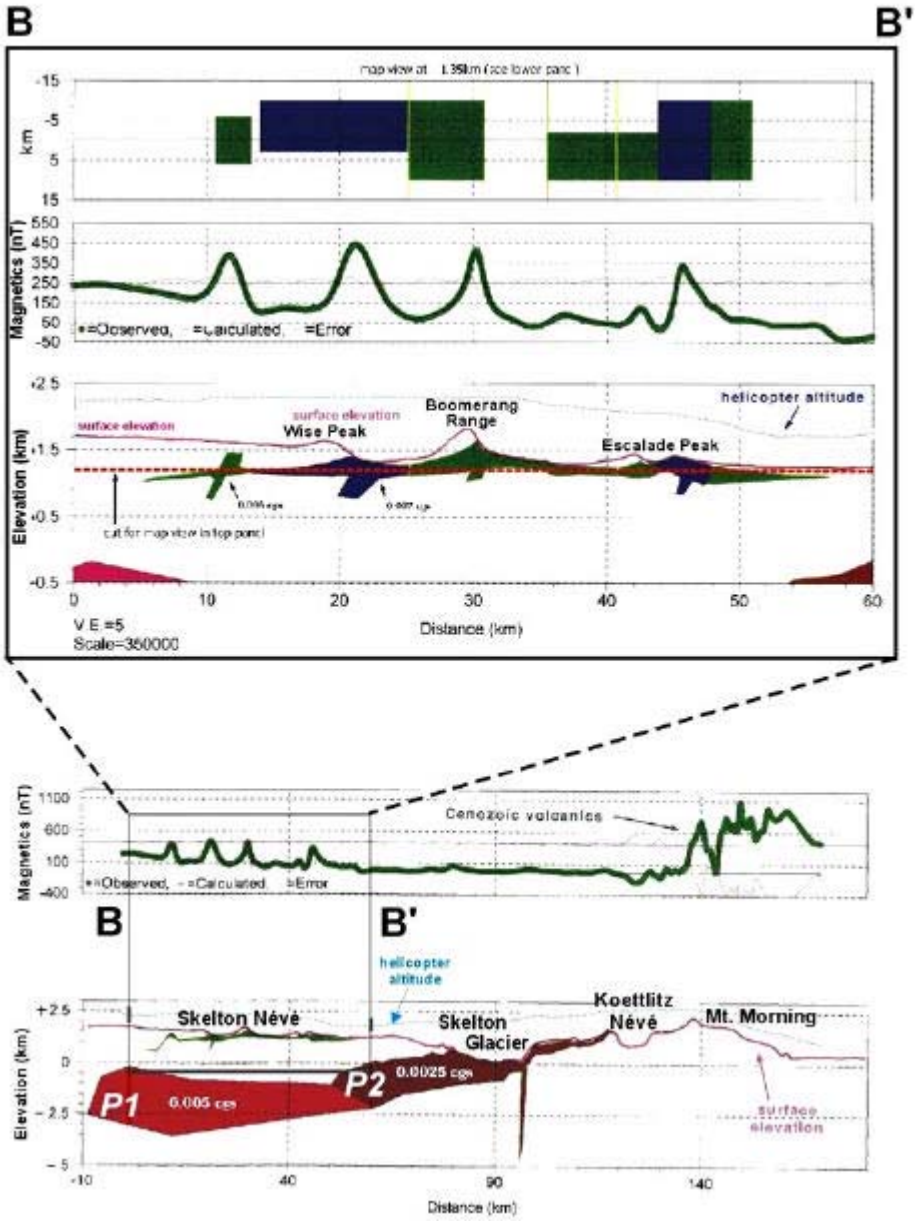

Fig. 33. 2 ¾ D model solution to explain magnetic anomalies over the area of Jurassic outcrops. See Fig. 31. for location of the profile (thick black line)

We use a combination of geophysical (airborne magnetics and gravity, ice-penetrating radar) and remote sensing (laser altimetry, visible, NIR and SAR imagery) methods to map ice-covered areas and to establish the relationship between geologic boundaries and surface features apparent on satellite imagery. For example the analysis of glaciological data reveals increased ice velocity, suggesting that the subglacial bed is soft, perhaps lubricated by meltwater or water–saturated till. The Intensity-Hue-Saturation fusion of the magnetic map with satellite imagery (Fig. 34) gives a vivid impression of the fast ice flow along the lineament and it also indicates the a connection between the ice surface topography and magnetic anomaly pattern.

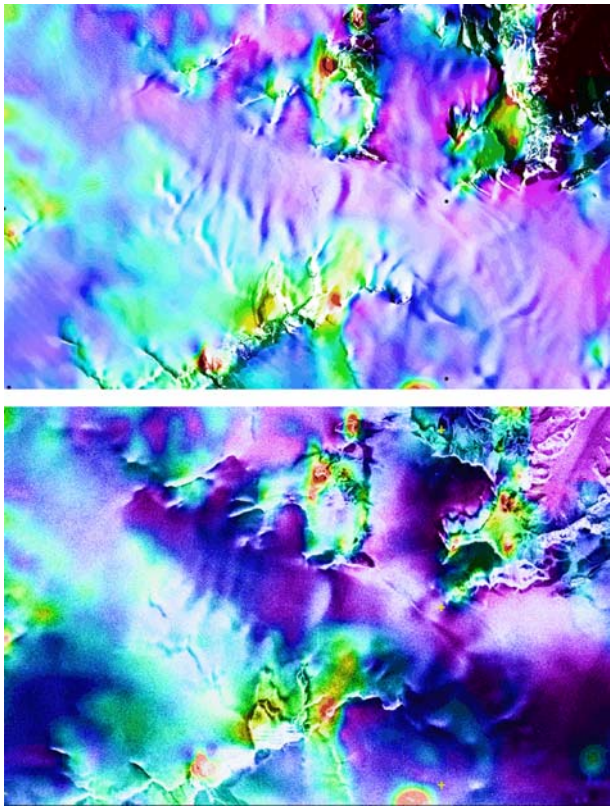

Fig. 34. Intensity-Hue-Saturation fusion of magnetic anomaly grid and Landsat imagery (upper panel) and magnetic anomaly grid and SAR imagery over the Radian lineament.
Color information (hue) is from the magnetic map and the intensity variation is from the satellite imagery. See Fig. 31 for the location of the composite imagery (white box in upper part of TAMARA survey site).

High-resolution, precise surface elevation data were mapped by NASA's Airborne Topographic Mapper (ATM) laser altimetry system over several sites in southern Victoria Land in December, 2001. The ATM surveys were conducted as part of a joint project of NASA and NSF to evaluate the potential of laser altimetry for topographic mapping in the Antarctica and to survey calibration/validation sites for the NASA ICESat (Ice, Cloud and Land Elevation Satellite) mission. Airborne laser altimetry (also called LIght Detection And Ranging or LIDAR) has been established as one of the most valuable tools in mapping surface topography and monitoring surface elevation changes of glaciers. Estimates of thickening and thinning rates measured by airborne lasers have been used to assess the mass balance of the Greenland and Antarctic ice sheets and alpine glaciers around the world (e.g., Krabill and others, 1999 and 2000). The main goal of the program presented here is to assess its potential for mapping glacial and tectonic geomorphology in the Antarctic polar environment.

The ATM system combines high-pulse laser ranging with a scanning capability (Krabill and others, 1995). The laser is operated in the blue-green spectral region and its beam is directed toward the surface by a nutating mirror producing a set of overlapping spirals of data points as the aircraft moves forward. The data processing starts with combining the position and attitude

of the platform with the laser range to compute the position of the laser footprints on the ground. The large reflection variation of the site caused the saturation of many laser returns, resulting a large number of outlier observations. To remove the outliers and to reduce the random noise of the ranging we developed a new postprocessing method (Csathó and others, 2001c, Schenk and others, 2001; Lee and others, in press). After the removal of the outlier observations the irregularly distributed data set is interpolated into a regular grid with 2-4 meter resolution. The Antarctic ATM mapping mission and the data processing, including questions of outlier detection, interpolation, feature extraction, data fusion and visualization of laser scanning data are summarized in Csathó and others (in press).

The results of the airborne laser mapping of the Dry Valleys and the Cenozoic volcanoes around southern McMurdo Sound illustrate the different geomorphic applications (Csathó and others, 2003). The shaded relief DEMs depict micro-topography that reflects the processes shaping the Earth's surface. Information about the past history of glaciers can be inferred from surface topography. Glacio-geomorphologic features (e.g., trimlines, terminal moraines, meltwater channels) left behind as glaciers receded provide valuable, and often the only, information about past glacier extent. The high resolution DEM of the Canada glacier, shown in Fig. 35, depicts the crevassed surface of the glacier snout, a circular moraine located about 2 km from the glacier front, melt water channel, and the lakes occupying the valley floor.

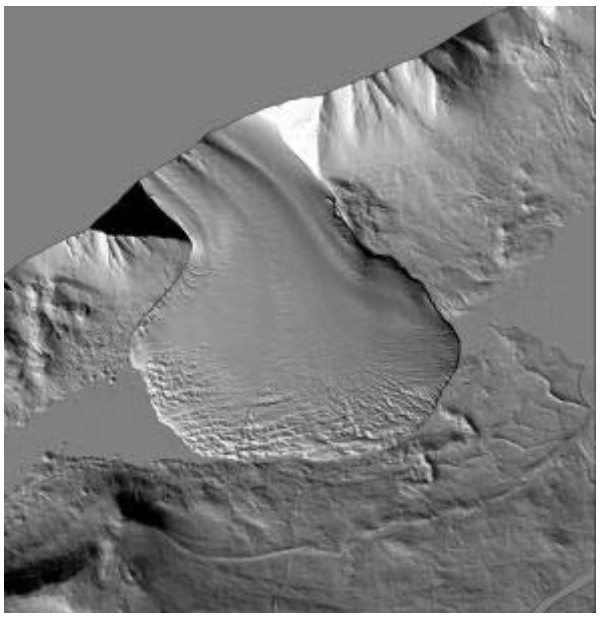

Fig. 35. Shaded relief imagery of the 2 meter resolution DEM derived from airborne laser survey over the Canada glacier in the Dry Valleys, Antarctica.
The shaded relief image measures about 10 km across.

The shape of permafrost features, such as the striking circular, labyrinthine, polygonal and striped patterns of stone and soil, can reflect the presence, thickness and nature of subsurface ice. The microtopography of of the Mullins glacier entering into the Beacon Valley is shown in

Fig. 36. Recent investigations suggest, that the ice under the rock glaciers of the Beacon Valley are from the Miocene age, making it perhaps the oldest ice in the Earth (Sugden and others, 1995). The high resolution laser survey allows us to create a very precise, high resolution DEM of the rock glaciers and the valley floor, needed for accurate measurement of its movement from SAR interferometry. Moreover, the DEM laser is also suitable for measuring the geometry of the unsorted rock polygons. The formation of these striking features is currently the subject of intense research (Kessler and Werner, 2003).

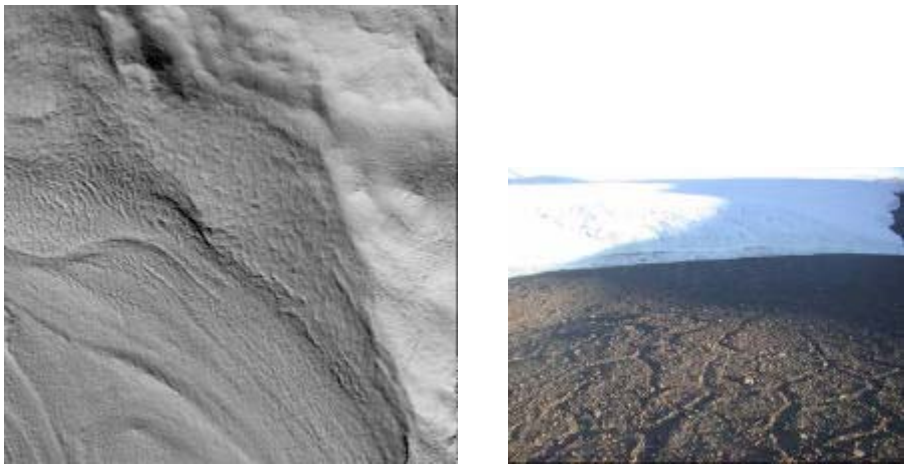

Fig. 36. Rock polygons and rock glacier surface on shaded relief DEM (left panel) and photograph (right panel), Beacon Valley.
The shaded relief measures about 1 km across. Photograph from courtesy of C. Hallam, USGS.

Other targets of the precise laser survey were surficial faults, including neotectonic faults. Fig. 37 illustrates how the linear fault traces, etched by erosion, can be mapped across bedrock terrain and Fig. 38 shows a striking rendering of a Quaternary fault.

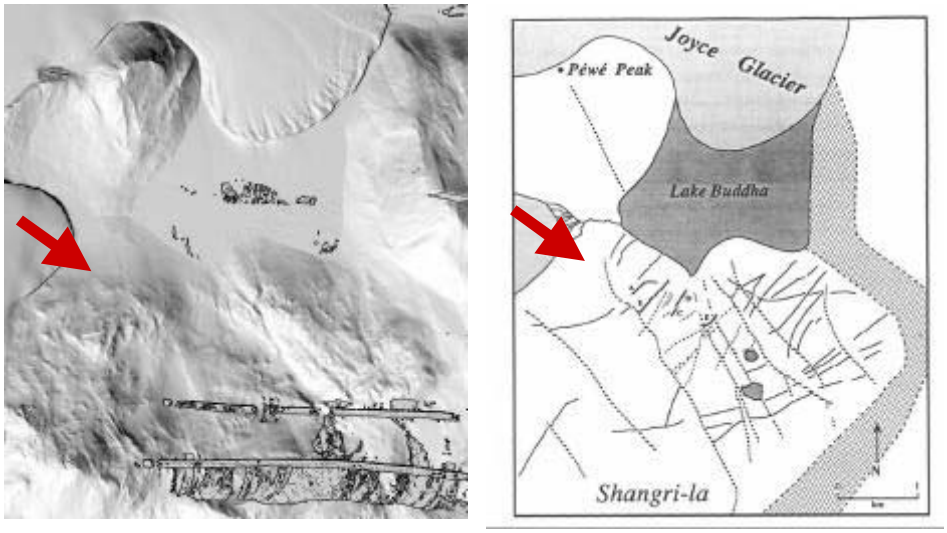

Fig. 37. Mapping cross-cutting fault array on Prekambrian rocks, Joyce glacier, Denton Hills.

Left panel: shaded relief DEM; right panel: detailed map of surface faults from field observations (Right panel is from Terry Wilson, in preparation)

Erro

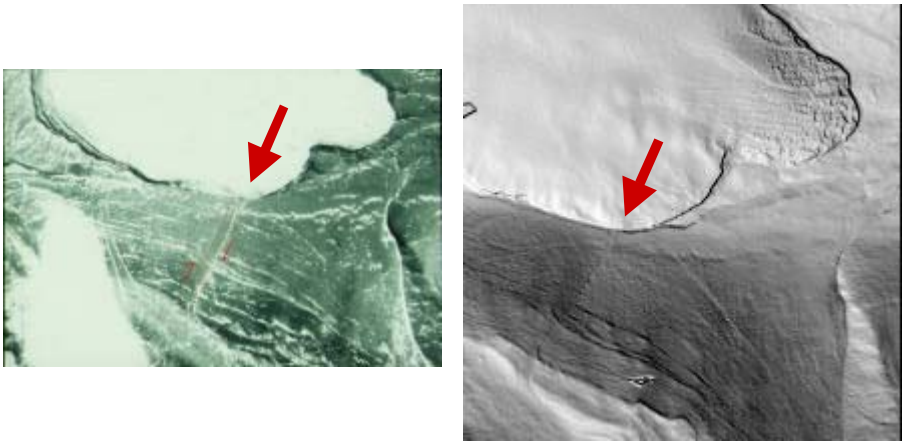

Fig. 38. Mapping Quaternary faults, Garwood Valley, Denton Hills.
Left panel: Quaternary fault on aerial photograph (Jones, 1996); right panel: same fault on shaded relief DEM.

In volcanic regions, the morphological shapes of volcanic cones can be used for structural mapping (Wilson and others, in press). Detailed information on the ellipticity, the symmetry of maximum/minimum elevation points, and the position of breaches on cone rims yield information on the geometry of underlying magmatic fissures and/or of faults that controlled ascent and emplacement of volcanic materials (Fig. 39).

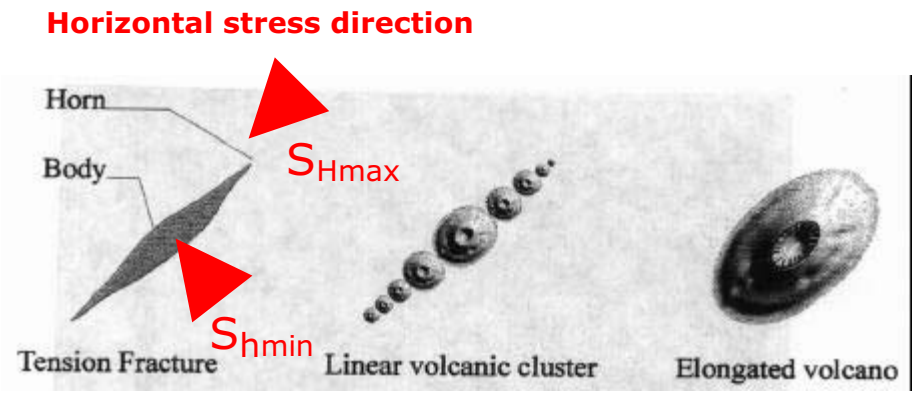

Fig. 39. Surface signatures of volcanic fissures – cone morphology as indicator of fault control (from Terry Wilson, in preparation).

Only locations and general cone shape are possible to map from imagery (aerial photos, Landsat, SPOT), for example on the color composite shown in the upper right panel of Fig. 40. The detailed topographic information from the LIDAR data makes it possible to quantify morphologic parameters of volcanic cones around Mt Discovery and Mt Morning and thus to obtain information on the structural kinematics and dynamics of the southern McMurdo Sound region in the late Cenozoic (Fig. 40, lower panel).

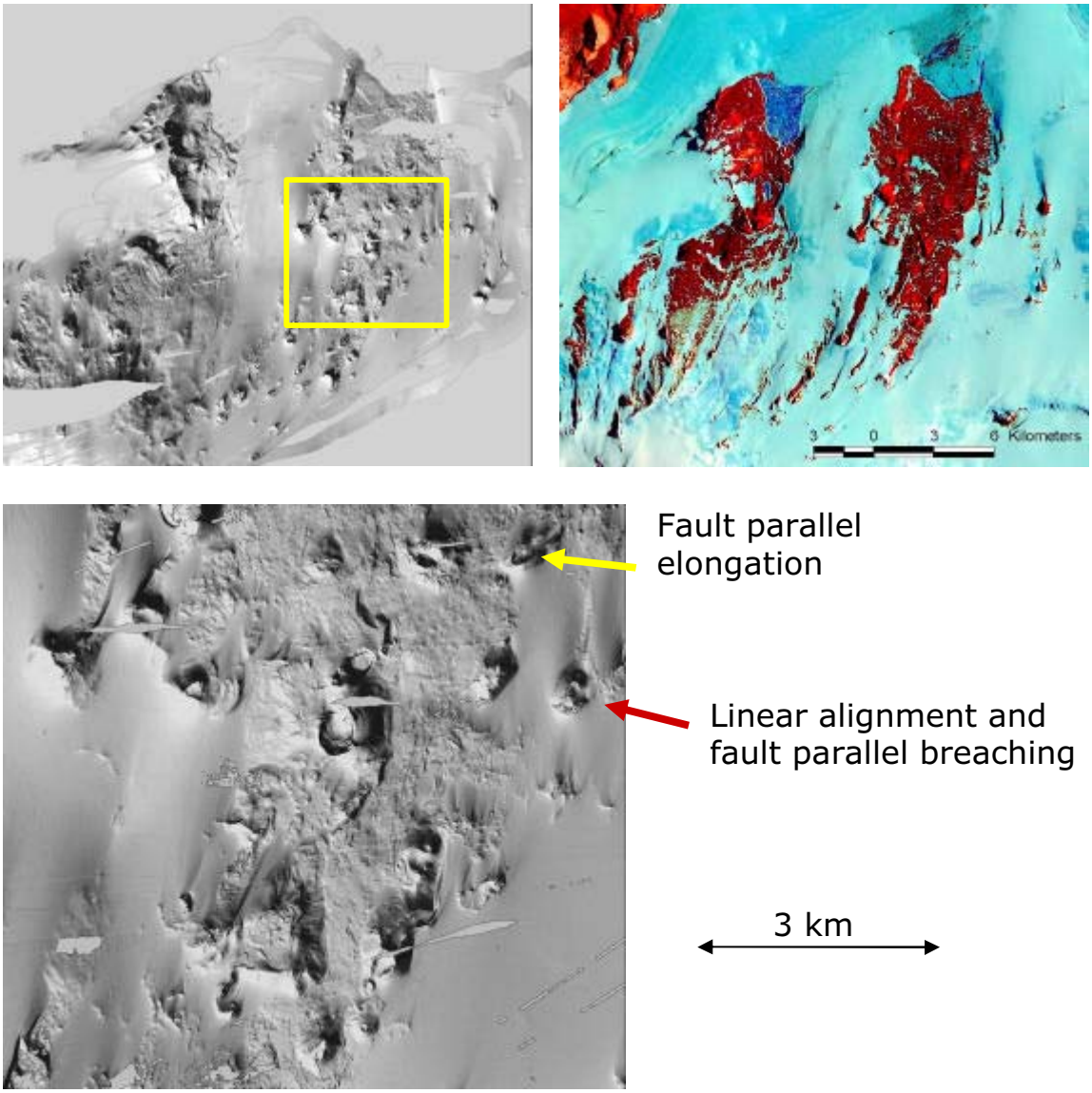

Fig. 40. Volcanic cone mapping with airborne laser altimetry.
Upper left panel: shaded relief DEM of northern slope of Mt. Morning; upper right panel: false color Landsat composite image, lower panel: enlarged part of 2 m resolution DEM showing fault parallel elongated volcanic cones, linear alignemt and fault parallel breaching.

5.1. Summary

This chapter presents results from the investigation of the regional structure of the Transantarctic Mountains in the Southern Victoria Land and Cenozoic volcanics around the McMurdo Sound. The OSU effort was focused on developing an integrated database of satellite imagery, geological and geophysical data sets to create a tool for modeling and interpretation of the magnetic data and for long-term study of the evolution of the TAM (Wilson and others, 1999 and 2001; Felus and Csathó, 2000; Csathó and others, 2001a and 2001b). My duties included the interpretation of remote sensing and geophysical data, potential field modeling and the

investigation and application of different fusion methods to support the interpretation. Potential field data processing and profile interpretation were done in collaboration with János Kiss from the Eötvös Loránd Geophysical Institute of Hungary. T. Wilson is leading the structural geological interpretation.

High resolution, airborne laser scanning data were acquired with NASA's ATM system in Southern Victoria Land in 2001-2002 during a campaign jointly supported by NASA and NSF. To process the data, my group developed new methods to remove the outlier observations, to reduce the random observational noise and to interpolate DEMs (Csathó and others, in press; Lee and others, in press). The 2-4 meter resolution DEMs depict the microtopography with striking details, providing accurate elevation data for various applications, including terrain analysis, geological mapping and geomorphological modeling (Wilson and others, in press, Csathó and others, 2003).

My results related to the geological and glaciological mapping in Southern Victoria Land and to the novel application of laser altimetry for mapping surface microstructure are summarized in Section V of the thesis booklet.

CONCLUDING REMARKS

The investigation of the polar regions will be an important goal in the years to come. To understand the geodymanical ad glaciological measurements or the interactions in the Earth-atmosphere-ocean-ice sheet system, we need to combine results from several disciplines. My intention was to contribute to this integrated approach, by developing new processing tools, exploring new applications of airborne and spaceborne remote sensing methods and by combining the tools and knowledge from glaciology and geophysics to investigate the effect of geologic control on ice flow.

The planned International Geophysical Year in 2007-8, the successor of the IPY in 1957-58 will be a major milestone of the polar research. Our research group proposes a comprehensive study of the Greenland ice sheet (Braun and others, in press). Greenland is a unique geophysical target since it represents a coupled system of the solid Earth and the cryosphere on different spatial scales. Major open questions include the structure, the history and the thermo-mechanical properties of the bedrock, the crust, the lithosphere and the mantle as well as their interaction with the ice sheet. Modeling ice dynamics requires a detailed knowledge of the bedrock properties and the lithology to infer basal melting and ice flow. In studies of ice mass balance or the contribution to sea level change, geodynamic processes such as glacial isostatic adjustment and crustal deformation have to be taken into account. Examples of coupled processes are ice surface deformations, englacial and basal melting, which are related to the onset of fast flow and possibly to the migration of shear margins. The basal melt indicates higher than average crustal heat flow, which in turn can be associated with temperature variations in the crust/mantle and thus may be triggered by past and ongoing geodynamic processes. Geophysical observations in Greenland have a long history ranging from Alfred Wegener's first meteorological records in 1906 to the completion of the Arctic Gravity Project in 2003. Although the scientific database of Greenland is continuously growing, there are only minor efforts in the solid Earth community to exploit and evaluate the recently collected data and merge these with historic data. Further, the interaction between the geophysical and the glaciological community has not been fully developed. While atmospheric sciences and off-shore geology of Greenland are well established, the large picture of Greenland's geological structure and history is still blurry. Past geodynamic activity, e.g. from a hotspot or rifting events, might have significant influence on present ice dynamics. Processes like glacial isostatic adjustment and glacier dynamics are shaping Greenland's surface. These processes must be observed with geophysical, geodetic and glaciological methods as a pre-requisite for further investigations. We like to initiate a concerted action (1) to collect further data (e.g. by airborne geophysical campaigns, seismic profiling,

borehole logging), (2) to establish an integrated and interdisciplinary interpretation, and (3) to promote international cooperation (e.g. with Denmark and Germany). In addition, an initiative focusing on the analysis of existing data would be a desirable step. The International Polar Year provides an exceptional opportunity to combine expertise in the relevant fields, and to study the interaction of geophysics, geology and glaciology. Greenland as a science target has received less attention compared to Antarctica, which might have political and economic reasons. We propose to initiate a discussion to establish a program focusing on the solid Earth - cryosphere interaction and put Greenland on the agenda in the US polar research community for the International Polar Year.

ACKNOWLEDGEMENT

My research would not have been possible without extensive collaboration and I would like to thank all my collaborators for their interest and enthusiasm. The papers I co-authored with them are listed in the reference list and in the thesis booklet. This research was partially sponsored by NASA's PARCA and ICESat programs and NSF grants.

REFERENCES

Abdalati, W., W. Krabill, E. Frederick, S. Manizade, C. Martin, J. Sonntag, R. Swift, R. , W. Wright, and J. Yungel (2001), Outlet glacier and margin elevation changes: Near-coastal thinning of the Greenland ice sheet. *J. Geophys. Res.106*, 33,729-33,741.

Abdalati, W., S. Manizade, Golder, B. Csathó, R. Thomas, W. Krabill (in press), Increase in flow rates of the Jakobshavns Isbræ, Greenland. *Eos. Trans. AGU*, Fall Meet. Suppl..

Abshire, J.B., J.F. McGarry, L. K. Pacini, J.B. Blair, and G.C. Elman (1994), Laser Altimetry Simulator, Version 3.0 User's Guide. *NASA Technical Memorandum 104588*, NASA/GSFC, Greenbelt, MD, 70 pages.

Adalgeirsdóttir, G., K. Echelmeyer, W. Harrison (1998), Elevation and volume changes of Harding Icefield, Alaska. *J. Glaciology 44,* 148, 570-581.

Ager, C.M., and N.M. Milton (1987), Spectral reflectance of lichens and their effects on the reflectance of rock substrates. *Geophysics 52*, 898-906.

Aldred, A., and G. Bonner (1985), Application of Airborne Lasers to Forest Surveys. *Canadian Forestry Service, Petawawa National Forestry Centre, Information Report PI-X-51*, 62 pages.

Alley, R.B. and R.A. Bindschadler (eds.) (2001), *The West Antarctic Ice Sheet: Behavior and Environment.* Washington DC: American Geophysical Union, Antarctic Research Series vol. 77, 296 pages.

Anandakrishnan, S., and C. Bentley (1993), Micro-earthquakes beneath Ice Streams B and C, West Antarctica: observations and implications. *J. Glaciology 39*, 133, 455-462.

Anandakrishnan, S., D.D. Blankenship, R.B. Alley, and P.L. Stoffa (1998), Influence of subglacial geology on the position of a West Antarctic ice stream from seismic observations. *Nature 394*, 62-65.

Bales, R.C., J.R. McConnell, E. Mosley-Thompson and B. Csathó (2001), Historical and recent accumulation over the Greenland ice sheet. *J. Geophys. Res.106,* D24, 33,813-33,826 (2001JD900153).

Bamber, J.L., and J.P. Muller (1998), Derivation of a global land elevation data set from satellite radar altimeter data for topographic mapping. *J. Geophys. Res.-Atmos., 103*, D24, 32159-32168.

Bamber, J.L., R.J. Hardy, and I. Joughin (2000), An analysis of balance velocities over the Greenland ice sheet and comparison with synthetic aperture radar interferometry. *J. Glaciology 46,* 152, 67-74.

Bamber, J.L., R.L. Layberry, and S.P. Gogineni (2001a), A new ice thickness and bed data set for the Greenland ice sheet. 1. Measurement, data reduction, and errors. *J. Geophys. Res. 106*, 33,773-33,780.

Bamber, J. L., S. Ekholm, and W. B. Krabill (2001b), A new, high-resolution digital elevation model of Greenland fully validated with airborne laser data. *J. Geophys. Res. 106*, 6733-6745.

Bell, R.E., D.D. Blankenship, C.A. Finn, D.L. Morse, T.A. Scambos, J.M. Brozena, and S.M. Hodge (1998), Influence of subglacial geology on the onset of a West Antarctic ice stream from aerogeophysical observations. *Nature 394*, 58-62.

Beschel, R. E. (1961), Dating rock surfaces by lichen growth and its application to glaciology and physiography (lichenometry). In Raasch, G. O. (ed.), *Geology of the Arctic 2*, Univ. Toronto Press, 1044-1062.

Bindschadler, R., and P. Vornberger (1998), Changes in the West Antarctic Ice Sheet since 1963 from declassified satellite photography. *Science 279*, 689-692.

Bindschadler, R., J. Bamber, and S. Anandakrishnan (2001), Onset of streaming flow in the Siple Coast region, West Antarctica. In: *The West Antarctic Ice Sheet: behavior and environment (eds. R.B. Alley and R.A. Bindschadler).* American Geophysical Union, Washington DC, Antarctic Research Series vol. 77, 123-136.

Blair, J.B., D.B. Coyle, J.L. Bufton, and D.J. Harding (1994). Optimization of an airborne laser altimeter for remote sensing of vegetation and tree canopies. *Proc. IGARSS'94*, 939-941.

Blankenship, D.D., D.L. Morse, C.A. Finn, R.E. Bell, M.E. Peters, S.D. Kempf, S.M. Hodge, M. Studinger, J.C. Behrendt, and J.M. Brozena (2001), Geologic controls on the initiation of rapid basal motion for West Antarctic ice streams: a geophysical perspective including new airborne radar sounding and laser altimetry results. In: *The West Antarctic Ice Sheet: behavior and environment (eds. R.B. Alley and R.A. Bindschadler).* American Geophysical Union, Washington DC, Antarctic Research Series vol. 77, 105-121.

Bøgvad, R. (1940), Quaternary geological observations etc. in south-east and south Greenland. *Meddelelser om Grønland 107(3)*, 42 pages.

Braun, A., B. Csathó, C. J. van der Veen, T. Wilson, R. von Frese, J. Daniels, M. Bevis, C. K. Shum (in press), Greenland: A geophysical target for the International Polar Year. *Eos. Trans. AGU*, Fall Meet. Suppl..

Brenner, A.C., H.V. Frey, and H.J. Zwally (1990), Comparisons between GEOSAT and SEASAT tracking over nonocean surfaces. *Geophys. Res. Lett. 17,* 10, 1537-1540.

Brenner, A.C., H.J. Zwally, C.R. Bentley, B.M. Csathó, D. J. Harding, M.A. Hofton, J.-B. Minster, J.L. Saba, R.H. Thomas, and D. Yi (1999), Derivation of range and range distribution from laser pulse waveform analysis for surface elevations, roughness, slope and vegetation heights. *Geoscience Laser Altimeter System (GLAS), Algorithm Theoretical Basis Document*, version 2.0, NASA, Goddard Space and Flight Center, 87 pages.

Broecker, W.S. (1994), Massive iceberg discharges as triggers for global climate change. *Nature 372*, 421-424.

Bromwich, D. H., R. I. Cullather, Q-s. Chen, and B. Csathó (1998), Evaluation of recent precipitation studies for the Greenland Ice Sheet. *J Geophys. Res. 103*, D20, 26,007-26024.

Brooks, R.L., W.J. Campbell, R.O. Ramseier, H.R. Stanley and H.J. Zwally (1978), Ice sheet topography by satellite altimetry. *Nature 274*, 539-543.

Brozena, J.M. (1995), *Kinematic GPS and Aerogeophysical Measurement: Gravity, Topography and Magnetics*. Ph.D. thesis, St. Edmund's College, University of Cambridge, 185 pages.

Budd, W.F. (1970), Ice flow over bedrock perturbations. *J. Glaciology 9*, 55, 29-48.

Budd, W.F., and D.B. Carter (1971), An analysis of the relation between the surface and bedrock profiles of ice caps. *J. Glaciology 10*, 59, 197-209.

Bufton, J.L., J.E. Robinson, M.D. Femiano, and F.S. Flatow (1982), Satellite laser altimeter for measurement of ice sheet topography. *IEEE Transactions on Geoscience and Remote Sensing GE-20*, 4, 544-549.

Bufton, J.L. (1989), Laser altimetry measurements from aircraft and spacecraft. *Proceedings of the IEEE, 77*, **3**, 463-477.

Bufton, J.L., J.B. Garvin, J.F. Cavanaugh, L. Ramosizquierdo, T.D. Clem, and W.B. Krabill (1991), Airborne lidar for profiling of surface topography. *Opt. Eng. 30*, 1, 72-78.

Carsey, F.D., ed. (1992), *Microwave remote sensing of sea ice*. American Geophysical Union, 462 pages.

Chuah, .S. (1996), *Design and development of a coherent radar depth sounder for measurement of Greenland ice sheet thickness*. D.E. thesis, University of Kansas.

Chuah, T.S., S.P. Gogineni, C. Allen, and B. Wohletz (1996), *Radar thickness measurements over the northern Greenland ice sheet.* Lawrence, KS, University of Kansas Radar Systems and Remote Laboratory, Technical Report 10470-3.

Clark, C.D. (1993), Mega-scale glacial lineations and cross-cutting ice-flow landforms. *Earth Surface Processes and Landforms 18*, 1-29.

Clark, C.D. (1997), Reconstructing the evolutionary dynamics of former ice sheets using multi-temporal evidence, remote sensing and GIS. *Quaternary Science Reviews 16*, 1067-1092.

Clark, C.D., J.K. Knight, and J.T. Gray (2000), Geomorphological reconstruction of the Labrador Sector of the Laurentide ice sheet. *Quaternary Science Reviews 19*, 1343-1366.

Clarke, T.S., C. Liu, N.E. Lord, and C.R. Bentley (2000), Evidence for a recently abandoned shear margin adjacent to ice stream B2, Antarctica, from ice-penetrating radar measurements. *J. Geophys. Res. 105*, 13,409-13,422.

Comiso, J.C. (1995), Satellite remote sensing of the Arctic Ocean and adjacent seas. *Arctic Oceanography: Marginal ice zones and continental shelves, Coastal and estuarines studies 49*, 1-50.

Csathó, B.M. and R.H. Thomas (1995), Determination of sea ice surface roughness from laser altimetry waveform. *BPRC Technical Report No. 95-03*, Byrd Polar Research Center, The Ohio State University, Columbus, Ohio, 45 pages.

Csathó B. M., R. H. Thomas, W. B. Krabill (1995a), Mapping ice sheet topography with laser altimetry in Greenland. *Eos. Trans. AGU*, Fall Meet. Suppl., pp. 194.

Csathó, B. M., A. F. Schenk, R. H. Thomas, W. B. Krabill (1995b), Topographic mapping by laser altimetry. *Proceedings of SPIE*, 2572, 10-20.

Csathó, B., T. Schenk, R. Thomas, R., and W. Krabill (1996a), Remote sensing of polar regions using laser altimetry. *International Archives of Photogrammetry and Remote Sensing 33*, B1, 42-47.

Csathó, B. M., and R. H. Thomas (1996), Determination of sea ice surface roughness from laser altimetry waveform. *Proceedings of Progress in Electromagnetics Research Symposium*, pp. 147.

Csathó, B. M., R. H. Thomas, W. B. Krabill (1996b), Mapping ice sheet topography with laser altimetry in Greenland. *BPRC Technical Report No. 96-01*, 53 pages.

Csathó, B. M., R. H. Thomas, W. B. Krabill (1996c), Mapping ice sheet topography with laser altimetry in Greenland. In *Glaciers, Ice Sheets and Volcanoes, A Tribute to Mark F. Meier,* ed. Samuel C. Colbeck, U. S. Army Corps of Engineers, Cold Region Research and Engineering Laboratory, 19-26.

Csathó, B.M., H. Xu, R. Thomas, D. Bromwich, and Q-C. Chen (1997), Comparison of accumulation and precipitation maps of the Greenland ice sheet. *Eos. Trans. AGU 78*, 46, Fall Meet. Suppl., F9.

Csathó, B., and T. Schenk (1998), Multisensor data fusion for automatic scene interpretation. *International Archives of Photogrammetry and Remote Sensing 32*, 3/1, 60-65.

Csathó, B., C. Kim, and J. Bolzan (1999a), Development of Greenland GIS database system. In *PARCA Report 1998* (W. Abdalati, ed.), NASA/TM-1999-209205, Greenbelt, MD, 80-84.

Csathó, B., G. Ahn, and T. Wilson (1999b), Structural mapping of the Transantarctic Rift Flank, Southern Victoria Land, from remote sensing data. *8th International Symposium on Antarctic Earth Sciences*, Wellington, New Zealand, abstracts volume.

Csathó, B. M., T. Schenk, D.-C. Lee and S. Filin (1999c), Inclusion of multispectral data into object recognition. *International Archives of Photogrammetry and Remote Sensing 32,* 7-4-3 W6, 53-61.

Csathó, B. M., J. F. Bolzan, C. van der Veen, T. F. Schenk, and D-C. Lee (1999d), Surface velocities of a Greenland outlet glacier from high-resolution visible satellite imagery. *Polar Geography 23*, 71-82.

Csathó, B., T. Wilson, J. Kiss, D. Damaske, and C. Finn (2001a), Aeromagnetic constraints on Transantarctic Mountains rift flank. *Eos. Trans. AGU 82*, 20, Spring Meet. Suppl., Abstract GP42A-08.

Csathó, B., Wilson, T., and C. J. van der Veen (2001b), Investigation of geologic control on ice sheets using remote sensing imagery. *4th International Symposium on Remote Sensing in Glaciology, IGS*, June 4-8, 2001, College Park, MD, USA, Abstract volume, pp. 23.

Csathó, B., Y-R. Lee, T. Schenk, W. Krabill, and J. McGarry (2001c). Creation of high resolution Digital Elevation Models (DEM) of Ocean City abd Assateague Island, MD. *International Archives of Photogrammetry and Remote Sensing 34*, 3 W4, 31-35.

Csathó, B., T. Schenk, S. Shin, and C. J. van der Veen (2002a), Investigating long-term behavior of Greenland outlet glaciers using high resolution imagery. *Proc. IGARSS'02*, published on CD-ROM.

Csathó, B., T. Schenk, S.W. Shin and C.J. van der Veen (2002b)..Investigating long term behavior of Greenland outlet glaciers using high resolution satellite and aerial imagery. *International Symposium of fast glacier flow, IGS,* June 10-14, 2002, Yakutat, Alaska, USA, abstract volume.

Csathó, B., T. Wilson, T. Schenk, G. McKenzie, W. Krabill and C. Hallam (2003), Geomorphologic mapping by airborne laser scanning in Southern Victoria Land, Antarctica. *9th International Symposium on Antarctic Earth Sciences*, September 8-12, 2003, Potsdam, Germany, page 59.

Csathó, B., and C. J. van der Veen (in press), Mapping periglacial trimlines from multispectral satellite imagery. *PARCA Report.*

Csathó, B., T. Schenk, K-I. Huh, I. V. B. Spikes, and W. Krabill (in press), ICESat calibration-validation and mass balance studies in Antarctica. *Eos. Trans. AGU*, Fall Meet. Suppl..

Dahl-Jensen, T., T.B. Larsen, I. Woelbern, T. Bach, W. Hanka, R. Kind, S. Gregersen, K. Mosegaard, P. Voss, and O. Gudmundsson (2003), Depth to Moho in Greenland: receiver function analysis suggests two Proterozoic blocks in Greenland. *Earth and Planetary Science Letters 205,* 379-393.

Davis, C.H., C.A Kluever, and B.J. Haines (1998), Elevation Change of the Southern Greenland Ice Sheet. *Science 279*, 2086-2088.

Davis, C.H., C. A. Kluever, B.J. Haines, C. Perez, and Y. Yoon (2000), Improved elevation change measurement of the southern Greenland ice sheet from satellite radar altimetry. *IEEE Transactions on Geoscience & Remote Sensing 38*, 1367-1378.

Doumani, G.A. (1967), Surface structures in snow. In *Physics of Snow and Ice: Sapporo Conference, 1966* (H. Oura, ed.), Inst. of Low Temp. Science, U. Hokkaido, 1119-1136.

Drewry, D.J., N.F. McIntyre, and P. Cooper (1985), The Antarctic ice sheet: a surface model for satellite altimeter studies.In *Models in Geomorphology* (Woldenberg, H. J., ed.), Allen and Unwin, Boston, 1-23.

Echelmeyer, K., W. Harrison, C. Larsen, J. Sapiano, J. Mitchell, J. DeMallie, B. Rabus, G. Adalgeirsdottir, L. Sombardier (1996), Airborne surface profiling of glaciers: A case study in Alaska. *J. Glaciology 42,* 142, 538-547.

Ekholm, S., K. Keller, J.L. Bamber, and S.P. Gogineni (1998), Unusual surface morphology from digital elevation models of the Greenland Ice Sheet. *Geophys. Res.Lett.. 25*, 3623-3626.

Endo, Y., and K. Fujiwara (1973), Characteristics of the snow cover in East Antarctica along the route of the JARE South Pole traverse and factors controlling such characteristics. *Japanese Antarctic Research Expedition Scientific Reports C*, 4-11.

Engelhardt, H., N. Humphrey, B. Kamb, M. Fahnestock (1990), Physical conditions at the base of a fast moving Antarctic ice stream. *Science 248*, 57-59.

Escher,J.C., and T.C.P. Pulvertaft (1995), Geological Map of Greenland, scale 1:2,500,000. Copenhagen, Geological Survey of Greenland, Denmark.

Escher, J.C., and W.S. Watt (eds.) (1976), *Geology of Greenland*, Geological Survey of Greenland, Denmark.

Fahnestock, M., R. Bindschadler, R. Kwok, and K, Jezek (1993), Greenland Ice Sheet surface properties and ice dynamics from ERS-1 SAR imagery. *Science 262*, 1530-1534.

Fahnestock, M., W. Abdalati, I. Joughin, J. Brozena, and P. Gogineni (2001), High geothermal heat flow, basal melt and the origin of rapid ice flow in central Greenland. *Science 294,* 2338-2342.

Felus, Y. A, and B. Csathó (2000), Multi-source DEM evaluation at the Antarctica, Transantarctic Mountains project. *International Archives of Photogrammetry and Remote Sensing 32***,** B1, 117-123.

Fifield, R. (1987), *International Research in the Antarctic*. Oxford University Press, New York, 146 pages.

Filin, S., and B.M. Csathó (1999). A novel approach for calibrating satellite laser altimeter systems. *International Archives of Photogrammetry and Remote Sensing 32***,** 3-W14, 47-54.

Filin, S., B. Csathó (2000a), *An algorithm and application for visualization and analysis of scanning laser altimeter data.* BPRC Technical Report 2000-01, 29 pages.

Filin, S., B. Csathó (2000b), *An efficient algorithm for the synthesis of laser altimeter waveform*. BPRC Technical Report 2000-02, 27 pages.

Filin S., B. Csathó, and T. Schenk (2001). An analytical model for in-flight calibration of laser altimeter systems using natural surfaces. In *Proceedings of ASPRS 2001*, April 24-27, 2001, St. Louis, Missouri, published on CD-ROM.

Filin, S., and B. Csathó (2002), Improvement of elevation accuracy for mass balance monitoring using in-flight laser calibration. *Annals of Glaciology 34*, 330-334.

Flint, R.F. (1971), *Glacial and Quaternary Geology*. New York NY: John Wiley & Sons, 892 pages.

Frey, H. and A.C. Brenner (1990), Australian topography from SEASAT overland altimetry. *Geophys. Res. Lett. 17*, 10, 1533-1536.

Furukawa, T., O. Watanabe, K. Seko, and Y. Fujii (1992), Distribution of surface conditions of ice sheet in Enderby Land and East Queen Maud Land, East Antarctica. *Proceeding of NIPR Symposium on Polar Meteorology and Glaciology 5*, 140-144.

Gardner, C.S. (1982), Target signatures for laser altimeters: An analysis. *Applied Optics 21*, **3,** 448-453.

Gardner, C.S. (1992), Ranging performance of satellite laser altimeters. *IEEE Transactions on Geoscience and Remote Sensing 30,* 5, 1061-1072.

Garvin, J. and R. Williams (1993), Geodetic airborne laser altimetry of Bredamerkurjökull and Skeidarárjökull, Iceland, and Jakobshavns Isbrae, West Greenland. *Annals of Glaciology 17*, 379-385.

Garvin, J., J. Bufton, J. Blair, D. Harding, S. Luthcke, J. Frawley, and D. Rowlands (1998), Observations of the Earth's topography from the Shuttle Laser Altimeter(SLA): laser-pulse echo-recovery measurements of terrestrial surfaces. *Phys. Chem. Earth 23*, **9-10**, 1053-1068.

Gates, D.M., H.J. Keeger, J.C. Schleter, and V.R. Weidner (1965), Spectral properties of plants. *Applied Optics 4,* 11-20.

Gates, D.M., H.J. Keegan, and V.R. Weidner (1966), Spectral reflectance and planetary reconnaissance. *Scientific Experiments of Manned Orbital Flight and Technology Series 4,* 71-86.

Gauslaa, Y. (1984), Heat resistance and energy budget in different Scandinavian plants. *Holarctic Ecology 7*, 1-78.

GEUS, *Geological Map of Greenland 1:500,000, Søndre Strømfjord (Nûgssuaq (Sheet 3)*, Geology of Greenland Map Series CD2, Geological Survey of Denmark and Greenland, Ministry of Environment and Energy

Gogineni, S., D. Tammana, D. Braaten, C. Leuschen, T. Akins, J. Legarsky, P. Kanagaratnam, J. Stiles, C. Allen, and K. Jezek (2001), Coherent radar ice thickness measurements over the Greenland ice sheet. *J. Geophys. Res. 106*, 33,761-33,772.

Gregersen, S. (1997), Seismicity and tectonics in Greenland, *Workshop on Greenland observatory, May 20-22, 1997,* abstract from web (www.hw.arizona.edu/ ~Alpine/Summit/abstr7b.html).

Grenfell, T.C., and D.K. Perovich (1984), Spectral albedos of sea ice and incident solar irradiance in the southern Beaufort Sea. *J. Geophys. Res. 89,* **C3**, 3,573-3,580.

Gribbon, P.W.F. (1964), Recession of glacier Tasîssârssik A, East Greenland. *J. Glaciology 39*, 361-365.

Hale, M.E. (1983), *Biology of lichens.* Edward Arnold, 495 pp.

Hall, D. K. and J. Martinec (1985), *Remote sensing of ice and snow*. Chapman and Hall Ltd, New York, NY, 189 pages.

Hamilton, G., I. Whillans, P. J. Morgan (1998), First point measurements of ice sheet thickness change in Antarctica. *Annals of Glaciology 27*, 125-129.

Harding, D.J., J.B. Blair, J.B. Garvin, and W.T. Lawrence (1994), Laser altimetry waveform measurement of vegetation canopy structure. *Proc. IGARSS'94*, 1251-1253.

Harding, D.J., J.L. Bufton, and J.J. Frawley (1994a), Satellite laser altimetry of terrestrial topography: vertical accuracy as a function of surface slope, roughness, and cloud cover. *IEEE Transactions on Geoscience and Remote Sensing 32,* **2**, 329-339.

Harding, D.J. (1998), Airborne lidar observations of canopy structure at the BOREAS tower flux sites. *Proc. IGARSS '98*, 1550-1552.

Hawksworth, D.L., and D.J. Hill (1984), *The lichen-forming fungi.* London: Blackie, 158 pp

Haworth, L.A., P.E. Calkin and J. M. Ellis (1986), Direct measurements of lichen growth in the central Brooks Range, Alaska, USA, and its application to lichenometric dating. *Arctic and Alpine Research 18*, 289-296.

Hoffman, G.R. (1970), Spectral properties of selected species and some variation accompanying leaf thickness, pigmentation, and dehydration. *Proceedings S.D. Academy of Sciences 49,* 60-72.

Hofton, M.A., J.B. Blair, J.B. Minster, J.R. Ridgway, N.P. Williams, J.L. Bufton, D.L. Rabine (2000), An airborne scanning laser altimetry survey of Long Valley, California. *Int. J. Rem. Sens. 21*, 12, 2413-2437.

Houghton, J. T. and others (eds.) (2001), *Climate Change 2001: The Scientific Basis*. Contribution of Working Group I to the Third Assessment Report of the Intergovernmental Panel on Climate Change (IPCC), Cambridge, University Press, 881 pages.

Hughes, T.J. (1998), *Ice Sheets.* New York NY: Oxford University Press, 343 pages.

Hutter, K., F. Legerer, and U. Spring (1981), First-order stresses and deformations in glaciers and ice sheets*. J. Glaciology 27*, **96**, 227-270.

Huybrechts, P. (1994), The present evolution of the Greenland ice sheet: an assessment by modeling. *Global and Planetary Change* 9, 39-51.

Huybrechts, P. (1996), Basal temperature conditions of the Greenland ice sheet during the glacial cycles. *Annals of Glaciology* 23, 226-236.

Jezek, K.C. (1999), Glaciological properties of the Antarctic ice sheet from RADARSAT-1 synthetic aperture radar imagery. *Annals of Glaciology 29*, 286-290.

Joughin, I., L. Gray, R. Bindschadler, S. Price, D. Morse, C. Hulbe, M. Karim, and C. Werner (1999a), Tributaries of West Antarctic ice streams by RADARSAT interferometry. *Science 286*, 283-286.

Joughin, I., M. Fahnestock, R. Kwok, P. Gogineni, and C. Allen (1999b), Ice flow of Humboldt, Petermann and Ryder Gletscher, northerm Greenland. *J. Glaciology 45*, 231-241.

Joughin, I., M. Fahnestock, D. MacAyeal, J.L. Bamber, and P. Gogineni (2001), Observation and analysis of ice flow in the largest Greenland ice stream. *J. Geophys. Res. 106,* 34,021-34,034.

Karrow, P.F., A. Dreimanis, and P.J. Barnett (2000), A proposed diachronic revision of late Quaternary time-stratigraphic classification in the eastern and northern Great Lakes area. *Quaternary Research 54*, 1-12.

Kessler, M.A. and B. T. Werner (2003), Self-organization of sorted patterned ground. *Science 299*, 380-383.

Kim, C., B. Csathó, R. Thomas, C. J. van der Veen (2000), Studying and monitoring the Greenland ice sheet using GIS techniques. *International Archives of Photogrammetry and Remote Sensing 32,* B7/2, 678-685.

Kirkbridge, M.P. and A.J. Dugmore (2001), Can lichenometry be used to date the "Little Ice Age" glacial maximum in Iceland? *Climatic Change 48*, 151-167.

Knight, P., R. Weaver, and D.E. Sugden (1987), Using Landsat MSS data for measuring ice sheet retreat. *Int. J. Remote Sensing 8*, 1069-1074.

Koblinsky, C.J., R.T. Clarke, A.C. Brenner, and H. Frey (1993), Measurement of river level variations with satellite altimetry. *Water Resour. Res. 29*, **6**, 1839-1848.

Kotlyakov, V.M. (1966), The snow cover of the Antarctic and its role in the present-day glaciation of the continent. *Israel Program for Scientific Translation*, Jerusalem, 256 pages.

Krabill, W., R. Thomas, C. Martin, R. Swift, and E. Frederick (1995), Accuracy of airborne laser altimetry over the Greenland ice sheet. *Int. J. Remote Sensing 16*, 1211-1222.

Krabill, W., E. Frederick, S. Manizade, C. Martin, J. Sonntag, R. Swift, R. Thomas, W. Wright, and J. Yungel (1999), Rapid thinning of parts of the southern Greenland ice sheet. *Science 283*, 1522-1524.

Krabill, W., W. Abdalati, E. Frederick, S. Manizade, C. Martin, J. Sonntag, R. Swift, R. Thomas, W. Wright, and J. Yungel (2000), Greenland ice sheet: high-elevation balance and peripheral thinning. *Science 289*, 428-429.

Lawrey, J.D. (1984), *Biology of lichenized fungi.* Westport CT: Praeger Publishers.

Layberry, R.L. and J.L. Bamber (2001), A new ice thickness and bed data set for the Greenland ice sheet. 2. Relationship between dynamics and basal topography. *J. Geophys. Res. 106*, 33,781-33,788.

Lee, I., Y. Ahn, B. Csathó, S. Schenk, S-W. Shin, T. Yoon (in press). Generation of large-scale and high-resolution DEMs over Antarctica through LIDAR survey. *Asian Conference Remote Sensing 2003*, Nov. 3-7, 2003 in Busan, Korea. abstract volume.

Lefsky, M.J. (1997), Application of Lidar Remote Sensing to the Estimation of Forest Canopy Structure. *Univ. of Virginia, Ph.D. Dissertation*, 185 pages.

Lefsky, A., W.B. Cohen, S.A. Acker, T.A. Spies, G.G. Parker, and D.J. Harding (1998), Lidar remote sensing of forest canopy structure and related biophysical parameters at the H.J. Andrews experimental forest, Oregon, USA. *Proc. IGARSS'98*, 1252-1254.

Lefsky, M.A, D.J. Harding, W.B. Cohen, G.G. Parker, and H.H. Shugart (1999), Surface lidar remote sensing of basal area and biomass in deciduous forests of Eastern Maryland, USA. *Rem. Sens. Environ. 67*, 83-98.

Leftwich, T.E., R.R.B. von Frese, and H.R. Kim (2001), Icelandic thermal modeling by satellite geopotential field anomalies. *EOS 82,* S127.

Leftwich, T., R. von Frese, L. Potts, D. Roman, and P. Taylor (2003), Crustal structure of the Iceland region from spectrally correlated free-air and terrain gravity data. *European Geophysical Society, Geophysical Research Abstracts, vol. 5*, p. 01280.

Legarsky, J., S.P. Gogineni, C. Allen, T.S. Chuah, and Y.C. Wong (1997), *Radar thickness measurements over the northern part of the Greenland Ice Sheet: 1996 results.* Lawrence, KS, University of Kansas Radar Systems and Remote Laboratory, Technical Report 10470-6.

Lindenberger (1993), *Laser-Profilmessungen zur topographischen Geländeaufnahme*. Ph. D. Dissertation, Universität Stuttgart, Verlag der Bayerischen Akademie der Wissenschaften, 131 pages.

Lock, W. W., J.T. Andrews and P.J. Webber (1979), A manual for lichenometry. *British Geomorphological Group, Technical Bulletin 28*, 47 pages.

Marini, J., and C. Murray (1973), Correction of laser range tracking data for atmospheric refraction at elevation angles above 10^{o}. *NASA Technical Report*, X-591-73-351, NASA/Goddard Space Flight Center.

Martin, T.V., A.C. Brenner, H.J. Zwally, and R.A. Bindschadler (1983), Analysis and retracking of continental ice sheet radar altimeter waveforms. *J. Geophys. Res. 88*, 1608-1616.

McIntyre, N.F. (1986), Antarctic ice-sheet topography and surface-bedrock relationships. *Annals of Glaciology 8*, 124-128.

McGarry, J.F., J B. Abshire, X. Sun, J. Saba, A. Brenner, and D. Yi (in process), GLAS flight science data selection algorithms for the altimeter (1064nm), Version 4.03. *NASA GSFC*

Means, J.E., S.A. Acker, D.J. Harding, J.B. Blair, M.A. Lefsky, W.B. Cohen, M.E. Harmon, and W.A. McKee, (1998)Use of a large-footprint scanning airborne lidar to estimate forest stand characteristics in the western Cascades of Oregon. *Rem. Sens. Environ. 67*, 298-308.

Methakullachat, D., B. Csathó, T. Schenk, and T. Wilson (2001), Orthorectification of DISP imagery over the Transantarctic Mountains using a rigorous black adjustment. *International Symposium on Remote Sensing in Glaciology, IGS,* June 4-8, 2001, College Park, MD, USA, Abstract volume, pp. 16.

Mikkelsen, N. and T. Ingerslev, eds. (2002), *Nomination of the Ilulissat Icefjord for inclusion in the World Heritage list.* Copenhagen, Denmark: Geological Survey of Denmark and Greenland (GEUS), 136 pages.

Mullins, J. L. (1999), The geodesy and mapping program of the United States Geological Survey in Antarctica. *Photogrammetric Engineering and Remote Sensing 65*, 12, 1340-1341.

Nilsson, M. (1996), Estimation of tree heights and stand volume using an airborne lidar system. *Rem. Sens. Environ. 56*, 1-7.

Noller, J.S., and W.W. Locke (2000), Lichenometry. In: *Quaternary Geochronology (J.S. Noller, J.M. Sowers, and W.R. Lettis eds.)*. Washington DC: American Geophysical Union, AGU Reference Shelf 4, 261-272.

Ogilvy, J. A. (1991), *Theory of Wave Scattering from Random Rough Surfaces.* Adam Hilger, Bristol, England, 277 pages.

Ohmura, A. and N. Reeh (1991), New precipitation and accumulation maps for Greenland. *J. Glaciology 37*, 140-148.

Okulitch, A.V. (compiler) (1991), Geology of the Canadian Archipelago and North Greenland; Figure 2, in H.P. Trettin (ed.), *Innuitian Orogen and Arctic Platform: Canada and Greenland*, Geological Society of America, The Geology of North America, vol. E, scale 1:2,000,000.

Paterson, W.S.B. (1994), *The Physics of Glaciers*. Permagon, Tarrytown, New York, 480 pages.

Perovich, D.K. (1996), The optical properties of sea ice. *CRREL Monograph 96-1*, U.S. Army Corps of Engineers CRREL, Hanover, NH, 24 pages.

Prescott, P. (1995), *Photogrammetric examination of the calving dynamics of Jakobshavns Isbræ, Greenland.* Orono ME: University of Maine, unpublished Ph.D. Thesis.

Punkari, M. (1982), Glacial geomorphology and dynamics in the eastern parts of the Baltic Shield interpreted using Landsat imagery. *Photogrammetric Journal of Finland 9*, 77-93.

Reeh, N., S. J. Johnsen, and D. Dahl-Jensen (1985), Dating of the Dye 3 deep ice core by flow model calculations. In *Greenland ice core, geophysics, geochemistry, and the environment* (C.C. Langway, Jr., H. Oeschger, and W. Dangaard, eds.), Am. Geophys. Union Geophys. Monograph 33, 57-65.

Retzlaff, R., N. Lord, and C. Bentley (1993). Airborne-radar studies: Ice Streams A, B and C, West Antarctica. *J. Glaciology, 39,* 133, 495.

Ridgway, J., J-B. Minster, N. Williams, J. Bufton, and W. Krabill (1997). Airborne laser altimetry survey of Long Valley, California. *Geophys. J. Int., 131*, 267-280.

Rignot, E., S. Gogineni, I. Joughin, and W. Krabill (2001), Contribution to the glaciology of northern Greenland from satellite radar interferometry. *J. Geophys. Res. 106*, 34,007-34,019.

Rignot, E., G.Buscarlet, B. Csathó, S. Gogineni, W. Krabill and M. Schmeltz (2000). Mass balance of the northeast sector of the Greenland Ice Sheet: a remote sensing perspective. *J. Glaciology 46*, 265-273.

Rignot, E. and R. H. Thomas (2002), Mass balance of polar ice sheets. *Science 297*, 1502-1506.

Rivard, B., and R.E. Arvidson (1992), Utility of imaging spectrometry for lithologic mapping in Greenland. *Photogrammetric Engineering and Remote Sensing 58*, 945-949.

Robin, G. de Q. (1967), Surface topography of ice sheets. *Nature 189*, 1029-1032.

Roman, D.R. (1999), *An Integrated Geophysical Investigation of Greenlands Tectonic History*. Ph.D thesis, Dept. of Geological Sciences, The Ohio State University, 270 pages.

Satterwhite, M.B., J.P. Henley, and J.M. Carney (1985), Effects of lichens on the reflectance spectra of granitic rock surfaces. *Rem. Sens. Environ. 18*, 105-112.

Scambos, T.A., and T. Haran (2002), An image-enhanced DEM of the Greenland Ice Sheet. *Annals of Glaciology 34*, 291-298.

Schenk, T. and B. Csathó (2001), Modellierung systematischer Fehler von abtastenden Laseraltimetern. *Photogrammetrie, Fernerkundung, Geoinformation 5,* 361-373.

Schenk, T., S. Seo, and B. Csathó, (2001). Accuracy study of airborne laser scanning data with photogrammetry. *International Archives of Photogrammetry and Remote Sensing 34,* 3 W4, 113-118.

Schenk, T. and B. Csathó (2002). Fusion of lidar data and aerial imagery for a more complete surface description. *International Archives of Photogrammetry and Remote Sensing 34*, 3A, 310-317.

Schenk, T., B. Csathó, S. W. Shin (in press), Rigorous panoramic camera model from DISP imagery. *International Archives of Photogrammetry and Remote Sensing.*

Shabtaie, S. and C.R. Bentley (1988), Ice-thickness map of the West Antarctic ice streams by radar sounding. *Annals of Glaciology 11*, 126-136.

Shi, J., and M.E. Cannon (1995), Critical error effects and analysis in airborne DGPS positioning over large areas. *Manuscripta Geodaetica 69*, 261-273.

Siegal, B.S., and A.F.H. Goetz (1977), Effect of vegetation on rock and soil type discrimination. *Photogrammetric Engineering and Remote Sensing 43*, 191-196.

Sohn, H. G., K. C. Jezek, R. H. Thomas, K. Kuivinen, B. Csathó (1994), Greenland ice sheet mapping with optical leveling and global positioning system. *BPRC Technical Report No. 94-03*, Byrd Polar Research Center, The Ohio State University, Columbus, Ohio, 98 pages.

Spikes, B, B. M. Csathó, and I. Whillans (1999), Airborne laser profiling of Antarctic ice stream for change detection. *International Archives of Photogrammetry and Remote Sensing 32*, 3-W14, 169-176.

Spikes, V. B., B. M. Csathó, G. S. Hamilton and I. M. Whillans (in press), Thickness changes on Whillans Ice Stream and Ice Stream C, West Antarctica, derived from laser altimetry measurements. *J. Glaciology.*

Spikes, V. B., B. Csathó, and I. Whillans (in press), Laser profiling over Antarctic ice streams: methods and accuracy. *J. Glaciology*

Charles Stearns, P.I., Automatic Weather Station Project, University of Wisconsin-Madison, http://uwamrc.ssec.wisc.edu/aws.

Stokes, C.R. and C.D. Clark (2001), Palaeo-ice streams. *Quaternary Science Reviews 20*, 1437-1457.

Stokes, C.R., and C.D. Clark (2002), Ice stream shear margin moraines. *Earth Surface Processes and Landforms 27*, 547-558.

Studinger, M., R.E. Bell, D.D. Blankenship, C.A. Finn, R.A. Arko, D.L. Morse, and I. Joughin (2001), Subglacial sediments: a regional geological template for ice flow in West Antarctica. *Geophys.Res.Lett.. 28*, 3493-3496.

Sugden, D. E., (1974) Landscapes of glacial erosion in Greenland and their relationship to ice, topographic and bedrock conditions. In Brown, E. H., amd Waters, R. S. (editors) *Progress in geomorphology, Inst. Brit. Geogr. Spec. Pub. 7,* 177-195.

Sugden, D.E. (1978), Glacial erosion by the Laurentide ice sheet. *J. Glaciology 20*, 367-391.

Sugden, D. E. and others (1995), Preservation of Miocene glacier ice in East Antarctica. *Nature 376*, 412-414.

Thomas, R.H., W. Krabill, S. Manizade, R. Swift, and A. Brenner (1994), Comparison of radar altimetry data over Greenland with surface topography derived from airborne laser altimetry. *Proceedings Second ERS-1 Symposium*, 11-14 Oct 1993, ESA SP-361.

Thomas, R., B. Csathó, M. Fahnestock, P. Gogineni, K. Jezek, K. Kuivinen, and J. Sonntag (1997), Mass balance of Greenland ice sheet. *Eos Trans. AGU 78*, 46, Fall Meet. Suppl., F2..

Thomas, R., B. Csatho, S. Gogineni, K. Jezek, and K. Kuivinen (1998), Thickening of the western part of the Greenland ice sheet, *J. Glaciology 44*, 653-658.

Thomas, R., T. Akins, B. Csatho, M. Fahnestock, P. Gogineni, C. Kim, and J. Sonntag (2000a), Mass balance of the Greenland ice sheet at high elevations. *Science 289*, 426-428.

Thomas, R. H., W. Abdalati, T. Akins, B. Csathó, E. Frederick, P. Gogineni, W. Krabill, S. Manizade, and E. Rignot (2000b), Substantial thinning of a major east Greenland outlet glacier. *Geophys. Res. Lett. 27*, 9, 1291-1294.

Thomas, R., B. Csathó, C. Davis, C. Kim, W. Krabill, S Manizade, J. McConnell, and J. Sonntag (2001), Mass balance of higher-elevation parts of the Greenland ice sheet. *J. Geophys. Res.106*, D24, 33,707-33,716 (2001JD900033).

Thomsen, H.H., L. Thorning, and R.J. Braithwaite (1988), Glacier-hydrological conditions on the inland ice north-east of Jakobshavn/Ilulissat, west Greenland. *Grønlands Geologiske Undersøgelse Rapport 138*.

Tsai, B. M., and C.S. Gardner (1982), Remote sensing of sea state using laser altimeters. *Applied Optics 21*, **21**, 3932-3940.

Tucker, W. B., D.K. Perovich, A.J. Gow, W.F. Weeks, and M.R. Drinkwater (1992), Physical properties of sea ice relevant to remote sensing. In *Microwave Remote Sensing of Sea Ice* (F. D. Carsey, ed.), American Geophysical Union, 9-27.

Vaughn, C., J. Bufton, W. Krabill, and D. Rabine (1996), Georeferencing of airborne laser altimetry measurements. *Int. J. Remote Sensing 17*, 11, 2185-2200.

van der Veen, C.J., W.B. Krabill, B.M. Csathó, and J.F. Bolzan (1998), Surface roughness on the Greenland ice sheet from airborne laser altimetry. *Geophys.Res.Lett. 25,* 20, 3887-3890.

van der Veen, C.J., D.H. Bromwich, B.M. Csathó, and C. Kim (2001), Trend analysis of Greenland precipitation. *J. Geophys. Res. 106***,** D24, 33,909-33,918 (2001JD900156).

Van der Veen, C.J. (2001), Greenland ice sheet response to external forcing. *J. Geophys. Res. 106*, 34,047-34,058.

Van der Veen, C. J., B. Csathó and C. Tremper (submitted), Trimline mapping from multispectral Landsat imagery. *Géographie Physique at Quaternaire.*

Verhoef, J., R. Macnab, W. Roest, and Project Team (1996), *A Compilation of Magnetic Observations from the Arctic and North Atlantic Oceans and Adjacent Land Areas.* Geological Survey of Canada, Open File Reports 3281, 3282 and 3283.

von Frese, R.R.B., L.V. Potts, L. Tan, J.W. Kim, T.E. Leftwich, C.J. Merry, and J. Bossler (1998), Comparative crustal modeling of the Moon and Earth from topographic and gravity correlations. *29th Lunar Planet. Sci. Conf. Abstract #1870 (CDROM).*

von Frese, R.R.B., L. Tan, J.W. Kim, and C.R. Bentley (1999), Antarctic crustal modeling from the spectral correlation of free-air gravity anomalies with the terrain. *J. Geophys. Res.* 104, B11, 25275-25296, 1999.

Watanabe, O. (1978), Distribution of surface features of snow cover in Mizuho Plateau. *Memoirs of National Institute of Polar Research (Japan), Special Issue #7*, 44-62.

Weidick, A., (1968), Observations on some Holocene glacier fluctuations in West Greenland. *Grønlands Geologiske Undersøgelse Bulletin No. 73,* 202 pages..

Weidick, A. (1984), Studies of glacier behaviour and glacier mass balance in Greenland – a review. *Geografiska annaler 66A,* 183-195.

Weidick, A. (1992), Jakobshavn Isbrae area during the climatic optimum. *Rapp. Grønlands geol. Unders., 155,* 67-72.

Wingham, D.J., A.J. Ridout, R. Scharroo, R.J. Arthern, and C.K. Shum (1998), Antarctic Elevation Change from 1992-1996. *Science 282*, 456-458.

Whillans, I.M., and S.J. Johnsen (1983), Longitudinal variations in glacial flow: theory and test using data from the Byrd Station strain network. *J. Glaciology 29*, 101, 78-97.

Whillans, I. and Van der Veen, C. (1993), New and improved determinations of velocity of Ice Streams B and C, West Antarctica. *J. Glaciology 39*, 133, 483-490.

Wilson, T**.,** B. Csathó, D. Damaske, C. Finn, J. Behrendt, R. Bell and F. Ferraccioli (1999), Transantarctic Mountains Aerogeophysical Research Activites [TAMARA]: A progress report. *8th International Symposium on Antarctic Earth Sciences,* Wellington, New Zealand, abstract volume.

Wilson, T. J., B. Csathó, T. S. Paulsen, C. Demosthenous, and Y. Felus (2001), Space-time evolution of Antarctic volcanoes: a remote sensing approach. *GSA Annua lMeeting*, November 5-8, 2001. Boston, MA, USA, abstract volume.

Wilson, T., B. Csathó, T. Schenk, T. Paulsen and W. Krabill (in press), Airborne laser swath mapping of the Erebus Volcanic Province, Antarctica: New means to map structure of volcanic cinder cones and volcanic alignments. *Eos. Trans. AGU*, Fall Meet. Suppl..

Winchester, V. and S. Harrison (2000), Dendrochronology and lichenometry: colonization, growth rates and dating of geomorphological events on the east side of the North Patagonian Icefield, Chile. *Geomorphology 34*, 181-194.

Zuber, M.T., D.E. Smith, S.C. Solomon, D.O. Muhlemen, J.W. Head, J.B. Garvin, J.B. Abshire, J.L. Bufton (1992), The Mars Observer laser altimeter investigation. *J. Geophys. Res. 97*, E5, 7781-7797.

Zuber, M.T., D.E. Smith, S.C. Solomon, J.B. Abshire, R.S. Afzal, O. Aharonson, K. Fishbaugh, P.G. Ford, H.V. Frey, J.B, Garvin, J.W. Head, A.B. Ivanov, C.L. Johnson, D.O. Muhleman, G.A. Neumann, G.H. Pettengill, R.J. Phillips. X. Sun, H.J. Zwally, W.B. Banerdt, T.C. Duxbury (1998), Observations of the North Polar Region of Mars from the Mars Orbiter Laser Altimeter. *Science 282*, 2053-2060.

Zwally, H. J., R.A. Bindschadler, A.C. Brenner, T.V. Martin, and R.H. Thomas (1983), Surface elevation contours of Greenland and Antarctic Ice sheets. *J. Geophys. Res. 88.*

Zwally, H.J., A.C. Brenner, J.A. Major, R.A. Bindschadler, and J.G. Marsh (1989), Growth of Greenland Ice Sheet: Measurement. *Science 246*, 1587-1589.

Zwally, H.J., A.C. Brenner, J.P. DiMarzio, and T. Seiss (1994), Ice Sheet Topography from Retracked ERS-1 Altimetry. *Proceedings Second ERS-1 Symposium*, 11-14 Oct 1993, ESA SP-361.

Zwally, H.J., and 15 others (2002), ICESat's laser measurements of polar ice, atmosphere, ocean, and land. *Journal of Geodynamics 34*, 405-445.